General Disclaimer

One or more of the Following Statements may affect this Document

- This document has been reproduced from the best copy furnished by the organizational source. It is being released in the interest of making available as much information as possible.

- This document may contain data, which exceeds the sheet parameters. It was furnished in this condition by the organizational source and is the best copy available.

- This document may contain tone-on-tone or color graphs, charts and/or pictures, which have been reproduced in black and white.

- This document is paginated as submitted by the original source.

- Portions of this document are not fully legible due to the historical nature of some of the material. However, it is the best reproduction available from the original submission.

TABLE OF CONTENTS

TABLE OF CONTENTS (CONTINUED)

TABLE OF CONTENTS (CONTINUED)

LIST OF TABLES

LIST OF TABLES (continued)

LIST OF FIGURES

LIST OF FIGURES (continued)

LIST OF FIGURES (continued)

LIST OF FIGURES (continued)

1. INTRODUCTION

Silicon solar cells have been used for 22 years and have been a major space power source from the very beginning. During the last two decades there has been a great deal of improvement in the basic design and technology of solar cells and this has resulted in the latest 15% AMO cell [1] as compared to the 6% cell of 1954 [2]. Despite recent theoretical analyses, which point to a practical 19-20% AMO efficiency, there is still a technological "gap" in achieving this high efficiency [3,4]. The lack of agreement between theory and actual conversion efficiency is the basic motivating factor in the development of a complete solar cell numerical analysis program.

Silicon technology has reached a very high degree of development allowing meaningful comparisons between theory and experiments. Hence the present work emphasizes the correlation of theoretical and experimental data in addition to the development of a complete solar cell analysis. It is believed that through the detailed comparison it may be possible to reveal the problem area which could eventually lead to performance improvements and high conversion efficiency.

2. DARK CURRENT-VOLTAGE CHARACTERISTICS OF SOLAR CELLS

Since the discovery of metal-semiconductor non-ohmic behavior the rectifying effects between metal-semiconductor and semiconductor-semiconductor contacts has received a great deal of attention. In 1949 Shockley proposed the modern p-n junction theory which established the important role of minority carrier density and its exponential behavior across the junction barrier [5]. The transport equations for minority carriers are particularly simple for low injection and uniform doped semiconductor regions. The minority carrier current density can be expressed as

$$J = J_s[\exp(\frac{qV}{kT})-1], \tag{2.1}$$

$$J_s = q[\frac{n_{po}}{\tau_n} L_n + \frac{p_{no}}{\tau_p} L_p],$$

where the saturation current density J_s is a function of semiconductor parameters on both sides of the junction. Departures from Shockley's simple I-V characteristic are usually observed in silicon at room temperature and further evolutions of the p-n junction theory have modified and extended Shockley's theory [6,7,8,9].

In all silicon p-n junctions, several current transport mechanisms may exist simultaneously. The diffusion current density which is due to the injection of minority carrier over the junction barrier is of course the most important. Other mechanisms include recombination current within the depletion region [6], tunneling through the bandgap for highly doped semiconductors [9] and high injection effects for high resistivity semiconductors at large forward bias voltages [7,8]. In addition to

these fundamental limitations there are several other current mechanisms which are due to improper fabrication processes and/or material imperfections. Especially important are the series resistance and any shunting resistance. Fortunately these can be minimized by using good contact metals, grid patterns and proper sintering treatments.

In general, the departures from the simple diffusion theory always lead to poor rectification in diodes and poor curve factors and low open circuit voltages in solar cell application. Figure 2.1 shows the ideal I-V characteristics and some of the modifications at forward biased voltages. As can be seen in the figure the simple Shockley diffusion current has a diode n factor of 1 for all bias voltages. The space charge recombination current has an n factor of 2. Such an n factor may also be found at high currents caused by high injection. An abnormally large n value may be found in some devices at small voltages which is caused by small shunting resistances. An n factor of 2 may be present at high voltages and caused by a high sheet resistance. Curves (c) and (e) of Figure 2.1 show examples of these effects.

The dark I-V characteristics of a solar cell are as important as the short circuit photocurrent in determining the efficiency and power output. The components of the dark I-V characteristics described above are discussed in detail in the following sections.

2.1 Simple Diffusion Current

The current density for minority carriers in Shockley's model is

$$J = J_s[\exp(qV/kT)-1], \tag{2.2}$$

where the saturation current density J_s is a function of semiconductor parameters and the appropriate boundary conditions. First order

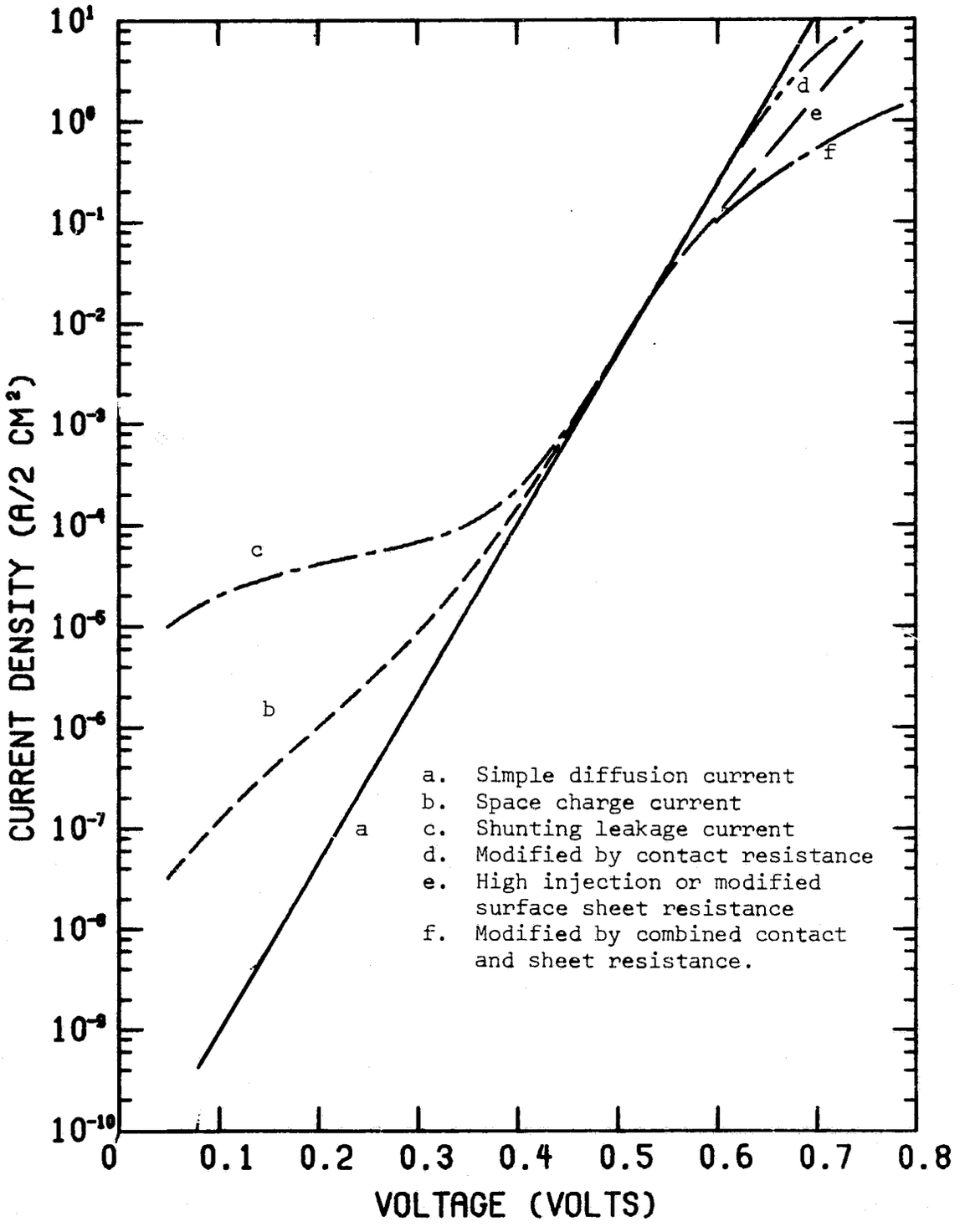

Figure 2.1. Prototype of the dark I-V characteristics of a solar cell.

analytical expressions for J_s has been compiled in Hovel's book [10] for several models with different boundary conditions.

2.2 Space Charge Recombination Current

The generation-recombination current of the Sah-Noyce-Shockley model is given by Equation 2.3 which assumes that the recombination is through a center located in the vicinity of the center of the bandgap.

$$J_\gamma = q_o \int^{W_d} \frac{pn-n_i^2}{\tau_{po}(n+n_1)+\tau_{no}(p+p_1)}\,dx$$

$$\approx \frac{qn_i^2\, W_d[\exp(qV/kT)-1]}{(\tau_{po}n_1+\tau_{no}p_1)+(\tau_{po}+\tau_{no})n_i\exp(qV/2kT)}, \qquad (2.3)$$

$$\approx \frac{qn_iW_d}{\tau_{po}+\tau_{no}} \exp(qV/2kT) \text{ for medium voltages}$$

It is clear that for a silicon p-n junction the space charge recombination current has a diode n factor of two at medium voltages and at room temperature.

2.3 High Injection Current

High injection occurs when the minority carrier density on one side of the junction becomes comparable with the majority carrier density. The calculation of the high injection current indicates an exp(qV/2kT) behavior [11]. High injection is likely to occur for low base doping densities near the junction or for silicon solar cells operating in multi-sun environments. For normal silicon solar cells with resistivities in the range of 10 Ω·cm to 0.1 Ω·cm which operate under one sun power intensity, high injection is unlikely to occur.

2.4 Tunneling Current

A tunneling current may exist in heavily doped junctions with a resistivity of less than 0.01 Ω•cm. The tunneling current takes the form [12]

$$J_T = KN_T \exp(\beta V_j) \tag{2.4}$$

where N_T is the density of energy states available for an electron or hole to tunnel into, and K and β are functions of semiconductor parameters. The n factor for tunneling currents lies between 1.3 and 2 at room temperature [12].

2.5 Leakage Current

Since a solar cell is a relatively large area device, there is a great chance of a leakage channel existing through the imperfect junction, especially under the metal contact [13]. The leakage current can be modeled by a shunting resistor R_{ST} across the junction and the current form is quite simple

$$I_{ST} = \frac{V_j}{R_{ST}}. \tag{2.5}$$

Where V_j is the junction voltage at the imperfection location. As a result of this leaky current, the diode n factor may be very high with values of 3 to 5 being usually observed at voltages less than 0.4 volts.

2.6 Current Voltage Characteristics Modified by Series Resistance

Series resistance becomes important as the current density increases and/or junction depth decreases. The series resistance comes from two sources: the surface sheet resistance and the metal-semiconductors contact resistance. For the contact resistance R_c which appears in series with the cell, the exponential dependence of current on voltage can be

modified by replacing V_J in the exponential with $V_J - R_L I$. For the sheet resistance, however, the two dimensional distributed nature of the current flow does not allow one to define a purely lumped resistance. In this case at large currents the equation becomes [14],

$$I = \sqrt{AJ_s I_T}\, \exp(qV/2kT), \tag{2.6}$$

$$I_T = \frac{2kT}{q} \frac{h^2}{\rho_{ST}} \cdot \frac{1}{A} \tag{2.7}$$

Where A is the total area of the solar cell, J_s is the saturation current density of the simple diffusion theory, ρ_{ST} is the surface sheet resistance and h is the total perimeter of the contact grid pattern.

The parameter I_T has the physical significance that it is the current level at which the characteristic makes a transition from an exp(qV/kT) dependence to an exp(qV/2kT) dependence. In a practical silicon solar cell both sheet resistance and contact resistance may exist simultaneously and the diode n factor may be as high as 5 at voltages greater than 0.5 volts. In this combined case one cannot model the cell correctly by a lumped constant resistance.

3. PARAMETERS FOR DEVICE MODEL

3.1 Diffusion Length and Lifetime

The lifetimes of electrons and holes are of great importance in understanding the electrical and optical behavior of a semiconductor device. For indirect bandgap semiconductors such as silicon, the carrier lifetime is generally high and basically determined by the recombination through intermediate centers within the bandgap instead of direct band-to-band recombination. The minority carrier lifetime has been developed by assuming a single Shockley-Read center as

$$\tau_p = \frac{1}{\sigma_p V_{th} N_R}\left[\left(1 + \frac{N_c}{n_{no}} \exp[-(E_C-E_R)/kT]\right) + \frac{\sigma_p}{\sigma_n}\frac{N_V}{n_{no}} \exp[-(E_R-E_V)kT]\right] \quad (3.1)$$

Where τ_p = hole lifetime in n-type semiconductor with doping density N_{no},

N_R = density of recombination centers,

σ_p, σ_n = hole and electron capture coefficients.

A similar form can be written for electrons in p-type material. Equation 3.1 indicates that the minority carrier lifetime is lower in general for a higher doping density. This behavior of minority carrier lifetime with doping density has been experimentally observed [16,17].

Some representative curves of measured diffusion lengths as a function of doping density are shown in Figure 3.1 [16]. The comparisons to other experimental data are also shown on the same graph [18,19,20,21]. At high doping densities band-to-band Auger recombination may become the dominant recombination process. This gives a decreasing lifetime which is inversely proportional to the square of the doping density. The experimental curve of L_D(MAX) in Figure 3.1 has a lifetime dependence on doping density with an exponent of -1.7 at doping densities greater than $10^{17}/cm^3$. This value is close to the theoretical band-to-band Auger lifetime model which has an exponent of -2.

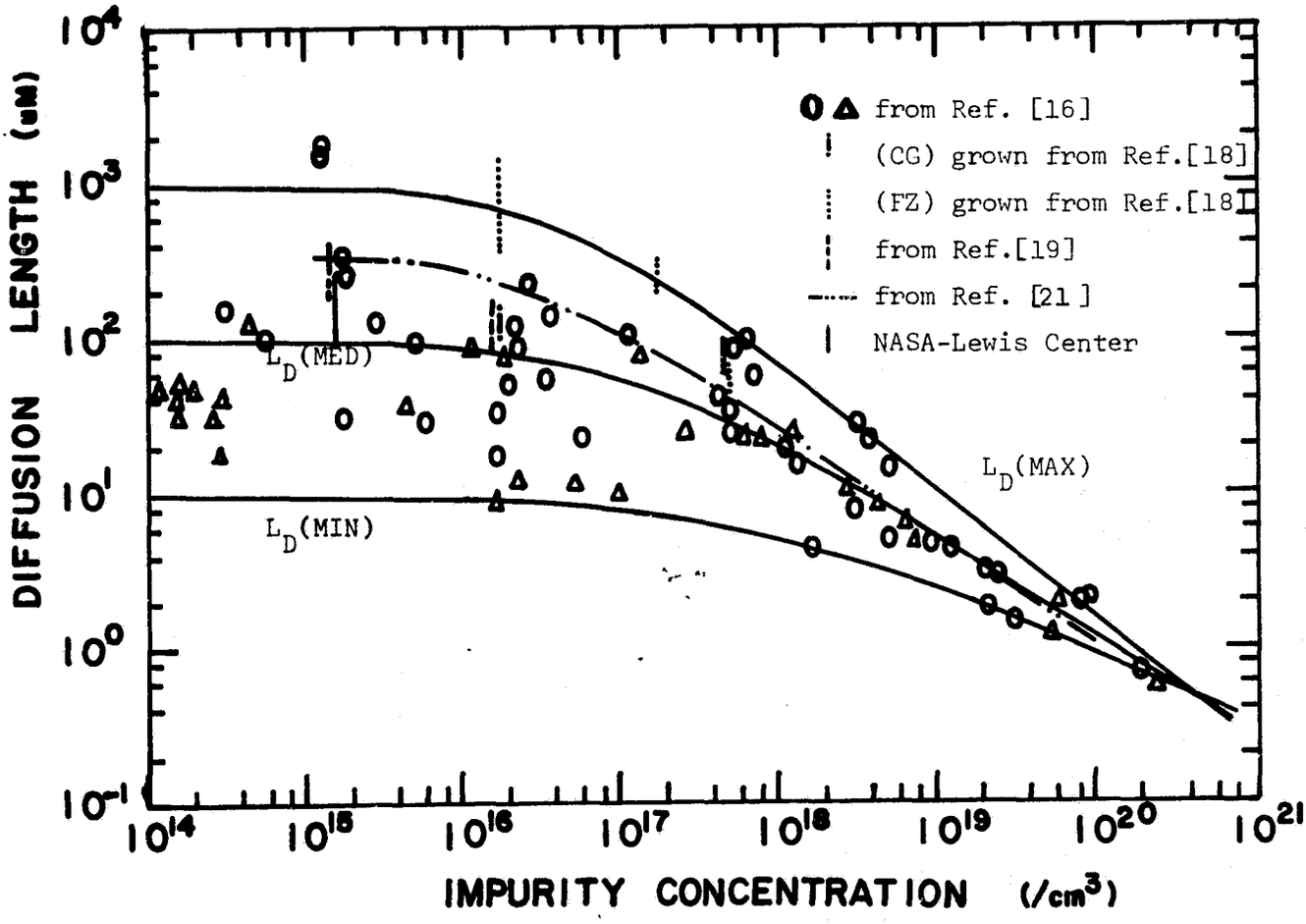

Figure 3.1. Model of the diffusion length and comparison to the experimental data. All experimental data are for p-type material except those marked by the triangle.

Hence it is a fiarly good approximation to define L_D(MAX) and L_D(MED) of Figure 3.1 as the upper and lower bounds for electron diffusion length in p-type silicon. Similarly L_D(MED) and L_D(MIN) of Figure 3.1 could be considered as upper and lower bounds for hole diffusion length in n-type silicon because of the lower hole mobility. In a practical silicon solar cell, the actual diffusion length may vary between some upper and lower bound depending on the material perfection and the fabrication processes. In a solar cell the density of recombination centers is generally much smaller than the doping density, hence the majority carrier lifetime equals that of the minority carriers [22].

Although the diffusion length data of Figure 3.1 was measured in bulk material, it is assumed valid for the shallow diffused layer of solar cells. If the lifetime is a function of total doping density only such as in the Auger process this will be a good approximation. However, this may not be valid if lifetime is dominated by deep level impurity recombination.

3.2 Surface Recombination Velocity

In addition to the bulk recombination, surface recombination is another loss mechanism which is modeled by a surface recombination velocity S. The minority carrier current flow toward the surface is given as

$$J_s = q\Delta p_s S, \tag{3.2}$$

where Δp_s is the surface excess minority carrier density.

The value of S is basically determined by surface conditions such as the density of interface states, any anti-reflection oxide layer and surface treatments. Very low S values of 10^2 cm/sec can probably be achieved only through the use of high temperature oxidation processes which may cause a drive-in of the surface diffused layer and may not

be compatible with solar cell technology. Hence a value of 10^3 cm/sec may be a lower limit for SRV of typical oxide coated solar cells.

3.3 Diffusion Doping Profile

It has been found that shallow diffusions ($\leq$ 1 μm) of phosphorous in silicon result in considerable deviations from the simple diffusion theory of an erfc function [26,27]. For short diffusion times ($\leq$ 1 hr) and temperature below 1100°C, it has been found that a constant concentration layer exists near the surface of about 1/3 ∿ 1/4 of the junction depth and the electrical active phosphorous concentration in this layer is about half of the solid solubility limit at the particular diffusion temperature. Beyond the constant concentration region, the diffusion profile can be reasonably well represented by a complementary error function. One of the typical diffusion profiles is reproduced here in Figure 3.2 [27]. The parameters which characterize this particular diffusion profile are the surface doping density C_s, width of the constant doping layer X_c and the doping density C_B at the boundary of the constant doping and the erfc doping profile.

3.4 Mobility

Two major contributions to mobility are phonon scattering and impurity scattering. These effects make mobilities a function of doping density, temperature and internal electric field intensity. The general empirical equation developed by Gummel [28] was used in this work.

$$\left(\frac{\mu_o}{\mu}\right)^2 = 1 + \frac{N_D}{\frac{N_D}{S} + N} + \frac{(E/A)^2}{E/A + F} + \left(\frac{E}{B}\right)^2 \qquad (3.3)$$

This equation has been confirmed by measuring the relations between drift velocity and electric field [29].

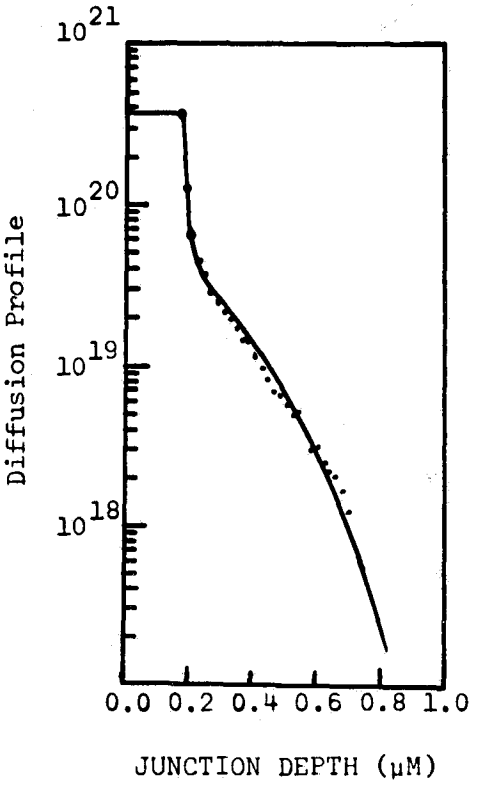

Figure 3.2. One sample of the shallow phosphorous diffused profile at 900°C. Ref. [26]

3.5 Heavy Doping Effects

Heavy doping phenomena occurs in silicon for total doping densities above about $10^{19}/cm^3$. The high doping effect on minority carriers can be represented by a bandgap reduction where the empirical expression of Equation 3.4 has been used in this work.

$$\Delta E_G = -0.45\sqrt{N/(10^{21}cm^{-3})} \quad (eV), \tag{3.4}$$

In this expression, N is the net doping density.

3.6 Absorption Coefficient

The ability of a semiconductor to absorb light of a given wavelength is characterized by the absorption coefficient α. Values of the absorption constant α were taken from Dash and Newman [30] up to about 0.95 μm wavelength. At wavelength above 0.95 μm there is considerable variation in the reported absorption coefficient values. Several reported values at 0.95 μm, 1.0 μm and 1.1 μm are shown in Table 3.1 [30-35]. The data of Dash and Newman is seen to be larger than most of the reported data at 0.95 μm and 1.0 μm. Good agreement in the long wavelength spectral response of solar cells could not be obtained by using the data of Dash and Newman. Best results have been obtained by using the values of the last line which are intermediate between the largest and smallest reported experimental values. Thus the absorption data which has been used is that of Dash and Newman with the data at 0.95 μm, 1.0 μm and 1.1 μm modified to the values of Table 3.1. The index of refraction as a function of incident wavelength was taken from Phillip (1972) [36].

Table 3.1 Comparison of reported absorption coefficient values at long wavelengths.

		1.1 μm	1.0 μm	0.95 μm
		Absorption Coefficient (cm^{-1})		
[30]	Dash & Newman	7	100	220
[31]	Vedam	-	-	270
[32]	Runyan	-	67	170
[33]	Vol'fson & Subashiev	-	64	150
[34]	Macfarlon	3.9	61	-
This work		3.9	74	204

3.7 Spectral Response

The spectral sensitivity of a solar cell to incident photons is measured by the spectral response or the quantum yield. For a practical solar cell the quantum yield is always less than unity because of surface reflection-losses and internal recombination losses.

Internal quantum yield can be defined as the ratio of the collected short circuit current density to the input current density which is generated by the incident photons assuming 100 percent transmission through the surface, i.e.

$$QY(\lambda) = \frac{I_{SC}(\lambda)}{qF(\lambda)(1-R(\lambda)-A(\lambda))(1-e^{-W_d\alpha(\lambda)})}, \qquad (3.5)$$

where $F(\lambda)$ = incident photon flux (proportional to input power density),

$R(\lambda)$ = reflection at surface,

$A(\lambda)$ = absorption in AR layer if any,

W_d = device thickness.

Another practical parameter is the external quantum yield $QY_{ext}(\lambda)$ which includes losses due to surface reflection and antireflecting layer absorption:

$$QY_{ext}(\lambda) = \frac{I_{sc}(\lambda)}{qF(\lambda)(1-e^{-W_d\alpha W})} \tag{3.6}$$

The spectral response is represented by the ratio of collected current to input power density as:

$$SR(\lambda)_{ext} = \frac{I_{SC}(\lambda)}{P_{input}} . \tag{3.7}$$

The spectral response theory of Prince and Wolf [37] shows that the overall spectral responses can be considered as made up of somewhat independent responses from the surface and base layers. Hence it is sometimes useful to specify the spectral response from the surface region, depletion region and base region respectively as

$$SR_{ext}(\lambda) = SR_{ext}(\lambda,\text{surface})+SR_{ext}(\lambda,\text{depletion})+SR_{ext}(\lambda,\text{base}). \tag{3.8}$$

Some of the parameters and results of the spectral response analysis are shown in Table 3.2.

The calculated reflectance R in Table 3.2 is in direct agreement with Phillips data of oxide free silicon [36], although it is well known that a thin layer of oxide of about 20 $\sim$ 35Å in thickness may be grown on an exposed bare silicon surface. The correction on R due to such a layer is less than 1 percent for photon wavelengths of 0.4 to 1.0 micrometer (This also agrees with Ref. [36].).

For Tantalum oxide calculations, a reflection index of 2.20 was used which is based upon ellipsometry measurements performed at a wavelength of 5461Å [38]. This value of reflection index is in general agreement with reported literature values [39].

Table 3.2. Parameters for spectral response calculation at various wavelengths.

λ	0.4	0.45	0.5	0.6	0.7	0.8	0.9	0.95	1.0
Absorption Coeff. (cm^{-1})	8.70E4	2.62E4	1.23E4	4.56E3	2.10E3	9.64E2	3.67E2	2.04E2	7.42E1
Photon Energy IeV)	3.09	2.75	2.47	2.06	1.77	1.54	1.37	1.30	1.24
Transmission for Bare S_i	0.521	0.583	0.615	0.647	0.663	0.672	0.679	0.681	0.683
Reflection for Bare S_i	0.478	0.416	0.384	0.352	0.336	0.327	0.318	0.318	0.316
INPUT POWER (mW)	10	10	10	10	10	10	10	10	10
Surface Rate ($\#/cm^2$)	9.15E20	3.47E20	1.91E20	8.91E19	4.91E19	2.61E19	1.13E19	6.65E18	2.55E18
INCIDENT CURRENT (mA/cm^2)	3.226	3.629	4.032	4.839	5.646	6.452	7.259	7.662	8.065

The calculated transmission and reflection coefficients for Ta_2O_5 are shown in Figure 3.3 which indicates a much better surface efficiency at short wavelength as compared to the bare Si, SiO or SiO_2 coated surface. Since the AMO power spectrum peaks between 0.4 μm to 0.6 μm, Ta_2O_5 is superior to the other oxides studied.

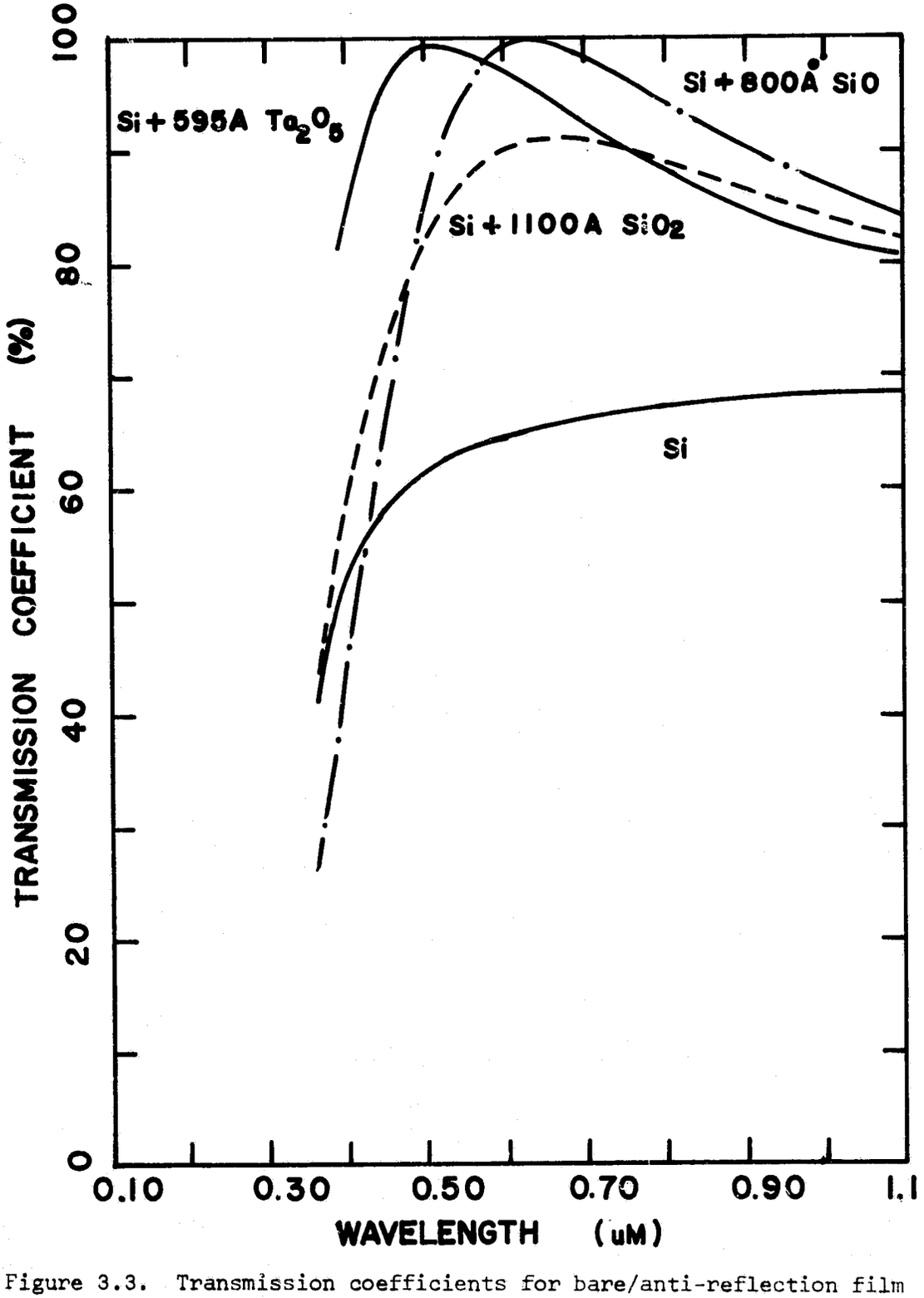

Figure 3.3. Transmission coefficients for bare/anti-reflection film coated silicon surface at wavelength 0.35 μM to 1.1 μM.

4. GENERAL COMPARISON OF THEORETICAL AND EXPERIMENTAL RESULTS

The solar cells which have been studied can be broadly divided into three categories based upon the origin of the bulk material and the cell design. The first category consists of n^+p cells on 0.1 Ω·cm base layers with a finished thickness of about 6 mils. The second category consists of n^+p cells on 10 Ω·cm base layers with thicknesses of about 10.5 mils. Both types of cells were made in a standard 2 cm^2 area and use a NASA-Lewis Research Center 10-finger grid. No anti-reflection layers were present on the silicon surface.

The third type of cell is the Aluminum BSF cell on 16 Ω·cm substrates with a finished cell thickness of about 6.5 mils. These cells have a Ta_2O_5 coating about 595Å in thickness and a 5 mil "Teflon" FEP cover on the Tantalum Pentoxide. On these the nine finger grid pattern of Spectro Lab was present.

The n-type surface layers were phosphorous diffusion, using $POCl_3$ at the NASA-Lewis Research Center. The temperature and the duration of the diffusion process are described for each type of cell in the following sections. The top and bottom contacts were made using metal masks and by evaporating a thin layer of Aluminum (200∿500Å) followed by the evaporation of about 3 to 5 micrometers of silver on the surface. The contacts were then sintered at temperatures of 550 to 650°C in H_2.

Al-Ag contacts have been found to have less degradation in the cell electrical characteristics than that which occurs for sintered Ag-Ti contacts, although Ti makes a better ohmic contact than Al. For BSF cells the Aluminum was alloyed at about 800°C for one hour or less and this produced a high-low junction of 0.5 to 1.0 μm in depth [40].

4.1 Results of Type One Cells

4.1.1 Simulation Model

These cells were made from 0.1 Ω·cm Boron doped wafers with a doping density of $5x10^{17}/cm^3$. The surface was diffused at 950°C for 60 minutes forming a junction with a depth of about 1 μm. The model for the surface diffused profile was taken from the empirical results of Tai [27] with the parameters C_s, C_B and X_c taken to be $4x10^{20}/cm^3$, $8x10^{19}/cm^2$ and 0.4 μm respectively as has been previously described.

The minority carrier diffusion length of the base region L_B was measured at NASA-Lewis by the X-ray method. An accurate model for the surface diffusion length is more difficult to simulate because of the lack of experimental data. Considerable variation in the base layer minority carrier diffusion length was noted from wafer to wafer in the same run and among groups of diffusion. Thus it is reasonable to model the surface diffusion length as a variable function of doping density between the measured upper and lower bound of $L_{D(MED)}$ and $L_{D(MIN)}$ for bulk n^+-type layers. The final value of surface layer diffusion length was selected on the basis of comparing the theoretical results with the experimental data.

4.1.2 Comparison of Model and Experiment

Three sets of simulated results will be described which include dark I-V characteristics, spectral response and photovoltaic I-V characteristics. The simulated model and results are shown in Tables 4.3 and 4.4.

The ideal diffusion theory is found to be generally true as can be seen in Figures 4.1, 4.2, 4.3. The diode n factor is quite close to 1 as seen in Table 4.1 which shows calculated values at voltages near V_{oc} and V_{max}.

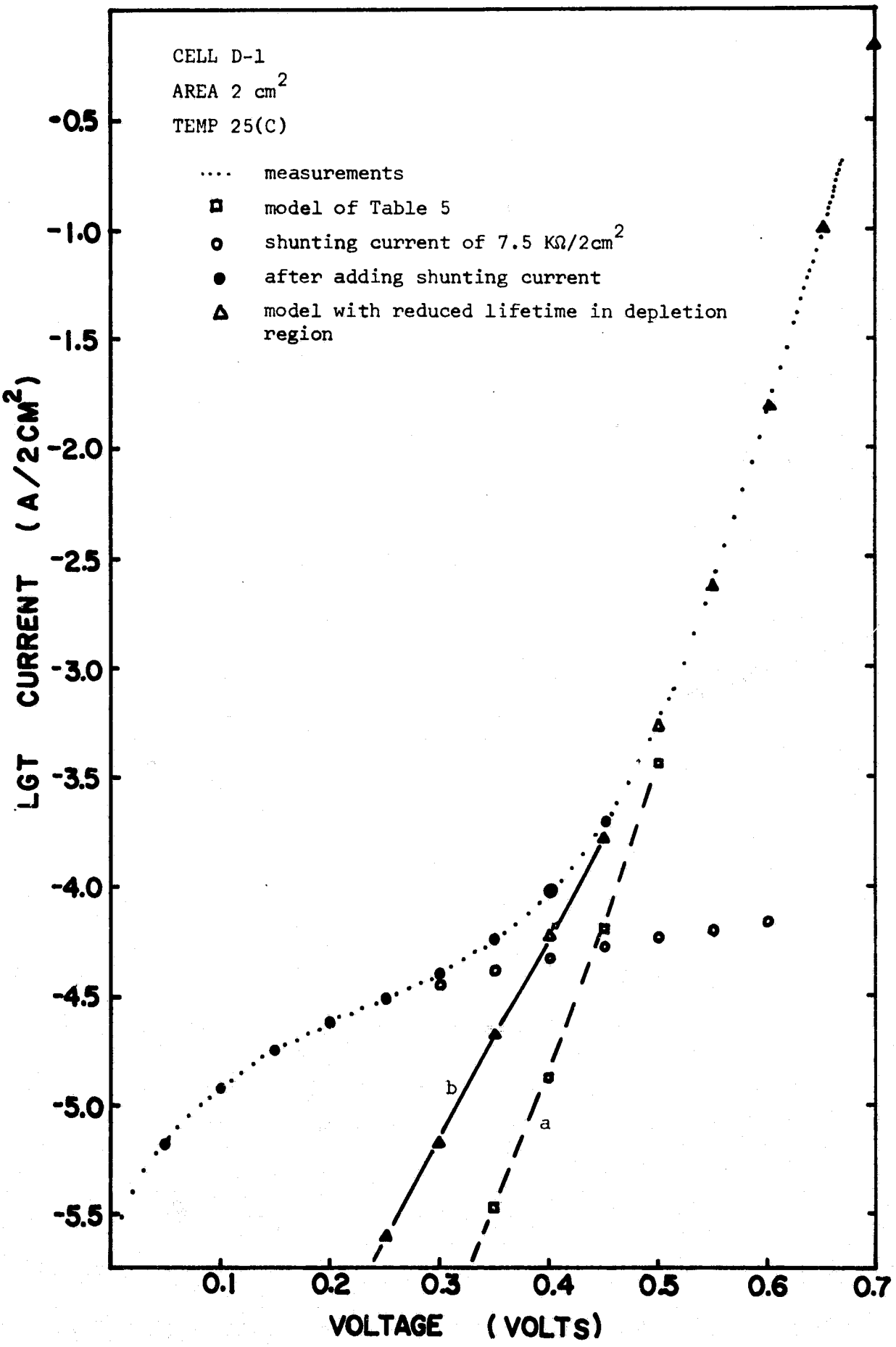

Figure 4.1. Comparison of the dark I-V characteristics of Cell D-1.

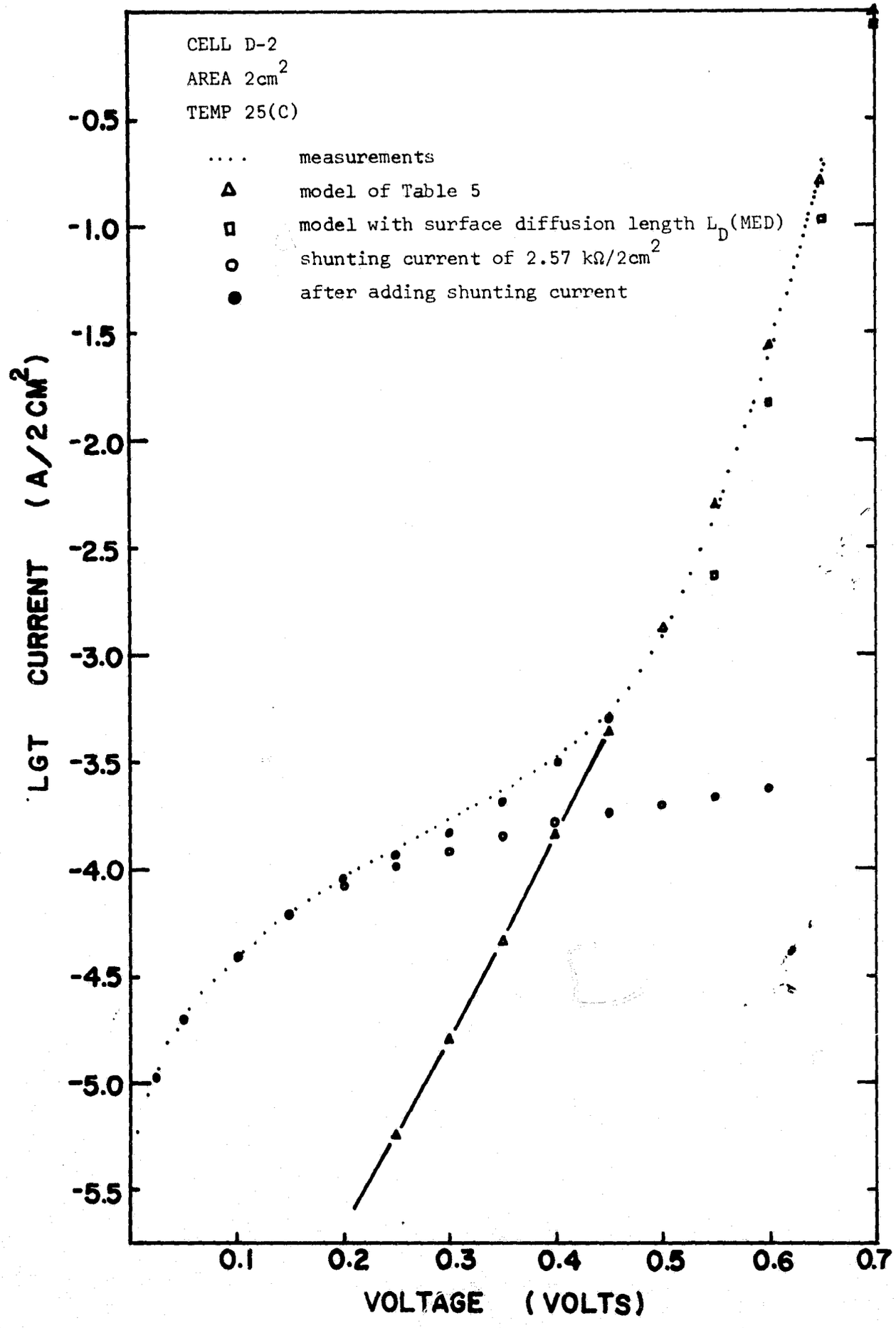

Figure 4.2. Comparison of the dark I-V characteristics of Cell D-2.

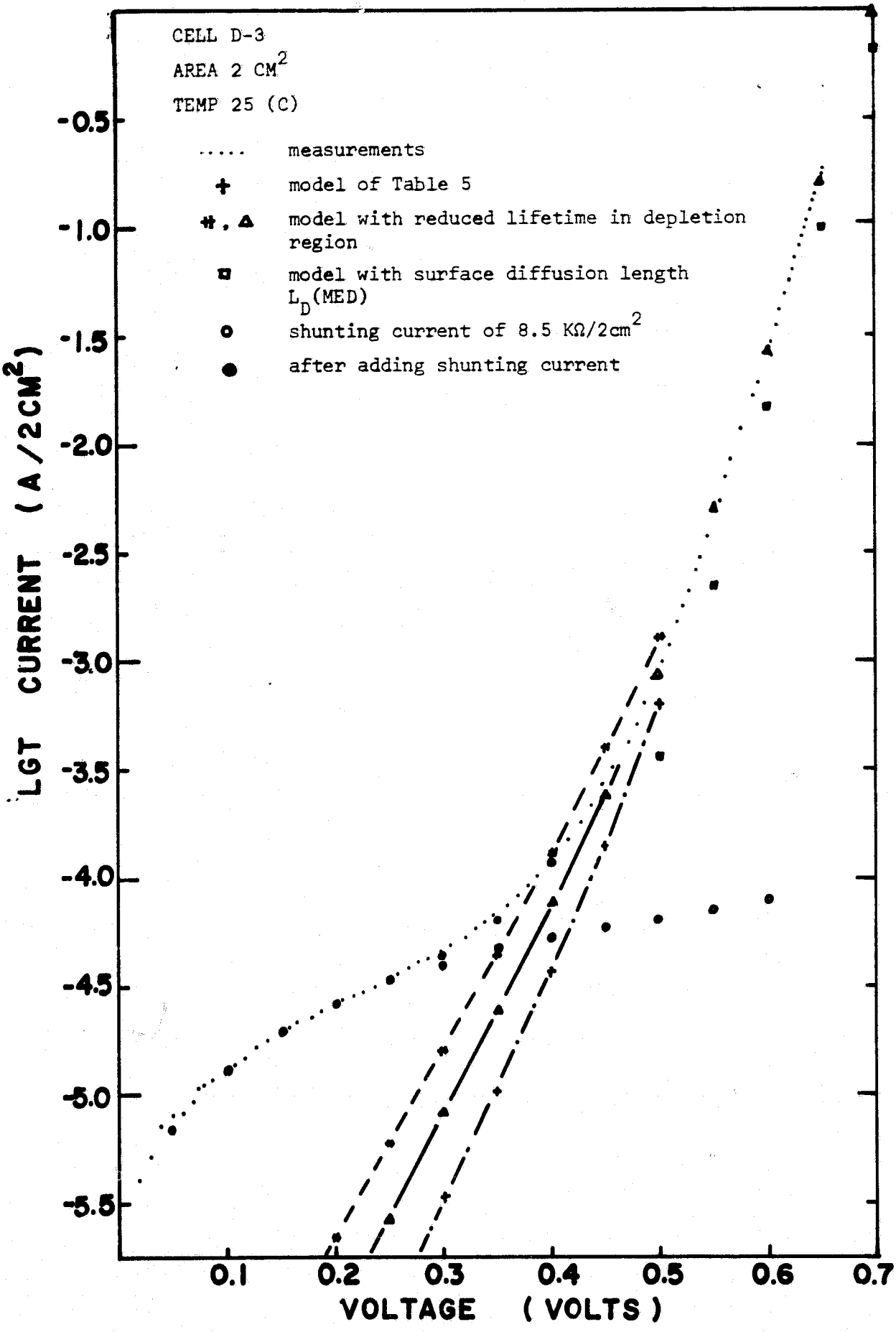

Figure 4.3. Comparison of the dark I-V characteristics of Cell D-3.

Table 4.1. Calculated diode n factors

Evaluated near	n for device number		
	D-2	D-3	D-1
V_{oc}	1.11	1.08	1.02
V_{max}	1.33	1.12	1.05

Table 4.2. Fraction of dark current at selected depths below surface.

		R values at selected voltages (volts)				
Position	x(μm)	0.3	0.4	0.5	0.6	0.7
Surface Region	0.1	0.000	0.002	0.010	0.031	0.049
	0.3	0.002	0.000	0.049	0.147	0.238
	0.5	0.003	0.017	0.081	0.243	0.393
	0.9	0.003	0.019	0.091	0.270	0.437
	1.0	0.216	0.255	0.323	0.435	0.522
Depletion Region	1.12	0.998	0.990	0.953	0.533	0.545
Base Region	7	0.998	0.991	0.958	0.873	0.794
	30	0.999	0.994	0.972	0.918	0.867
	83	1.000	0.999	0.994	0.982	0.971
	130	1.000	1.000	0.999	0.998	0.998
	150	1.000	1.000	1.000	1.000	1.000

Table 4.3. Device model of type one cells.

Structure	D-1 n^+p, 0.1Ω·cm	D-2 n^+p, 0.1Ω·cm	D-3	D-1-1	D-1-2	D-1-3
(μm) Junction depth	1.	1.	1.	1.	0.2	0.2
Surface doping	$4x10^{20}$	$4x10^{20}$	$4x10^{20}$	$4x10^{20}$	$2x10^{20}$	$2x10^{19}$
Surface profile	Experimental	Exp.	Exp.	Exp.	erfc	erfc
Base diffusion length	75	60	105	75	75	$L_{D(MAX)}$
Surface diffusion length	$L_{D(MED)}$	$L_{D(MIN)}$	$L_{D(MIN)}$	$L_{D(MIN)}$	$L_{D(MED)}$	$L_{D(MED)}$
Surface Recomb. Velocity	10^5	10^5	10^5	10^5	10^3	10^3
Anti-reflection layer	No	No	No	5%	5%	5%
Device thickness	150	150	150	150	150	150
Two-way reflection	Yes	Yes	Yes	Yes	Yes	Yes

Table 4.4. Calculated results of type one cells

	D-1-1	D-1-2	D-1-3
VOC (volts)	0.631	0.674	0.690
I_{SC} (mA/cm^2)	29.41	41.44	42.56
VM (volts)	0.554	0.596	0.606
IM (mA/cm^2)	27.57	39.36	40.81
PM (mW)	15.27	23.46	24.73
CFF	0.823	0.840	0.842
EFF	11.29	17.34	18.28

The deviation from the ideal n value is due to the space charge recombination current within the depletion region. The relative contributions of space charge recombination current and diffusion current can be clearly revealed by looking at the normalized integral of the recombination as a function of position. This is shown in Table 4.2, where

$$R = \frac{\int_o^x U(x)dx}{\int_o^W U(x)dx},$$

and U is the net generation-recombination rate.

For example the base layer and surface layer diffusion current comprise 53.3 percent and 43.5 percent respectively of the total current density, while space charge recombination current accounts for only 10 percent of the total current at 0.6 volts. Also it is clear from the data that recombination current from the depletion region dominates at lower voltage.

The devices with a deep junction and low base layer resistivity provides a good test for simulation of the surface diffusion length because of the large dark current and the high spectral response of the surface region. The response of high resistivity cells with shallow junction are much more dominated by the base diffusion current. The fairly high n value of 1.33 of device D-2 is due to a low shunting resistance as can be seen from Figure 4.2.

The spectral response results for the same cells are shown in Figure 4.4, 4.5 and 4.6. The agreement between theory and experiment is fairly good in all ranges of wavelength from 0.4 μm to 1.0 μm. Since the base region dominates the long wavelength response, the response in this range provides an independent check of the base diffusion length. Indeed the base diffusion lengths which give the best spectral response

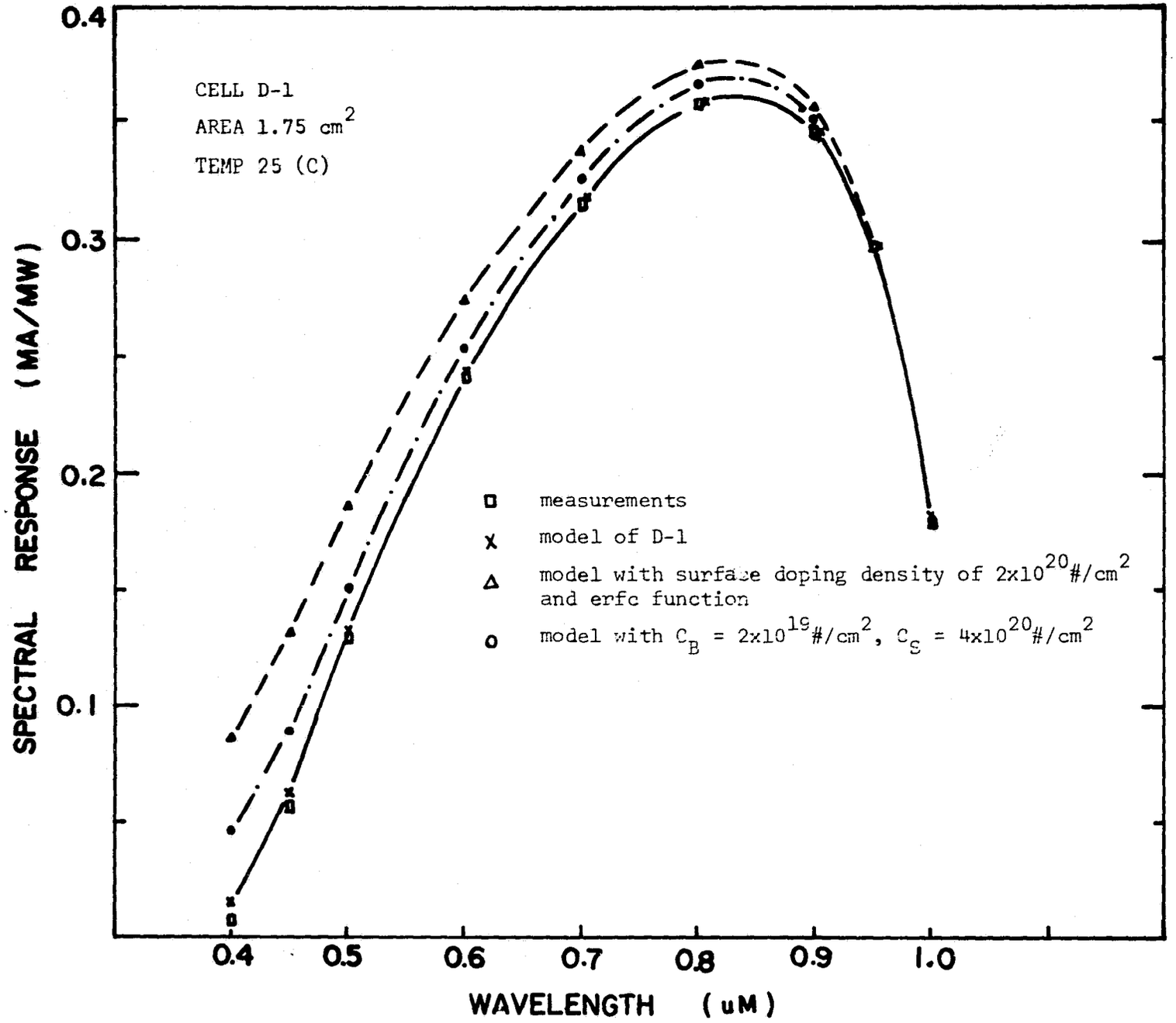

Figure 4.4. Comparison of the spectral response of Cell D-1.

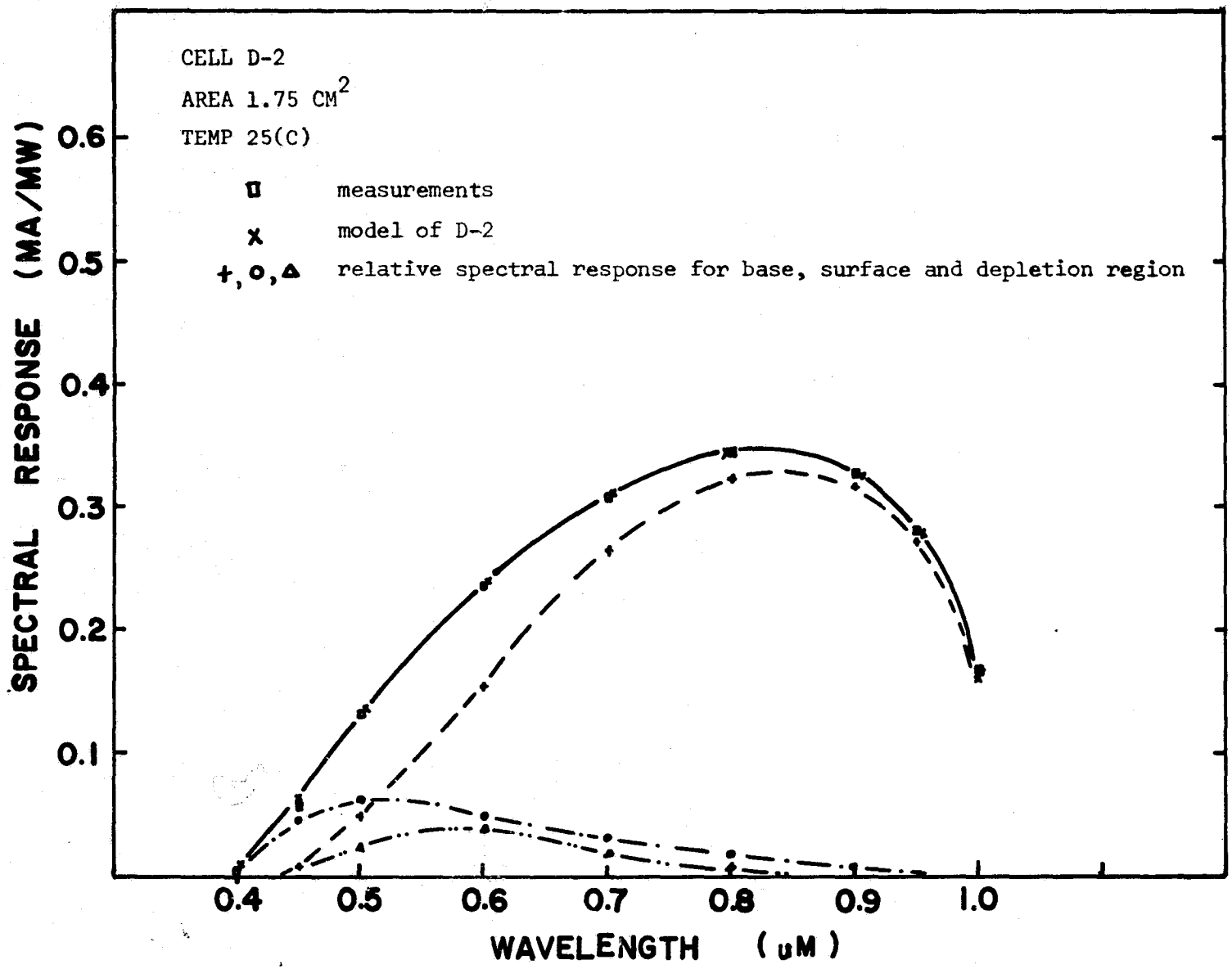

Figure 4.5. Comparison of the spectral response of D-2.

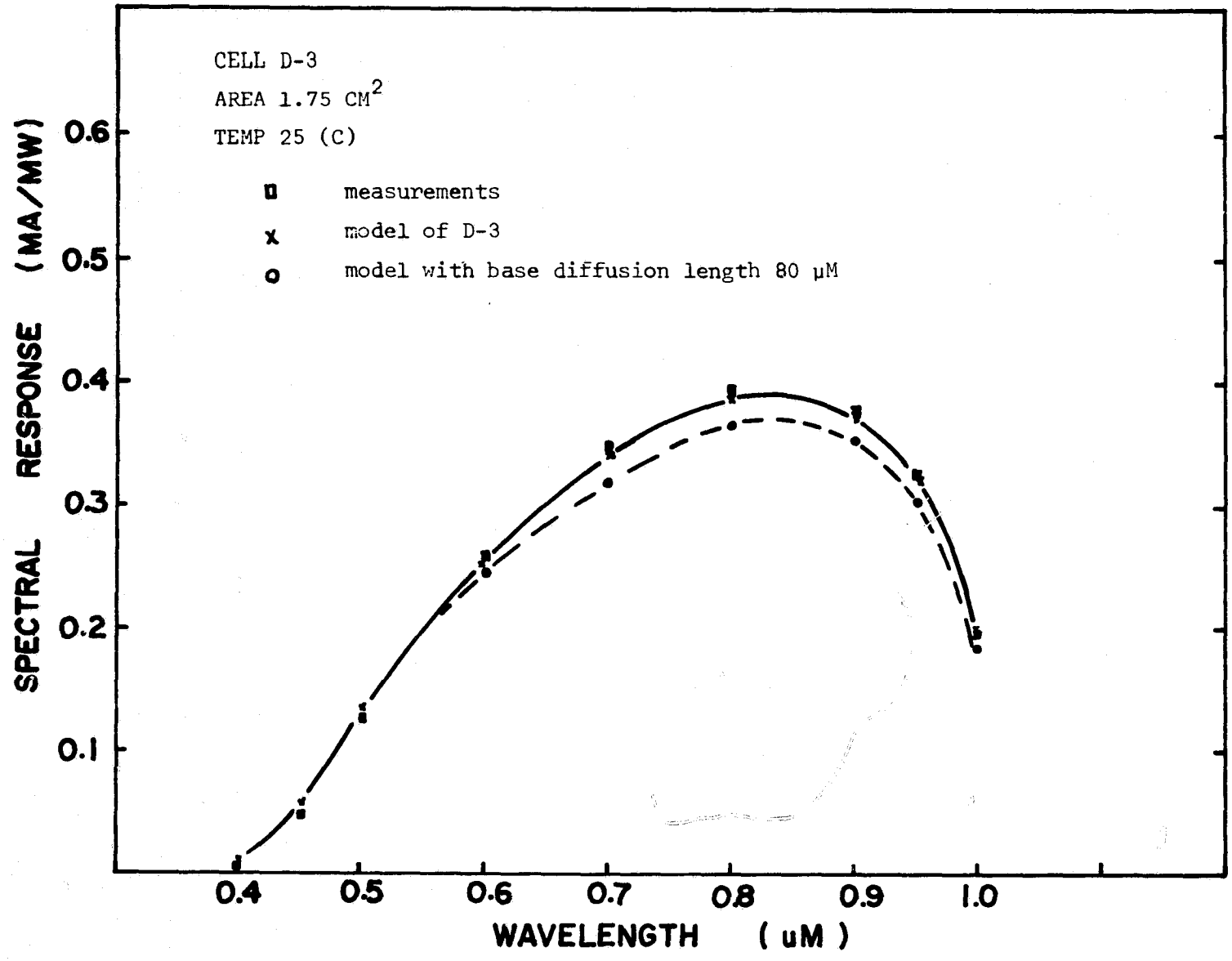

Figure 4.6. Comparison of the spectral response of Cell D-3.

were found to be close to the experimental measured value for the low L_B/W_B ratio devices of D-1 and D-2. However it was found that a higher diffusion length of 105 μm instead of 80 μm value measured by the X-ray method was a better choice for fitting the experimental results for device D-3.

The discrepancy may result from an unknown bottom surface recombination velocity which influences the measured short circuit current density of the X-ray method for $L_B/W_B \sim 1$. This point will be discussed in more detail in the section on BSF cells. The matching of data points for short wavelength is due largely to the diffused layer properties near the surface. In particular the combinations of heavy doping effects, high SRV and low lifetime and mobility near the surface lead to a very low collection efficiency within a thin layer near the surface.

Historically, a dead layer was postulated as a thin layer adjacent to the front surface which had a very short lifetime. The thickness of this dead layer was about 1/4 to 1/3 of the junction depth. Within this layer where the diffusion transit time was less than the lifetime [41] the collection efficiency was postulated to be very low. An alternative explanation of the dead layer effect has been proposed. In this model it it argued that the retrogate drift field resulting from heavy doping effects near the surface prevents carrier collection from a thin surface layer [42].

In the present calculations the diffused surface layer was approximated by a constantly doped surface layer followed by an erfc profile such as seen in Figure 3.2. For the particular example discussed at present this results in a retrograde field over a distance of 0.61 μm from the surface, while the constantly doped region extends over a depth of 0.40 μm. The detailed

computer calculations have indicated that in this case the short circuit current density in the surface layer reverses sign at a depth of 0.50 μm. Thus the actual width of an effective dead layer is between the depth of the constantly doped region and the point at which the field reverses sign.

The results obtained in this work are consistent with the fact that the dead layer like model is necessary to exaplain the poor short wavelength response. In the present model this layer is due to the combined effects of diffusion profile, heavy doping retrogade field effects and low lifetime. To improve the optical response of short wavelength photons this surface layer must be reduced and/or eliminated. Design improvements using shallow junction depths, a lower surface doping density, lower SRV and good surface lifetime will lead to an enhanced short wavelength response and better conversion efficiency for a solar cell.

Shown in Fig. 4.5 is the relative spectral response for the surface, the depletion and base regions. It is clear in the figure that the surface and base region dominate the short and long wavelength response respectively. The depletion region is at its highest response at photon energies where the penetration depth roughly approximates the depletion region depth.

Three photovoltaic I-V characteristics are shown in Figures 4.7, 4.8 and 4.9. The one dimensional calculations were shown for reference and as ideal upper limits for the particular device. The results of the two dimensional analysis are in good agreement with the experimental data. A sheet resistance value of 8Ω was calculated which is in agreement with the experimental determined value of 9Ω. Also a total contact resistance value of $4 \times 10^{-7}\Omega$ was used which gives a negligible voltage drop across the contact area. In fact there is a negligible effect for contact resistances below $10^{-3}\Omega$. The details of the two-dimensional models are discussed in Appendix 9.2.

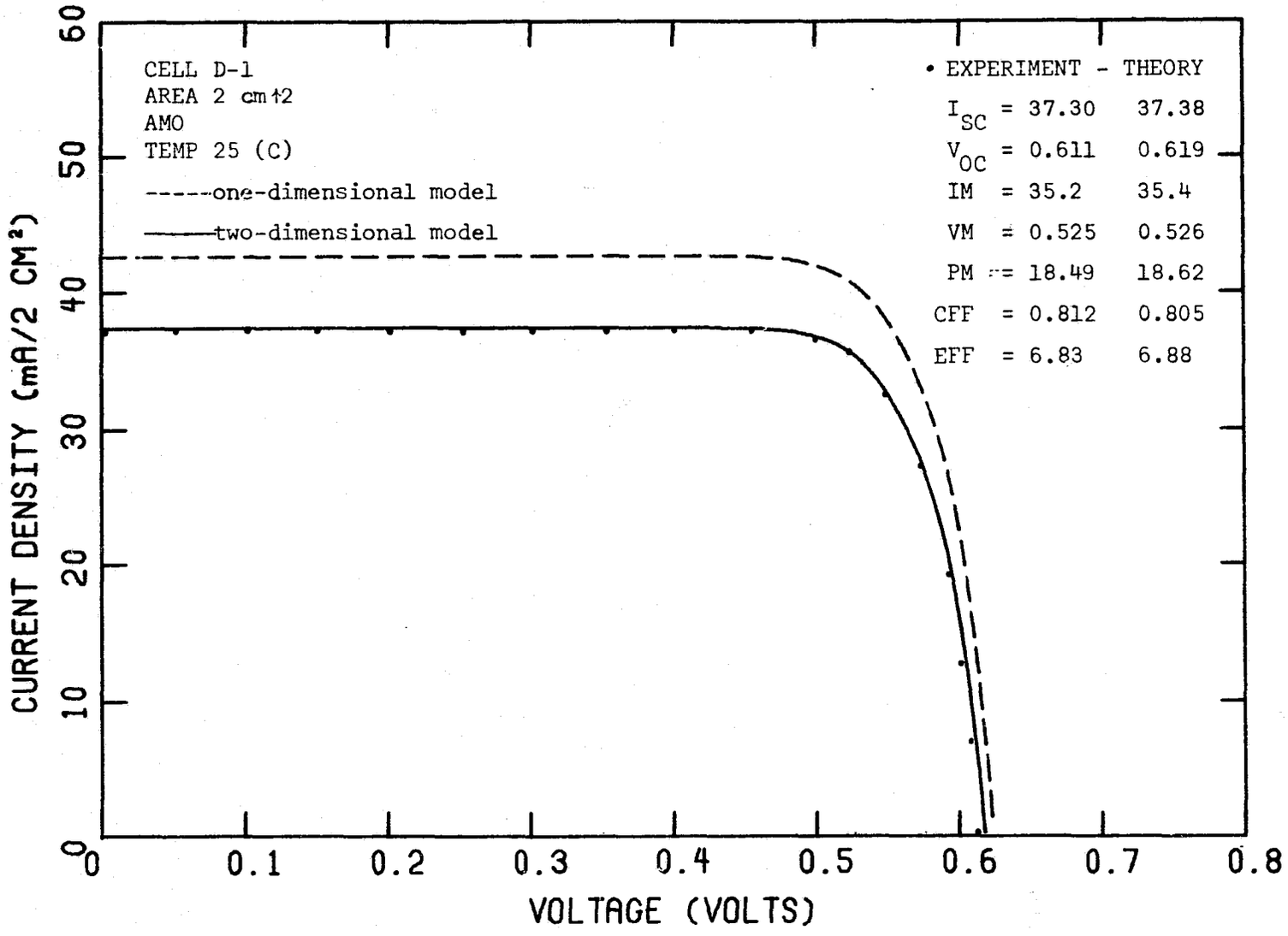

Figure 4.7. Comparison of the photovoltaic I-V characteristics of Cell D-1.

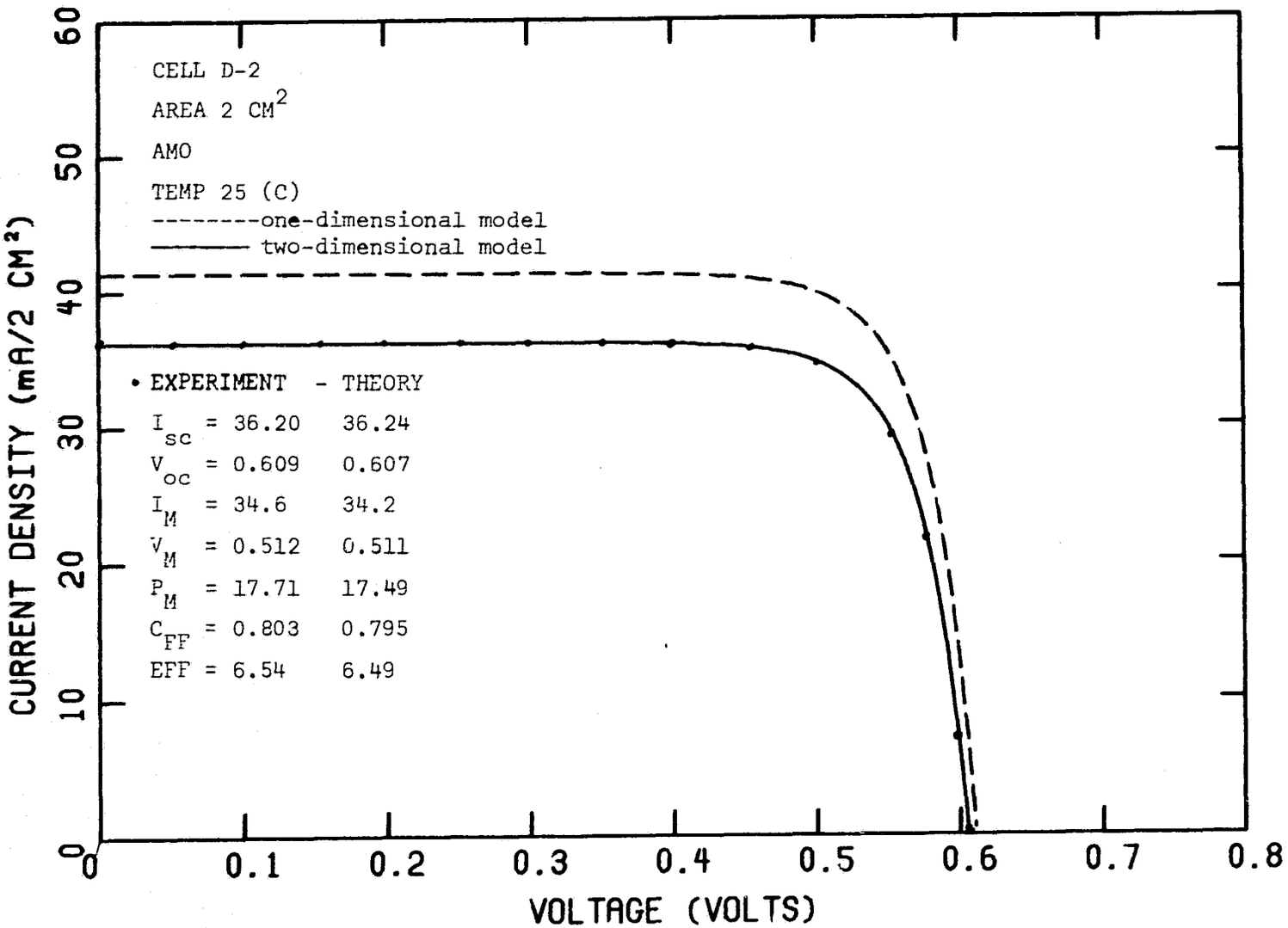

Figure 4.8. Comparison of the photovoltaic I-V characteristics.

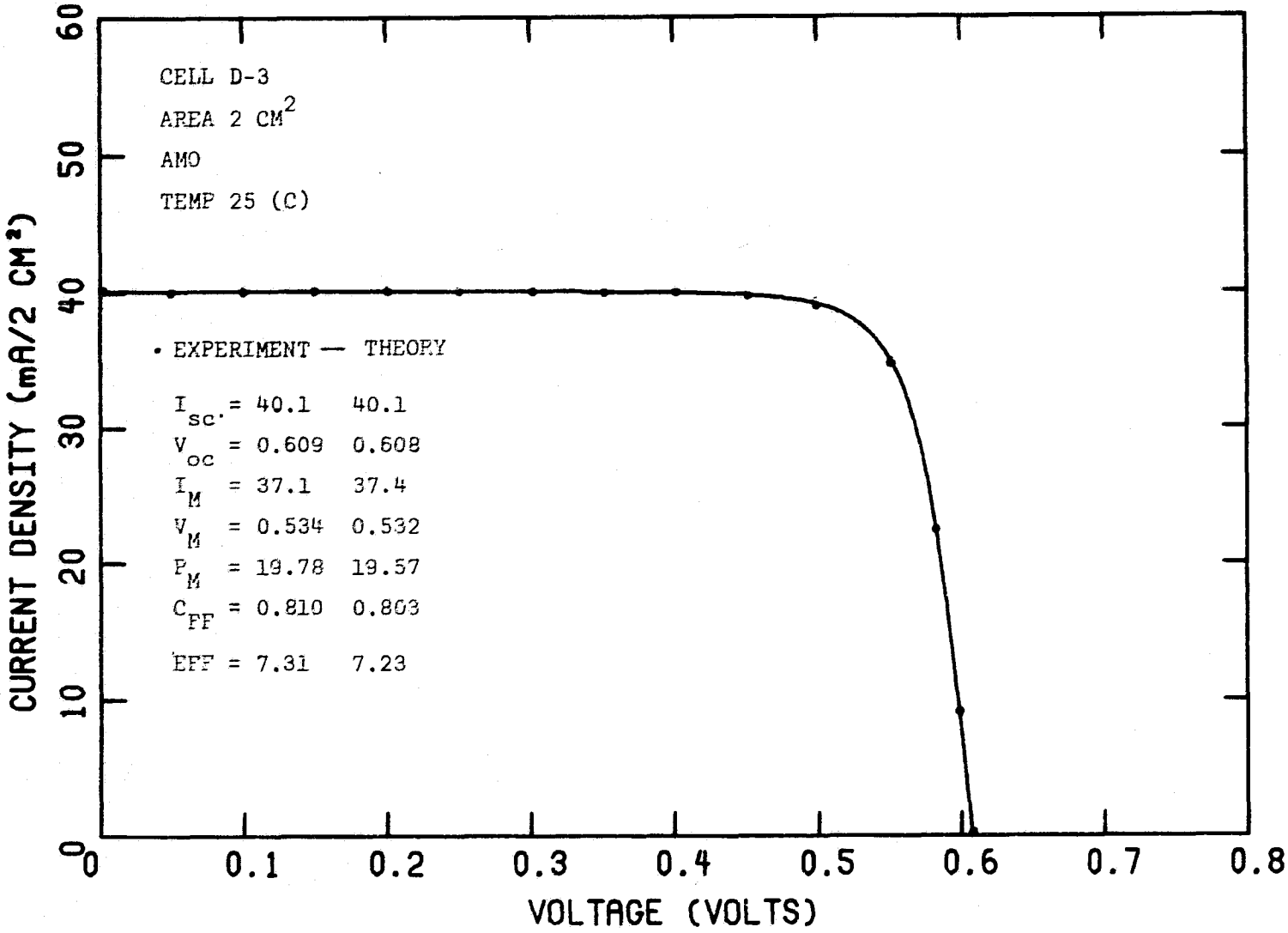

Figure 4.9. Comparison of the photovoltaic I-V characteristics.

4.1.3 Excess Current Density at Voltages Less than 0.4 Volts and the Keldysh-Franz Effect

The forward dark current density of silicon solar cells usually shows an excess current density at voltages lower than 0.4 volts. The diode n factor in this region may be as large as 2 to 5. If this excess current density extends up to the open circuit voltage, it degrades the power output by reducing the curve factor and output voltage. The degradation becomes severe at low illumination intensities.

Many explanations have been proposed for this excess current; however, no one seems entirely satisfactory. Goetzberger and Shockley [43] and Queisser [44] have suggested that the excess current results from metal precipitates within the depletion region. They have also reported that the density of metal precipitate can be reduced by using gettering materials or proper annealing processes. This explanation is similar to Sah's modified p-n junction theory where space charge recombination current accounts for n factors of 2 only. Tunneling current has been ruled out for normal silicon solar cells with resistivity in the range of 10 Ω•cm to 0.1 Ω•cm.

Surface or edge leakage current has also been proposed as a possible source of excess current [45]. An equation for surface leakage current has been deduced of the form

$$I = \pm I_L(e^{qV/kT} - \frac{qV}{kT} - 1)^{1/2}$$

where positive and negative signs represent forward and reverse bias respectively. It is clear that this equation has an n factor of 2 for voltages in the range of 0.1-0.4 volts. Thus this cannot explain the observed high n factors of many silicon solar cells.

Since the internal electric field is higher at lower voltages a physical process which causes higher recombination current at lower voltages might explain the high n factors. With this in mind the Franz-Keldysh effect has been proposed to explain the excess current in solar cells. In 1958 Franz [46] and Keldysh [47] independently predicted an optical bandgap reduction with a strong electric field of magnitude

$$\Delta\mathcal{E}_g = [\frac{\hbar^2}{2\pi m^*}(qE)^2]^{1/3}. \tag{4.1}$$

This effect has been observed experimentally and is now an accepted physical effect. The experiment of Britsyn and Smirnov [48] confirmed the functional dependence of bandgap reduction on electric field, although their results of a reduction of 0.05 to 0.14 eV in the bandgap at an electric field intensity of 1 to 5×10^4 V/cm are not in agreement with the magnitude of the above theoretical prediction.

This model predicts that the space charge recombination current will increase by a factor of $\exp(\Delta\mathcal{E}_g/2kT)$ as

$$I_R = \frac{qn_i}{\tau_{po}\tau_{no}} W_D \frac{2\sinh(qV_J/2kT)}{(V_o-V_J)q/kT} \cdot f(b) \cdot \exp(q\Delta\mathcal{E}_g/2kT), \tag{4.2}$$

with the exponential factor increasing in importance as the applied voltage decreases.

In our computer calculations, Britsyn's experimental data has been used in modeling the bandgap reduction in terms of a lower effective doping density which is equivalent to the increase in minority carrier density resulting from the bandgap reduction. The results are shown as Figure 4.10. The detailed calculations are in fairly good agreements with the prediction

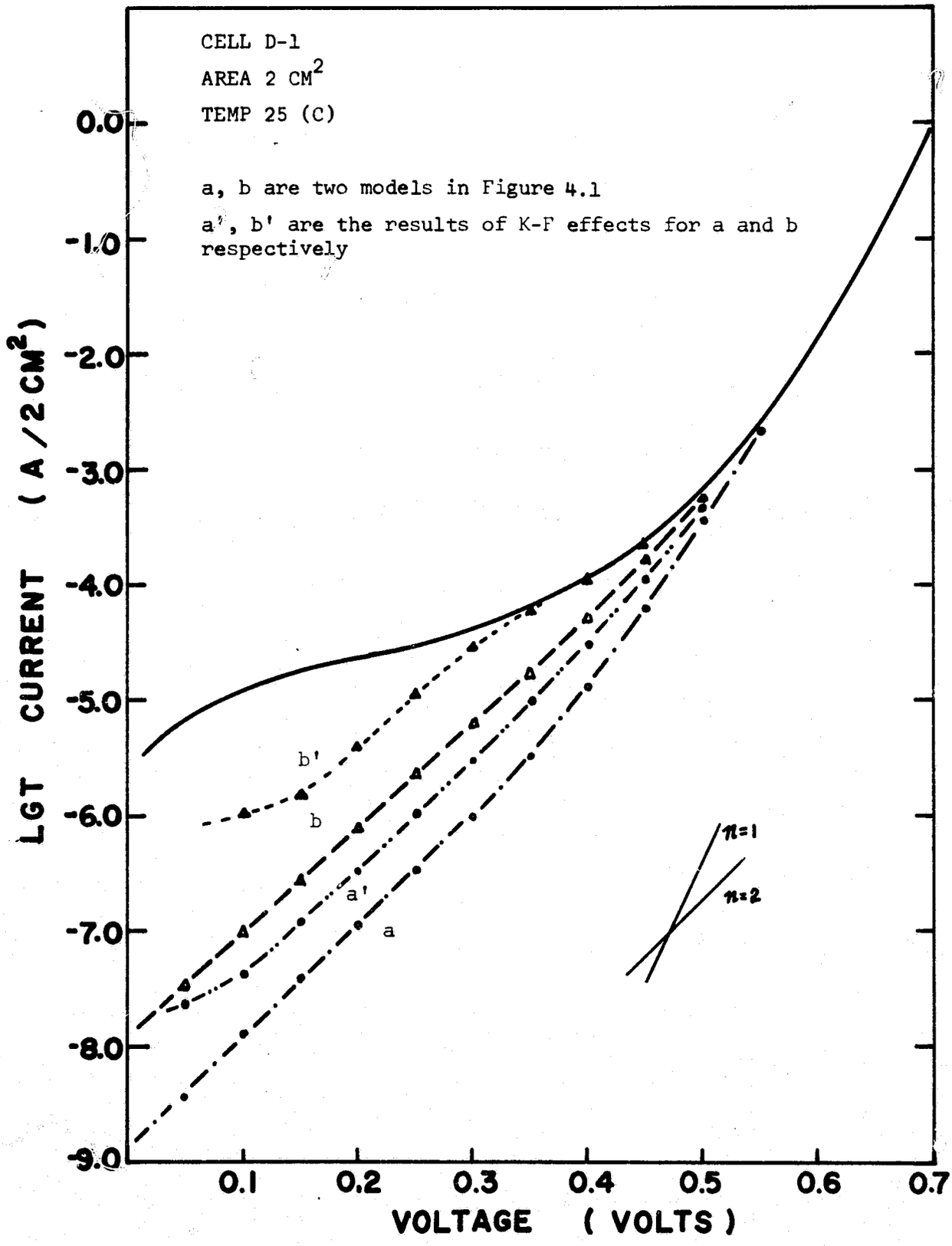

Figure 4.10. Excess current density at low voltage and Keldysh-Franz effects.

of the above simple equation, although it fails to explain the large excess current at low voltage. The predicted diode n factor is increased from that without Keldysh-Franz effect, but it is still less than 2 which is the maximum value from Sah's depletion recombination current model.

Since solar cells are quite large area devices, it is very difficult to completely eliminate surface imperfections such as dislocations, stacking faults and mechanical scratches. Hence there is a possibility of a shunting channel existing through these surface imperfections. The shunting channel could be characterized by some shunting resistance R_{ST}. The shunting effects are found to be more critical under the metal contact, especially for improper sintering treatments as has been experimentally confirmed by Stirn [13]. A model of a pure shunting resistance fits the data of devices D-1, D-2 and D-3 very well where 2.57 kΩ, 7.5 kΩ and 8.5 kΩ were found as values for the resistance (i.e. $R_{ST} \simeq 5.14$, 15, 17 kΩ/cm^2).

4.1.4 Design of High Efficiency Cells

Further improvements of solar cell operation can be achieved by reducing the forward dark current and enhancing the photon collection efficiency. Hence the base and surface lifetimes need to be preserved or increased to as large a value as possible. The optical dead layer at the surface need to be decreased and/or eliminated. This can be achieved by a reduction of the junction depth, using a different doping density and reducing surface recombination velocity. To indicate the improvements which might be made in cell D-1, calculations have been made with this basic cell but with modified parameters listed in Table 4.3.

Device D-1 is transformed into D-1-1 by adding a 5% antireflection film. This is also shown in Table 4.4 as cell D-1-1. Other changes give cells D-1-2 and D-1-3 of Table 4.3 with the improved results as seen in Table 4.4.

The SRV value of 10^3 cm/sec is about the lowest value which has been reported. It is also found to be the upper limit to any allowed value for essentially complete collection of short wavelength photons when the junction depth is 0.2 μm or less. The calculation of quantum response in Figure 4.11 shows that the collection efficiency is 94.7 percent at 0.4 μm for cell D-1-3 and this is very close to the upper limit of 95 percent set by the transmission coefficient. The surface doping density of $2 \times 10^{19}/cm^3$ is the optimum design for no retrogate field region induced by the heavy doping effect. A five percent surface reflectance is used because of the feasibility of making antireflection film of such low reflectance. It is clear from Table 4.4 that the most significant improvement obtained is by reducing the junction depth. This reduces the dead layer like effect and increases the collection efficiency.

The calculated data of Table 4.4 are the results of the one-dimensional calculation and shows a near ideal curve factor. In the two-dimensional model this value along with efficiency is decreased depending on the area of the blocking grid and the magnitude of the series resistance. The collection depth of the base region was calculated to be approximately 110 μm for D-1-3 giving a maximum available short circuit current of about 46.7 mA/cm^2 for AMO and a 5% antireflecting layer. This compares to the calculated short circuit current of 42.6 mA/cm^2 indicating that about nine percent of the available current density is lost by internal recombination.

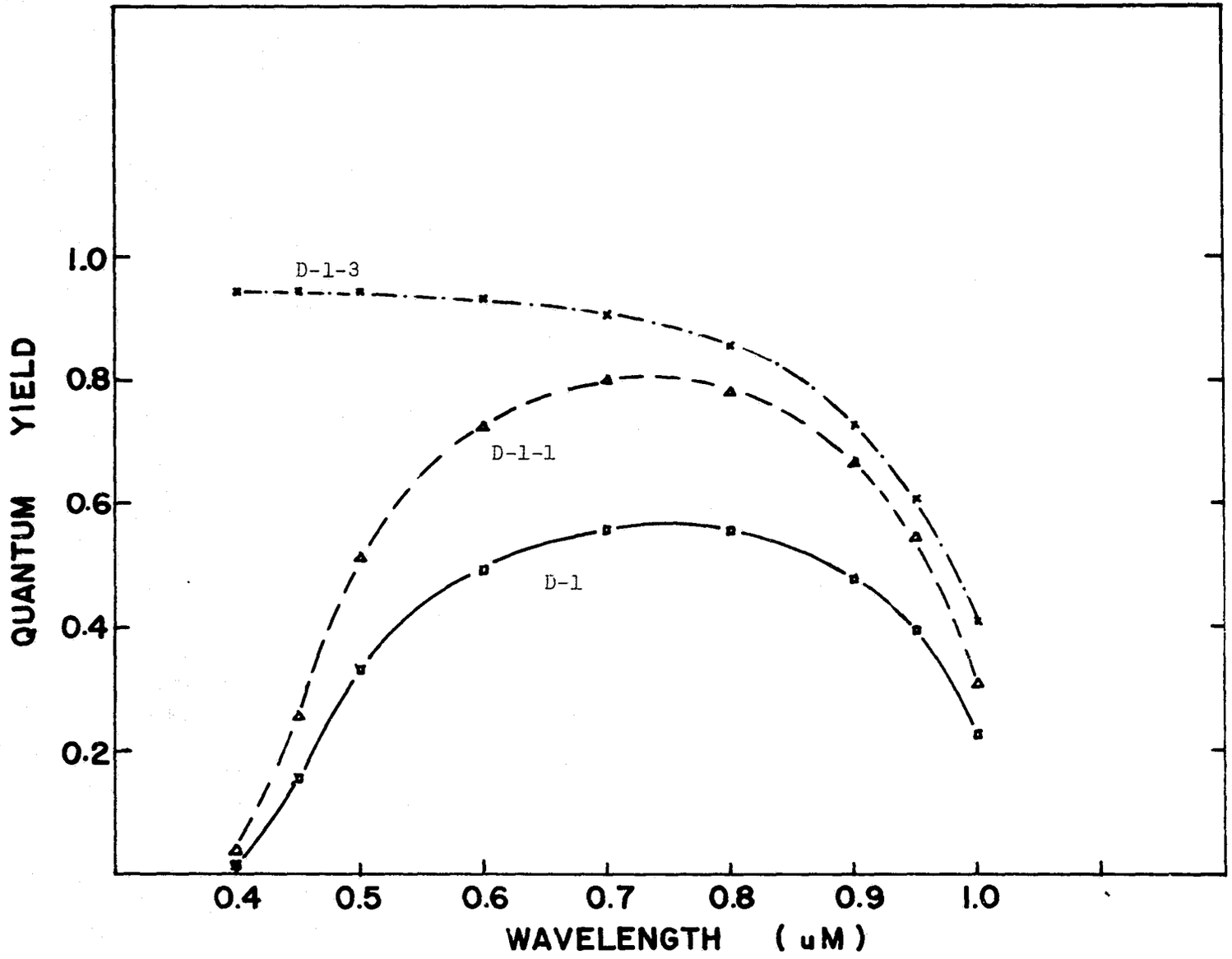

Figure 4.11. Comparison of the Quantum Yields for Devices of D-1, D-1-1 and D-1-3.

The higher efficiency for D-1-2 and D-1-3 over D-1-1 is mainly the result of the shallow junction which allows more of the generated carriers to be collected in the surface region.

4.2 Results of Type Two Cells

4.2.1 Simulation Model

These are standard cells from 10 Ω·cm ($1.25 \times 10^{15}/cm^3$) Boron doped wafers with a thickness of about 10.5 mils. The diffusion temperature was 850°C for half an hour and this produces a junction depth of about 0.57 μm. The surface doping profile was modeled after Tai's experimental results with the constants of C_S, C_B and X_C taken to be $2 \times 10^{20}/cm^3$, $2 \times 10^{19}/cm^3$ and 0.07 μm respectively. These values are in accordance with Figure 7 and Figure 11 of Reference [27]. A surface doping of $2 \times 10^{20}/cm^2$ was assumed which is consistent with the solid solubility of phosphorous at a temperature of 850°C [49]. Other important parameters used in the modeling are given in Table 4.5.

4.2.2 Comparison of Model and Experiments

The simulation procedure will be described briefly here. The long wavelength spectral response is dominated by the base region; hence, the base diffusion length can be found by matching the spectral response at long wavelengths. Also the surface diffusion length and surface recombination velocity can be found similarly from the best fitting of the spectral response at short wavelength. Finally forward dark I-V measurements and the short circuit current density provide a double check of the above parameters for consistency.

Figure 4.12 shows the spectral response and a comparison of the above model with the experimental results. Results for different surface models are also indicated on the graph where points a and b are models of erfc function with

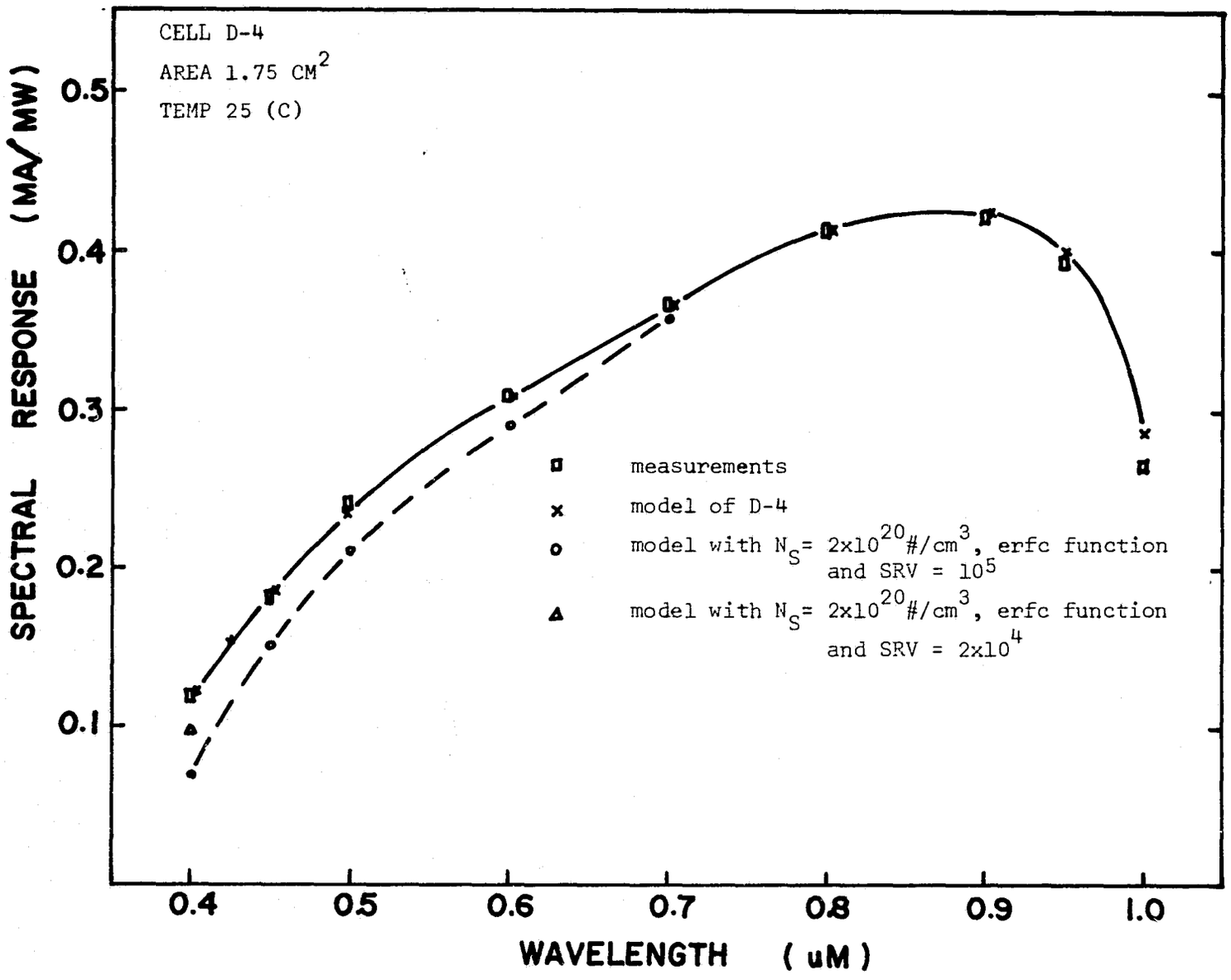

Figure 4.12. Comparison of the spectral response of Device D-4.

Table 4.5. Device model of type two cells.

	D-4	D-4-1	D-4-2	D-4-3	D-4-4
Structure	n^+p,10Ω·cm	n^+p, 10Ω·cm	n^+p,10Ω·cm	n^+pp^+,10Ω·cm	n^+pp^+,10Ω·cm
Junction Depth	0.57	0.57	0.2	0.2	0.2
Surface Doping	$2x10^{20}$	$2x10^{20}$	$2x10^{19}$	$2x10^{19}$	$2x10^{19}$
Surface Profile	Experimental	Experimental	erfc	erfc	erfc
Base Diff. Length	230	230	L_D(MAX)	L_D(MAX)	L_D(MAX)
Surface Diff. Length	1/2(L_D(MED)+(MIN))	1/2(L_D(MED)+(MIN))	L_{D_3}(MED)	L_{D_3}(MED)	L_{D_3}(MED)
SRV	$2x10^4$	$2x10^4$	10^3	10^3	10^3
Anti-reflection Layer	No	5%	5%	5%	5%
Device Thickness	265	265	250	250	250
Two way Reflection	Yes	Yes	Yes	Yes	Yes
Back Surface Layer	No	No	No	10^{19} Gaussian 0.5μm	10^{19} Gaussian 5 μm

Table 4.6. Calculated results of type two cells.

		D-4-1	D-4-2	D-4-3	D-4-4
VOC	(volts)	0.530	0.534	0.614	0.639
ISC	(mA/cm^2)	42.24	45.81	48.90	48.87
VM	(volts)	0.454	0.460	0.524	0.541
IM	(mA/cm^2)	39.39	43.17	46.17	45.86
PM	(mW)	17.88	19.86	24.19	24.81
CFF	-	0.799	0.812	0.806	0.714
EFF	(%)	13.22	14.68	17.88	18.34

$2x10^{20}/cm^3$ surface doping density and surface recombination velocities of 10^5 and $2x10^4$ cm/sec respectively.

Dark I-V characteristics are shown as Figure 4.13. In general there is a good matching over the higher voltage range. High injection effects are clearly shown as the higher slope n factor at voltage larger than 0.6 volts. this is very close to the 1st order prediction of a 0.575 volt transition from low to high injection from the equation $V^*_{HL} = 2\frac{kT}{q}\ell n(N_A/n_i)$ [11]. At one sun AMO power density, this high injection effect can be usually neglected. However, for multi-sun operation, high injection effects become very important for 10 Ω·cm base layer cells.

The dominance of the base region can be seen from the results of Table 4.7 which shows the relative recombination rate for different regions of the cell. About 90% or more of the recombination occurs in the base layer. The excess current at low voltages is clearly seen in Figure 4.13.

The results of the two-dimensional analysis agrees very well with the measured sheet resistance values. A value of 1500 Ω was estimated for this device in agreement with the first order estimation from Equation 2.7. Finally the comparison of theoretical and experimental light I-V characteristics are shown in Figure 4.14. The general agreement between the model and experiments is quite good.

The two-dimensional analysis gives good agreement between theory and experiment for sheet and contact resistance values of 1500 Ω/□ and 1.12 Ω respectively. A comparison of the results are given in Table 4.8. The curve factor of the 1-dimensional analysis is much higher than the value experimentally obtained. Also from the comparison of the 1-dimensional and 2-dimensional analysis, it is clear that the effect of high series resistance is mainly in the reduction of the curve factor. This point is discussed in more detail in the chapter on series resistance.

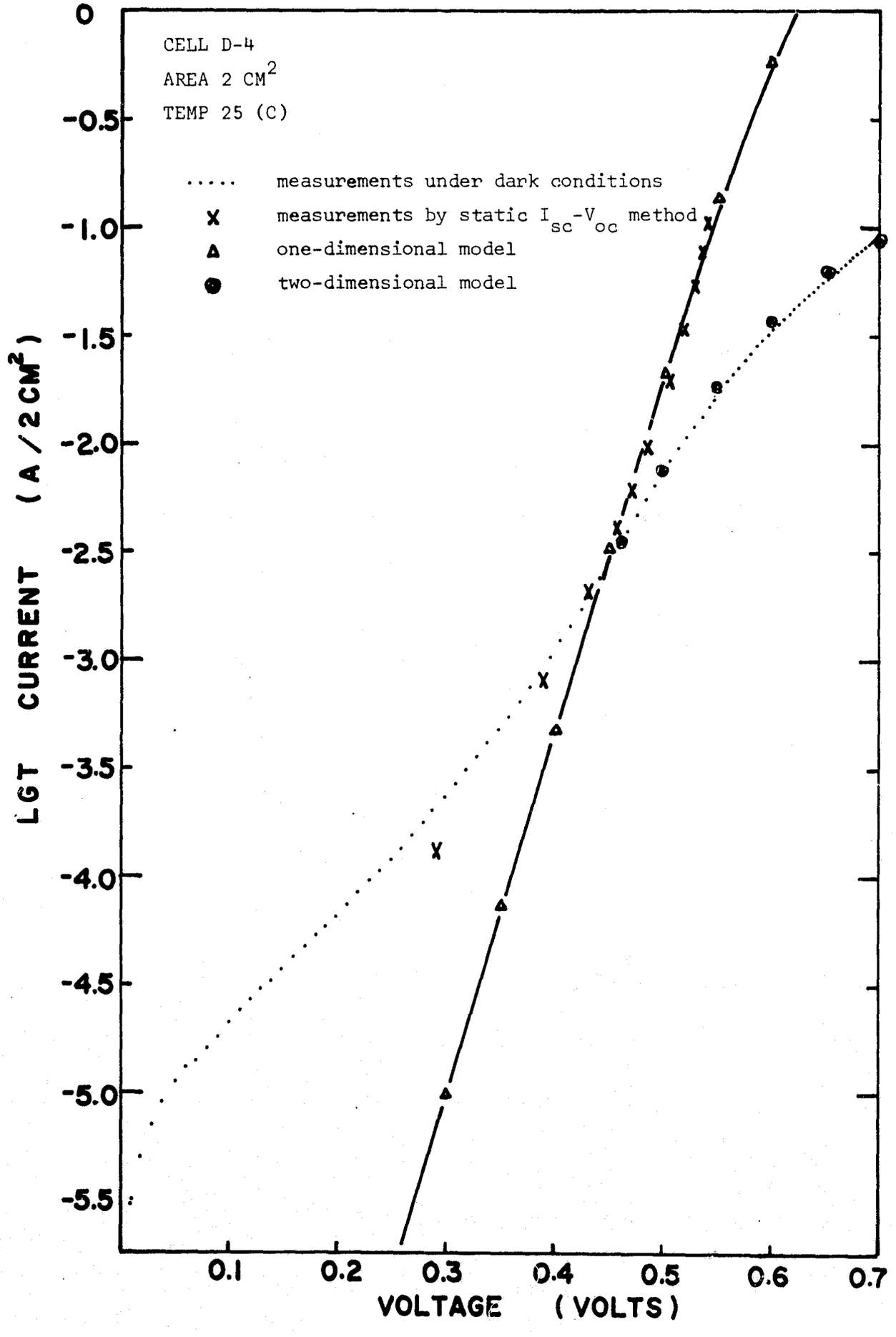

Figure 4.13. Comparison of the dark I-V characteristics of Cell D-4.

Table 4.7. Fraction of dark current density at different region of device D-2.

	VOLTAGE (VOLTS)				
%R	0.3	0.4	0.5	0.6	0.7
Surface	0.5	0.5	0.5	0.9	3.8
Depletion	10.9	3.2	1.5	0.8	1.0
Base	88.6	96.3	98.0	98.3	95.2

Table 4.8. Results of one and two dimensional calculations of D-2.

	I_{SC_2} (A/2 ^{2})	V_{OC} (volts)	I_{M_2} (A/2cm^2)	V_m (volts)	P_m (mW)	CFF	EFF (%)
1-DIM	0.05866	0.527	0.05371	0.464	24.92	0.806	9.21
2-DIM	0.0501	0.522	0.0399	0.331	13.21	0.505	4.88

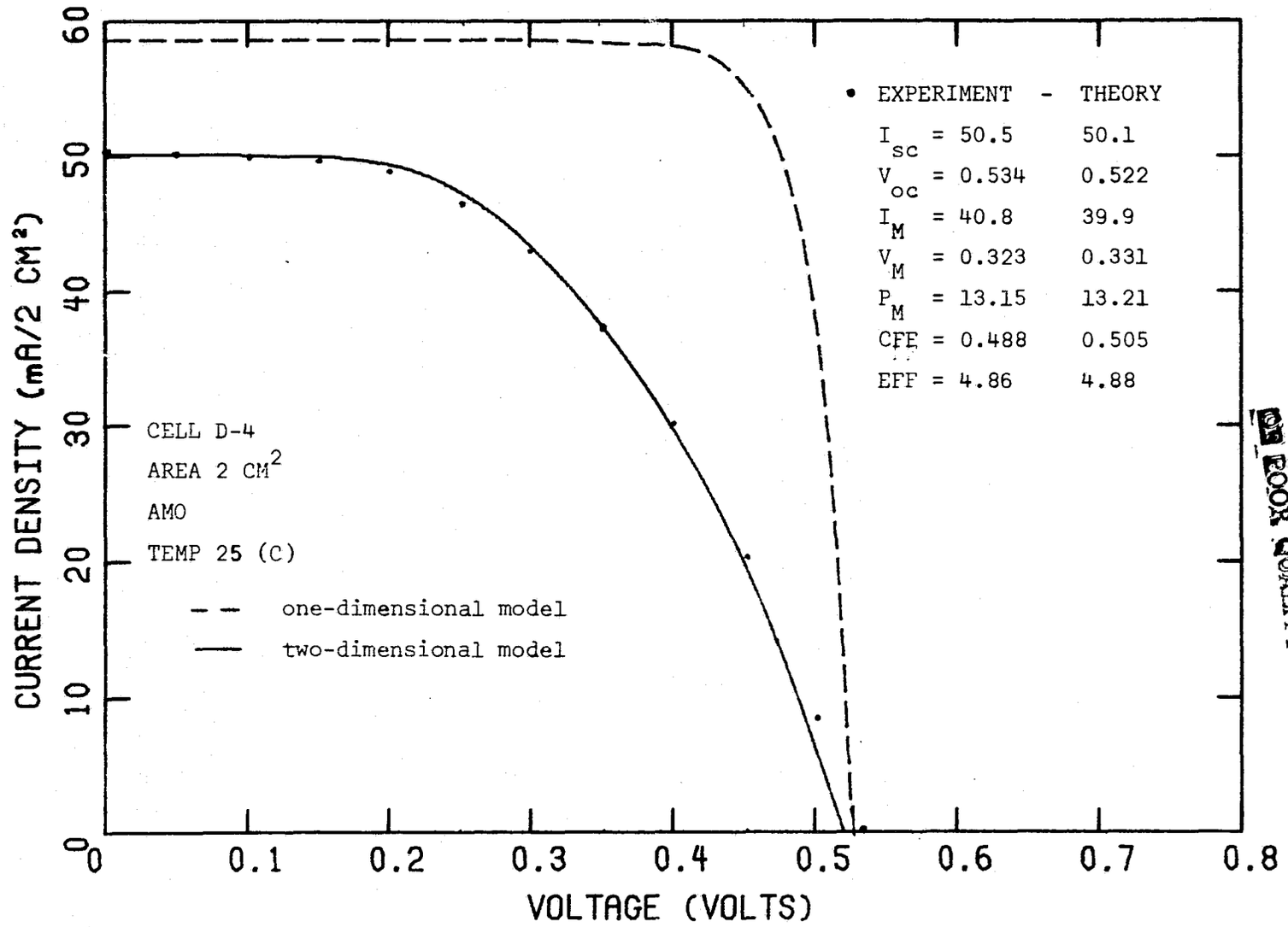

Figure 4.14. Comparison of the photovoltaic I-V characteristics of Cell D-4.

4.2.3 Design of High Efficiency Standard Cells

The prospects of increasing the conversion efficiency of a standard n^+p silicon solar cell appear promising from the results of Table 4.5 and Table 4.6. Devices D-4-1, D-4-2, D-4-3 and D-4-4 are calculated variations of the 10 Ω·cm cell which show improved performance. The parameters used in the improved performance calculations are not unreasonable.

It is interesting to compare the quantum yield of devices D-4-2 and D-4-3 with device number D-4-1 which is similar to device D-4 except for the use of a 5% AR film instead of the bare silicon surface in the calculations. It is clear in Figure 4.15, that a higher quantum yield can be achieved through the proper designs of the cell structure and parameters. The much better response at long wavelength for BSF cells is also shown in the same figure. This results from the lower effective surface recombination velocity at the high-low junction. The superiority of BSF cells over non-BSF cells arise mainly from increasing V_{oc} and to a lesser extent from an improved collection efficiency.

The curve factor is usually observed to be better for BSF cells than for non-BSF cells. In the present case the curve factor is less than the non-BSF counterpart cell because of high injection occurring for this specific design of BSF cell. The calculation of diode n-factor for D-4-3 and D-4-4 results in a value of 1.15 and 1.20 respectively in the range of 0.6 volts to 0.65 volts. Also the minority carrier density was found to be larger than the base doping density in the above voltage range. In a practical solar cell, the actual diffusion length of minority carriers may be less than the model presented above and high injection may not occur. This may explain the difference in V_{oc} for the predictions and for experimental solar cells.

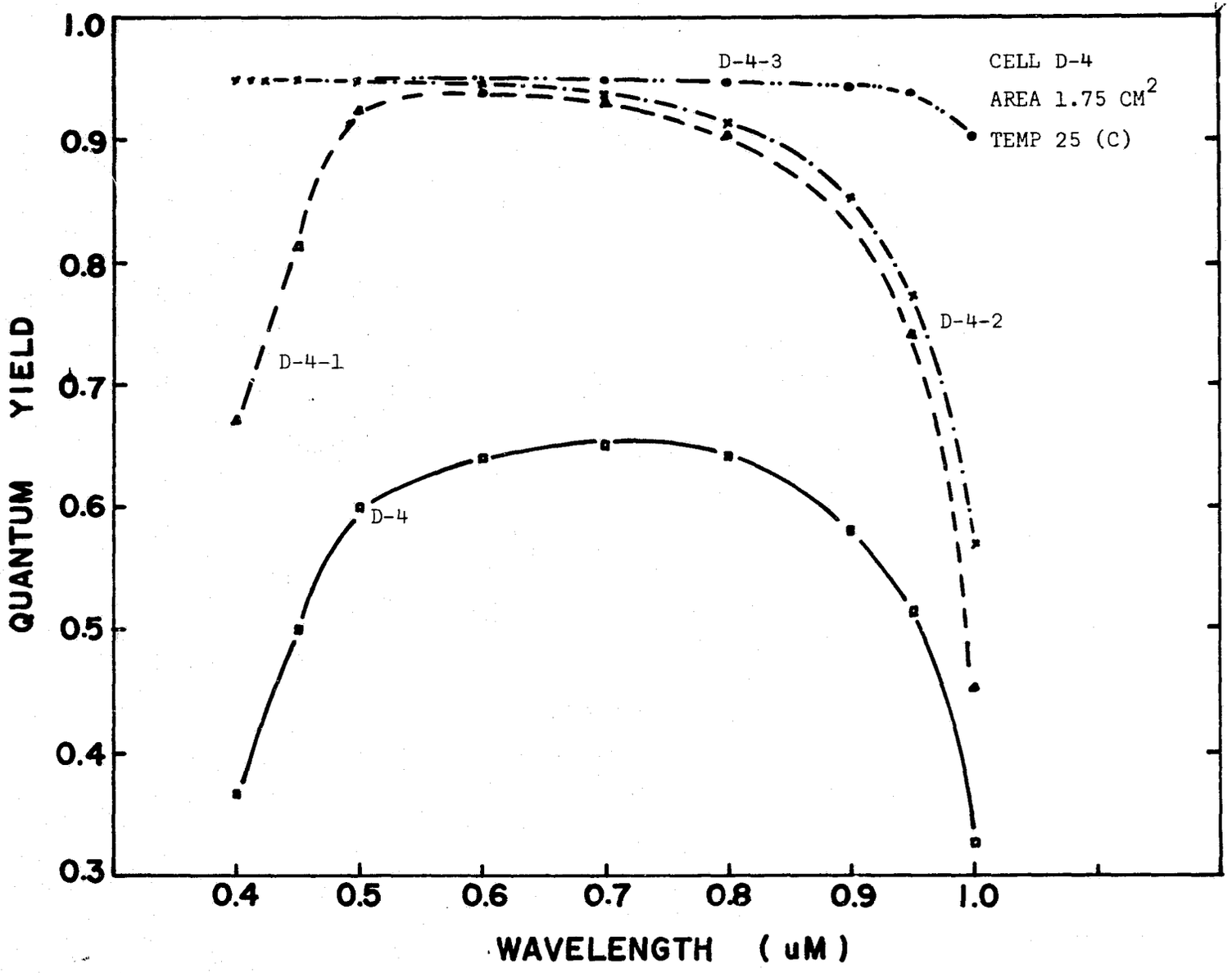

Figure 4.15. Comparison of the spectral response of type two cells D-4, D-4-1, D-4-2 and D-4-3.

The fabrication of devices with back surface field regions of 5 μm in thickness may be difficult by normal alloy processes which usually make high-low junction less than 1 μm in thickness. However, the epitaxial growth technique can grow layers up to 25 μm relatively easily [Ref. 50]. Our calculations indicate that such thicknesses (5 μm) are required for high efficiency solar cells.

4.3 Type Three Cells

4.3.1 Simulation model

These cells are Aluminum BSF cells made using 16 Ω·cm ($9x10^{14}/cm^3$) Boron doped wafers with finished thickness of about 6.5 mils. The diffusion is performed at low temperatures resulting in a junction depth of about 0.2 μm. The surface doping density was assumed to be $2x10^{20}/cm^3$, with a profile described by a complementary error function. The base diffusion length was measured to be 160 μm at the NASA Lewis Research Center.

The back surface field was made by alloying a layer of Aluminum. This bottom p^+ profile was assumed to be a Gaussian function with a junction depth of about 0.5 μm and a surface doping density of $1x10^{19}/cm^3$. The values assumed above are consistent with the published experimental diffusion coefficient and solid solubility of Aluminum at the particular temperature of 800°C [49].

The anti-reflection layer of Ta_2O_5 was matched to the wavelength of 0.5 μm resulting in a thickness of 595 Å. The value of 2.20 was assumed as the reflective index although the true value may vary between 2.20 and 2.30. The outside cover of 5 mils "Teflon" FEP has a refractive index varying between 1.341 to 1.347.

4.3.2 Comparison of Model and Experiments

Before presenting the results, an interesting and perplexing fact of the BSF cells should be described. For the non-BSF cells the diffusion length measured at NASA Lewis was found to be close to the value giving a best theoretical fit to the experimental data. This is not the case for the BSF cell. The use of the measured diffusion length was found to give a dark current much larger than experimentally measured as seen by the upper curve in Figure 4.16. A diffusion length of 460 μm was found to give a good fit to the dark current data as also shown in Figure 4.16. This value is also consistent with the spectral response data as shown in Figure 4.17. The reasons for this discrepancy are not completely known although it is known that the usual method of measurement of diffusion length that relies on the semi-infinite cell width and bottom ohmic contact cannot be used in a straightforward manner to deduce the diffusion length in the presence of a HL junction [50]. Agreement between theory and experiment can only be obtained if the diffusion length is considerably larger than the NASA Lewis measurements.

The two-dimensional analysis of the dark I-V characteristics using the 9-finger Spectro Lab grid pattern agrees with the measured results. Also the two-dimensional light I-V characteristics of Figure 4.18 are fairly well matched to the experimental data further justified the parameters summarized in Table 4.9. (More details of the BSF cell are discussed in another chapter.)

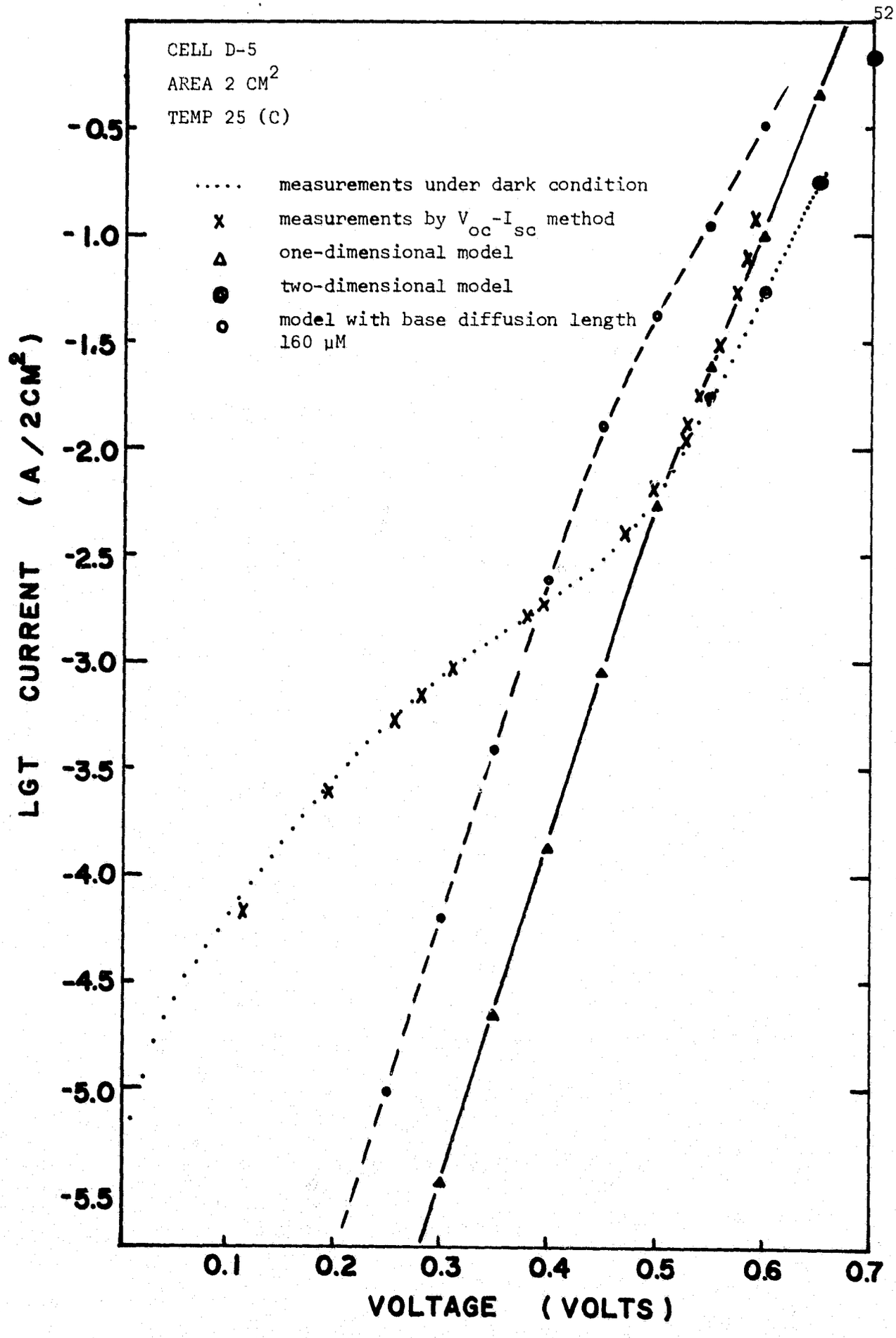

Figure 4.16. Comparison of the dark I-V characteristics of Cell D-5.

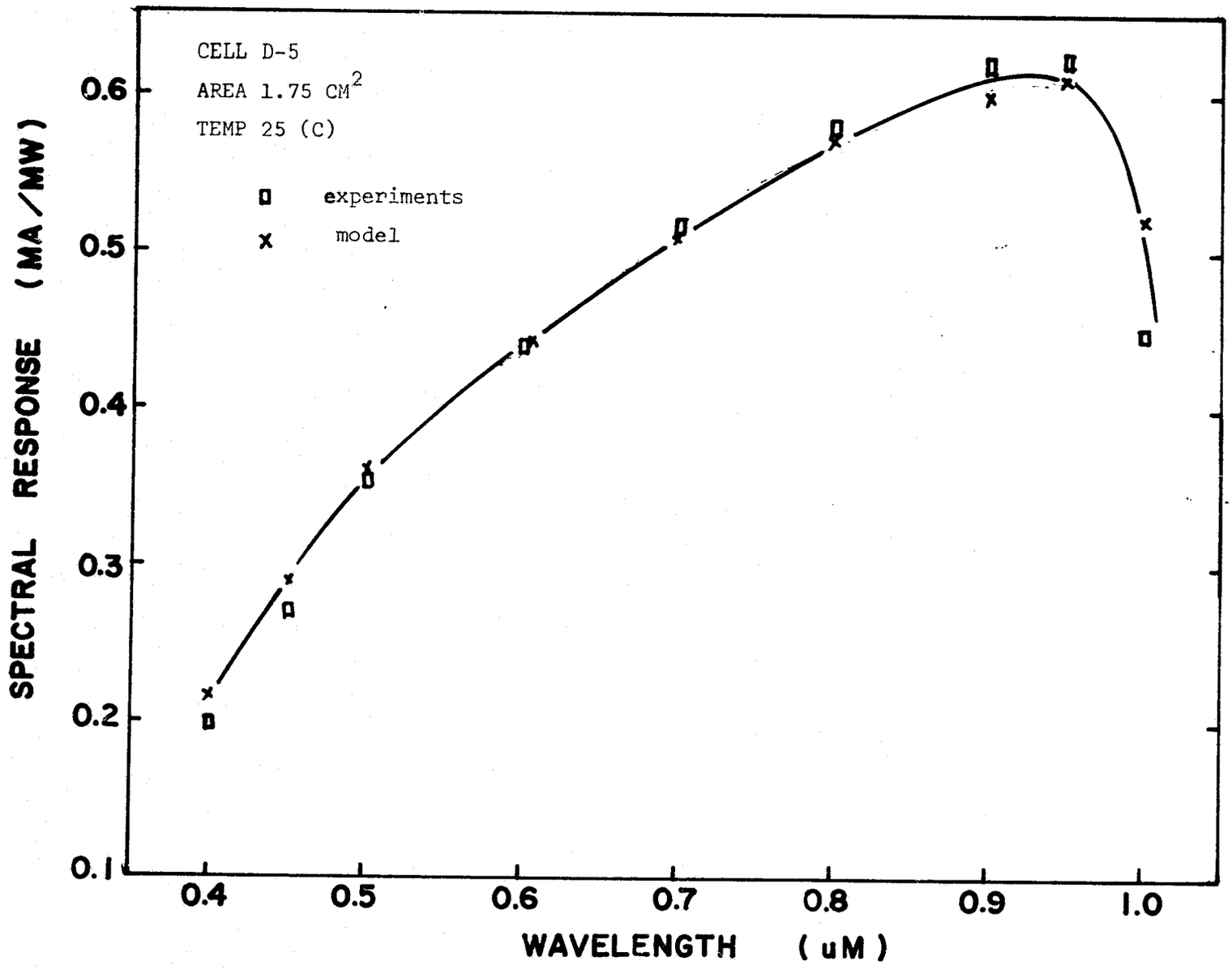

Figure 4.17. Comparison of the spectral response of Cell D-5.

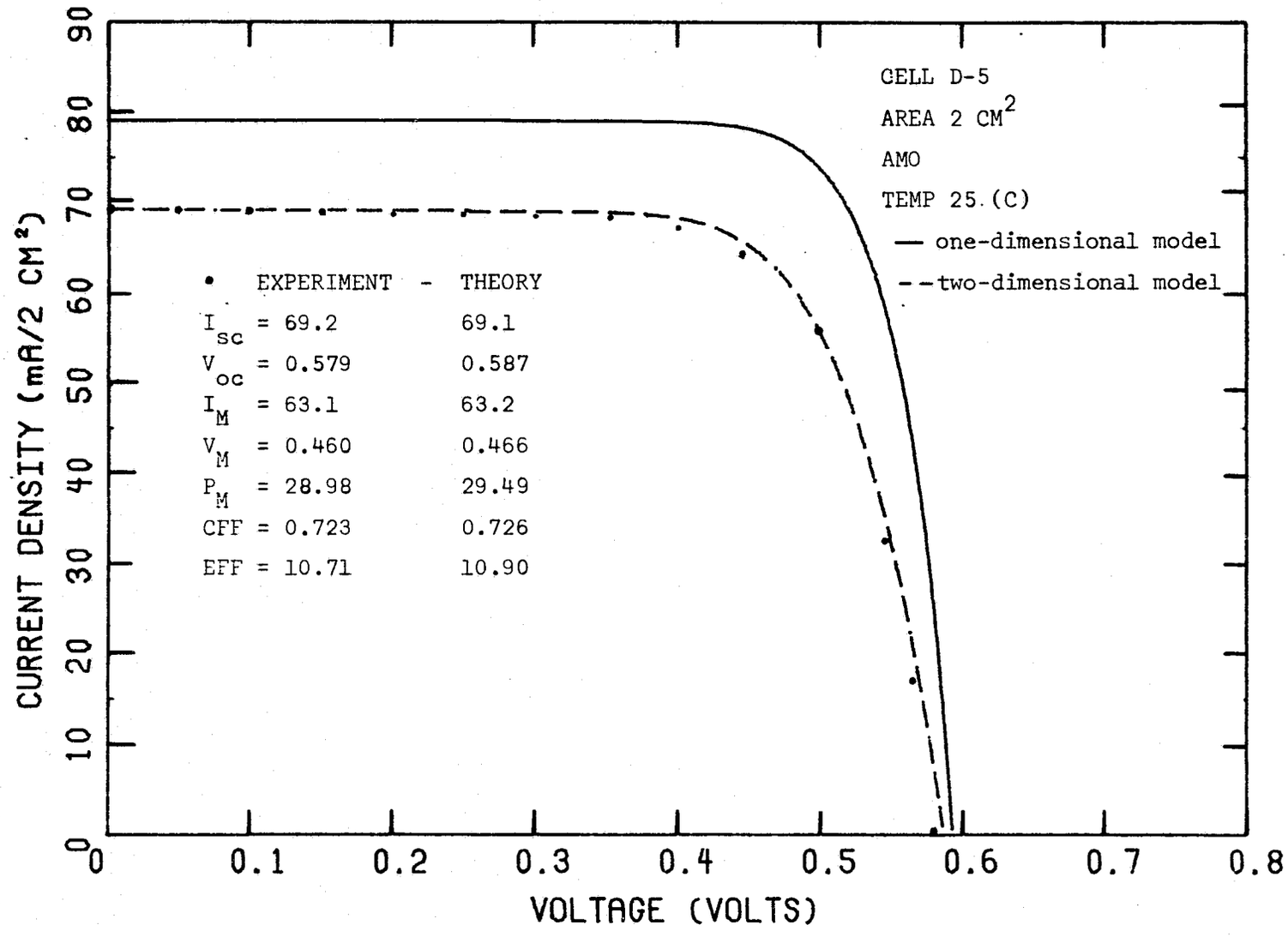

Figure 4.18. Comparison of the photovoltaic I-V characteristics.

Table 4.9. Device model of type three cells.

Parameter	D-5
Structure	n^+pp^+ on 16 Ω•cm wafer
Junction Depth	0.2 μM
Surface Doping	$2x10^{20}$
Surface Profile	erfc
Base Diff. Lengths	460.
Surface Diffusion Length	$L_D(MED)+L_D(MIN)$ / 2
SRV	$5x10^3$
Antireflection Layer	Ta_2O_5 595 Å + 5 mil Teflon FEP
Device Thickness	160 μM
Back Surface Reflection	Yes

The results of one-dimensional and two-dimensional analysis are shown in Table 4.10. In the two-dimensional analysis, the sheet resistance was found to be 380 Ω/□ with a negligible contact resistance or at least a value smaller than 10^{-4}Ω. It is clear that the slope of the measured dark I-V characteristics has a diode n-factor of near two at high voltage which is characteristic of pure sheet resistance as Equation 2.6 shows.

The calculated results above were made neglecting the excess current density for voltage below 0.45 volts. The comparison of the measured and calculated two-dimensional model shows the effect of excess current density at low voltage and these are shown in Table 4.11.

Under the small contact area, there exists only the forward dark current density. Thus the difference in photovoltaic measurements fairly close to the excess dark current implies that the excess current is a localized parameter instead of a distributed p-n junction effect. Also the near equality in both excess current density at the specific voltage suggests that the localized leakage channel exists under the metal contact. D-5 has very low contact resistance, hence the voltage under the metal contact is very close to the terminal voltage. The voltage profile between two fingers is given in Table 4.12 at the terminal voltage of

0.45 volts assuming 10 equal spacing points where points 1 and 10 are under the metal contact. This is an indirect verification of the localized shunting channel under the metal contact area which has been detected directly by Stirn [13].

Table 4.10. Calculated results of one and two dimensional model of D-5.

	I_{SC} ($A/2cm^2$)	V_{OC} (volts)	I_m ($A/2cm^2$)	V_m (volts)	P_m (mW)	CFF	EFF %
1-DIM	0.0791	0.594	0.0742	0.498	36.96	0.786	13.66
2-DIM	0.0691	0.587	0.0632	0.466	29.49	0.726	10.90

Table 4.11. Comparison of the leakage current density of the photovoltaic I-V characteristics.

Voltage	($mA/2cm^2$) Photovoltaic I-V Experimental	($mA/2cm^2$) Photovoltaic I-V Model	($mA/2cm^2$) Difference in Current $mA/2cm^2$	($mA/2cm^2$) Excess current density from dark I-V measurement
0.25	68.50	69.13	0.63	0.51
0.3	68.10	69.09	0.99	0.83
0.35	67.70	68.96	1.26	1.23
0.4	66.25	68.33	2.08	1.91
0.5	62.30	65.33	3.03	2.98

Table 4.12. Photovoltaic potential profile of device D-5 at the terminal voltage of 0.45 volts.

	1	2	3	4	5	6	7
V (Volts)	0.4503	0.4741	0.4917	0.5034	0.5092	0.5092	0.5034
	8	9	10				
	0.4917	0.4741	0.4503				

5. SERIES RESISTANCE EFFECTS ON Si SOLAR CELLS

5.1 Introduction

Series resistance in a silicon solar cell is a detrimental power consuming parameter which can seriously reduce the power conversion efficiency. Surface sheet resistance, bulk resistance, and surface and back metal contact resistances are the major contributions to the internal effective series resistance. Due to the small metal coverage on the surface, the current flows basically transverse to the collecting junction and is nonuniformly distributed on the surface. Hence the effective series resistance depends on the grid contact geometry and is a distributed parameter in general.

With the trends of making very shallow junction cells, the sheet resistance becomes a limiting factor for power conversion. Also there is increased interest in operating in a multi-sun environment for terrestrial applications. In this case, sheet, bulk and contact resistance are critical in efficient power conversion.

Although it has been recognized for many years that a distributed resistance model is the only proper representation of a solar cell [51], many authors have worked mainly on lumped-resistance, 1st-order models [51,52]. The objective of this chapter is to analyse the series resistance effects on silicon solar cell performance using a distributed resistance and current model. A one-dimensional model accounts for the bulk resistivity while the sheet resistance and the contact resistance are modeled by a two-dimensional distributed resistance model. Since normal solar cells are made with metal coverage all over the back surface, the base layer resistance and back contact resistance can be treated as

non-distributive. The details of this model are discussed in the appendix on the two-dimensional analysis of solar cells. The model is justified by comparisons to experimental measurements.

5.2 Series Resistance Effects on the Current-Voltage Characteristics of Solar Cells

There are basically three ways of obtaining the current-voltage characteristics of solar cells (Figure 5.1). First the dark forward I-V characteristic can be measured by applying a terminal voltage without any light illumination. According to first order device models the output current can be represented by the equation

$$I = I_o\{\exp[q(V-IR_s)/nkT] - 1\}, \tag{5.1}$$

where n ranges from about 1.0 to about 2.0.

The second method uses a varying illuminating intensity and measures open circuit voltage and short circuit current. A plot of the corresponding points then gives a current-voltage equation which according to first order models is described by

$$I = I_o\,[\exp(qV/nkT) - 1] \tag{5.2}$$

This method has been used independently by Heeger [53], Wolf [51] and Queisser [44]. The advantage of this method is that the effects of series resistance are effectively eliminated as seen in Equation 5.2.

The 3rd method uses a constant illuminating intensity but with a variable external resistance load. This photovoltaic method is the most important measurement for solar cell performance. Since the important parameters of short circuit current density, open circuit voltage, curve factor and efficiency can only be obtained by this method. According to first order models this gives an equation of the form

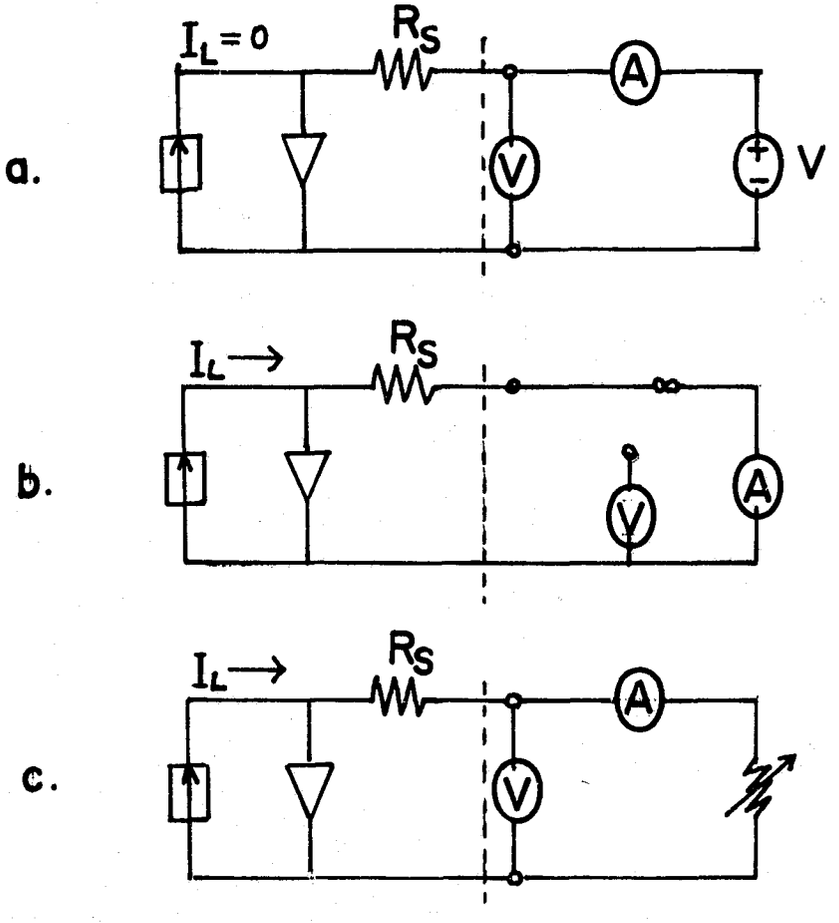

Figure 5.1. Measurements of current voltage characteristics of solar cells.

(a) measurements of dark I-V characteristics
(b) measurements of static I_{sc}-V_{oc} characteristics
(c) measurements of photovoltaic I-V characteristics

$$I = I_o \{\exp[q(V-IR_s)/nkT] - 1\} - I_L, \qquad (5.3)$$

where I_L is the short circuit current.

For illustrative purpose, consider a two centimeter square Si cell with a base resistivity of 0.1 Ω•cm and a standard NASA ten fingers grid pattern. Although the metal mask was designed with 1.91 cm^2 active area, the active area from actual measurements is between 1.80 cm^2 and 1.70 cm^2 because of metal spreading during the evaporation process. An average value of 1.75 cm^2 of active area is used in this work. The dark I-V characteristics are taken from the experimental result of device D-2, which has a very low sheet resistance and contact resistance. Figure 5.2 shows the effect of various sheet and contact resistances on the dark I-V characteristics where a value of 500 Ω/□ has been assumed for the sheet resistance. This corresponds to the resistance of a shallow junction depth of about 1500 Å [41].

5.2.1 Effects of R_s on Dark I-V Measurements

As a result of the transverse current flow the actual junction voltage is reduced away from the contact fingers. This implies a lower forward current density at any given terminal voltage. This is clear from Figure 5.2 where it is seen that the sheet resistance effectively lowers the current level at any given voltage. The contact resistance has a similar effect at high current densities.

Only curve (b) in Figure 5.2 can be truly modeled by a lumped effective series resistance of 0.4 Ω. The series resistance of curve (c) and (d) are a nonlinear function of the current level. This is shown in Table 5.1. The photovoltaic column refers to the terminal I-V measurements under

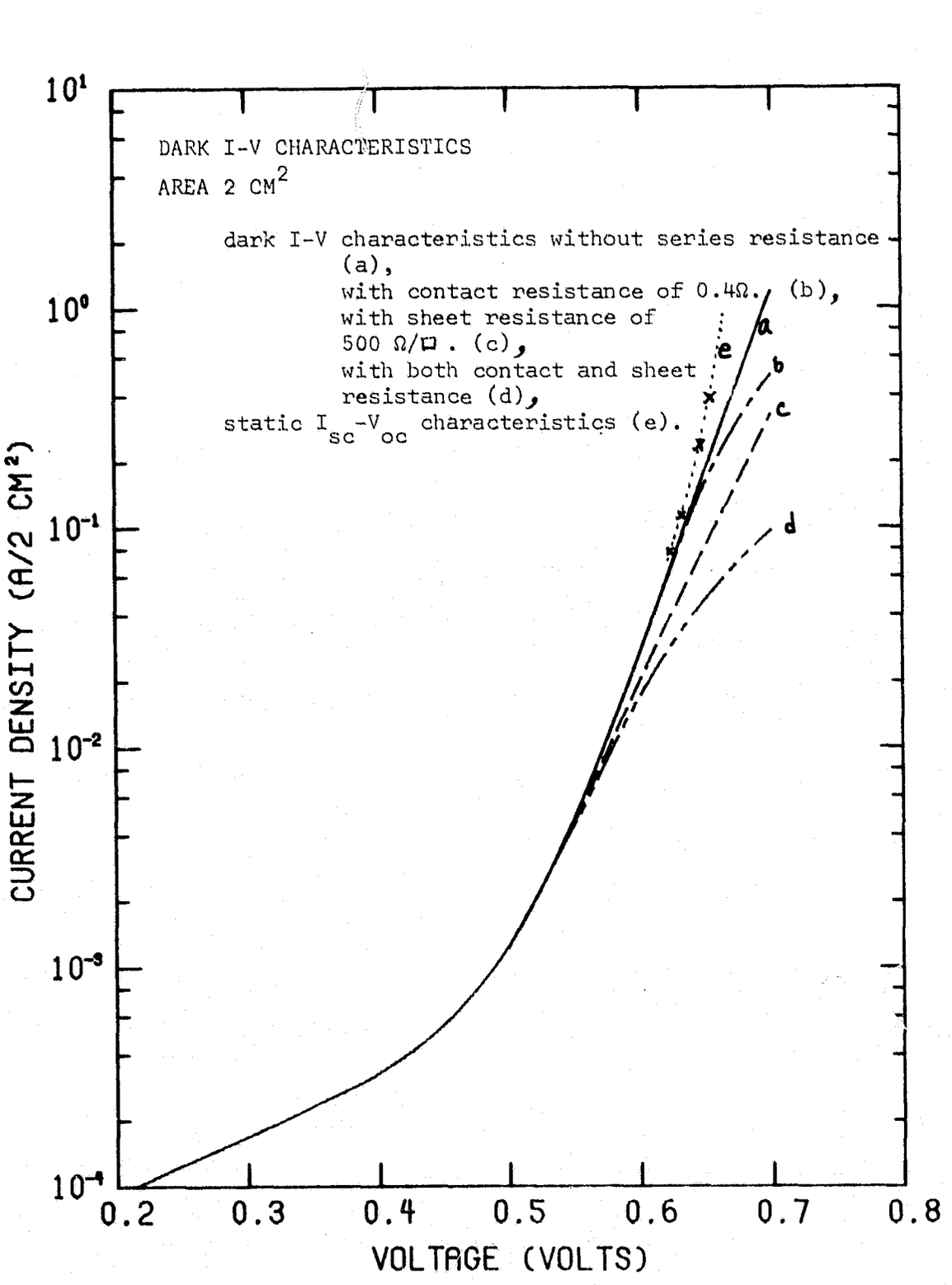

Figure 5.2. Effects of series resistance on dark I-V characteristics.

constant illumination while the dark column refers to standard terminal I-V measurements. As the table values show the "resistance" needed in Equation 5.2 or 5.3 depends upon the measurement method as well as the current level. Figure 5.3 shows a typical variation of photovoltaic potential between two finger contacts. Figure 5.4 shows calculated potential profiles on the surface of a cell and is the true representation of the potential difference across the p-n junction at various points along MM' of Figure 5.3. The potential drop across the contact resistance are indicated as the voltage difference at each terminal potential. The total contact resistance can be calculated as the sum of the surface finger contact resistance and back contact resistance as

$$\text{Total contact resistance} = \frac{\text{surface contact resistance in } \Omega\cdot\text{cm}^2}{\text{surface contact area}} + \frac{\text{back contact resistance in } \Omega\cdot\text{cm}^2}{\text{back contact area}} . \quad (5.4)$$

Because of the much larger area of the back contact, most of the contact resistance probably arises from the front surface metal fingers. This will be assumed to be the case in further discussions, although the results do not depend on exactly where the contact resistance occurs.

5.2.2 Effects of R_s on Static I_{sc}-V_{oc} Measurements

The second method of static I_{sc}-V_{oc} measurement has been suggested as a way to correct for the series resistance effect and to observe the ideal one-dimensional I-V characteristic as Equation 5.2 shows [51]. Unfortunately there is always a finite contact area and series resistance such that the static I_{sc}-V_{oc} characteristic is not always identical with the ideal dark I-V characteristic. There may be a rather large deviation for higher light illumination such as curve (e) of Figure 5.2.

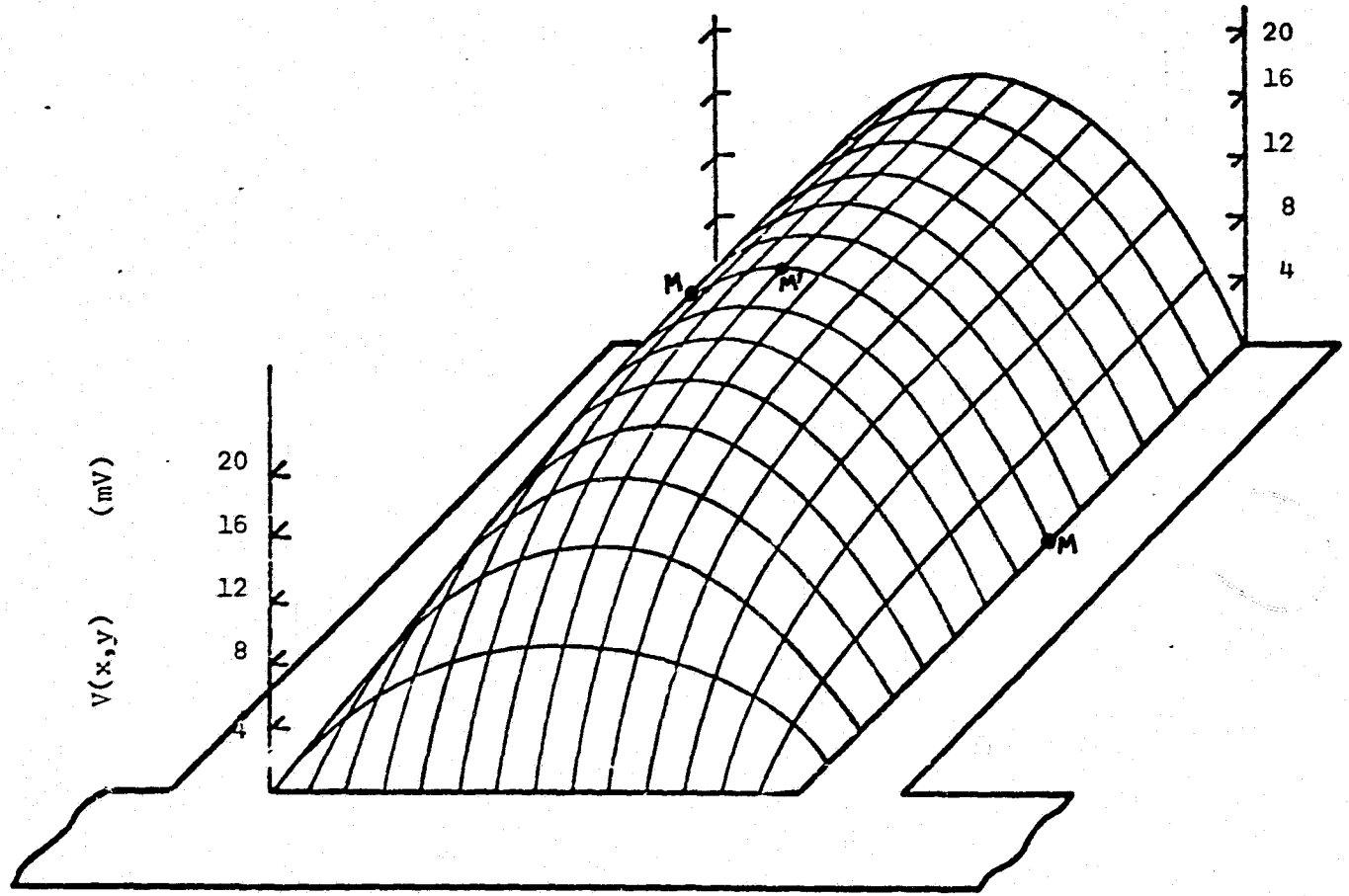

Figure 5.3. Typical variation of potential between contact fingers for a 1 cm by 2 cm solar cell with 10 contact fingers.

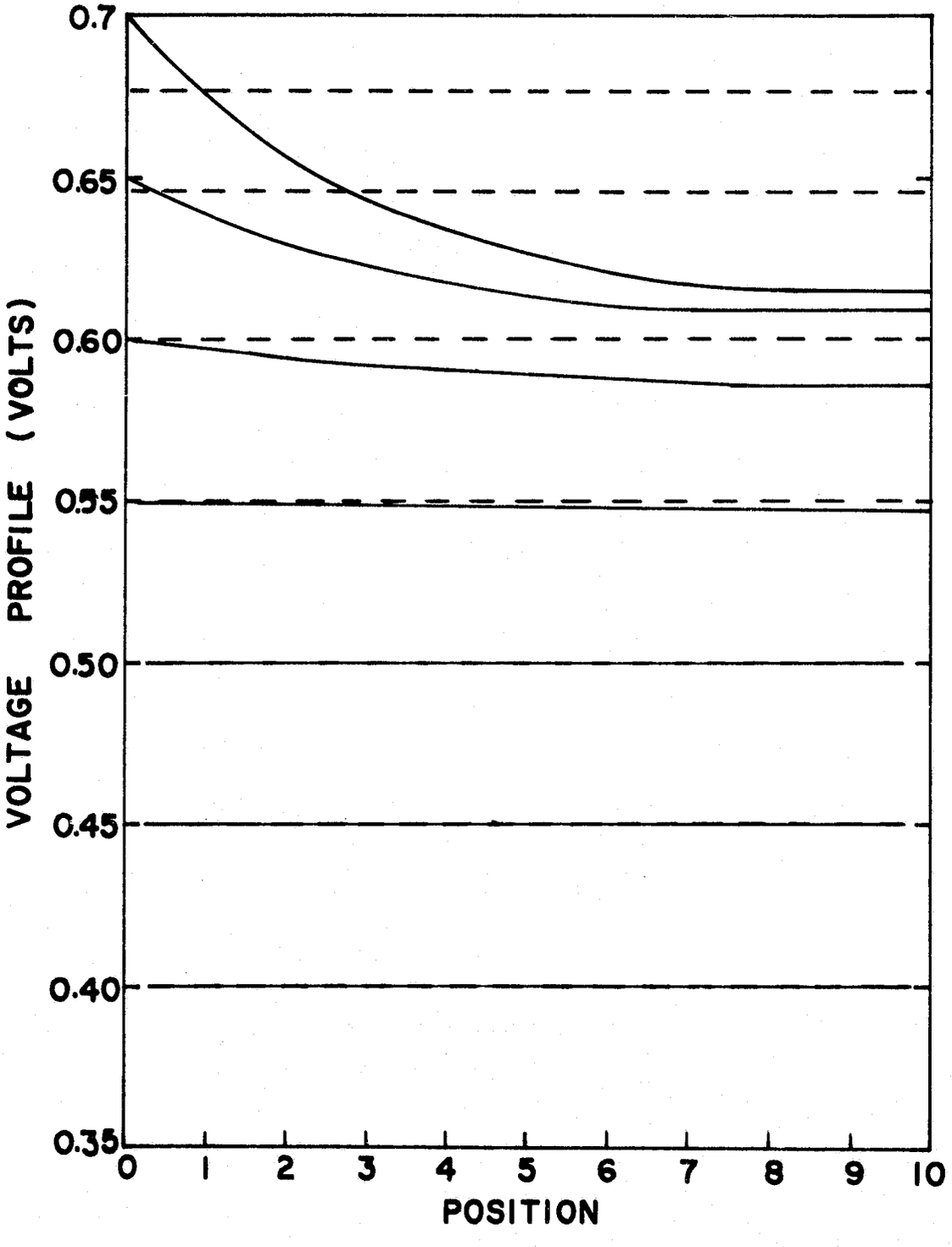

Figure 5.4. Surface potential profile without illumination. R_{ST} = 500 Ω/□ and R_C = 10^{-7} Ω-CM^2 (solid line), R_{ST} = 10 Ω/□ and R_C = 0.1 Ω-CM^2 (dashed line).

Because the illuminated area differs from the total junction area there is always a slight offset in the light I-V data from the ideal junction behavior. This can be evaluated as

$$\Delta V_{oc} = n \frac{kT}{q} \ell n(A/AA) \simeq 4 \text{ mV}, \qquad (5.5)$$

where AA is the active area out of total area A and n is the diode ideality factor at the open circuit voltage. When sheet resistance is present the difference can be even larger at high illumination levels. At the open circuit condition, there is no external current density which means that the forward dark current density exactly balances the photon-induced current density. There is a finite dark current which flows under the metal contact area and this current can only be supplied by a current flow transversely to the surface. Thus the terminal open circuit voltage is reduced until a balance between both current densities is established. Unlike the first order model of Equation 5.5 which predicts a constant shift in open circuit voltage, the distributed diode model predicts a much higher shifting in open circuit voltage at higher illumination.

The amount of the reduced open circuit voltage cannot be easily estimated with the first order model, but the general trend is toward a larger reduction with higher values of current level, sheet resistance and ratio of dark contact to the illuminated area. Figure 5.5 shows calculated photovoltaic potential at two different light intensities and at open circuit conditions along path MM' of Figure 5.3. The terminal open circuit voltage is seen to be as much as 5-15 mV below the voltage away from the contacts.

Similarly at short circuit conditions, the measured short circuit current is reduced by the amount of the forward dark current density

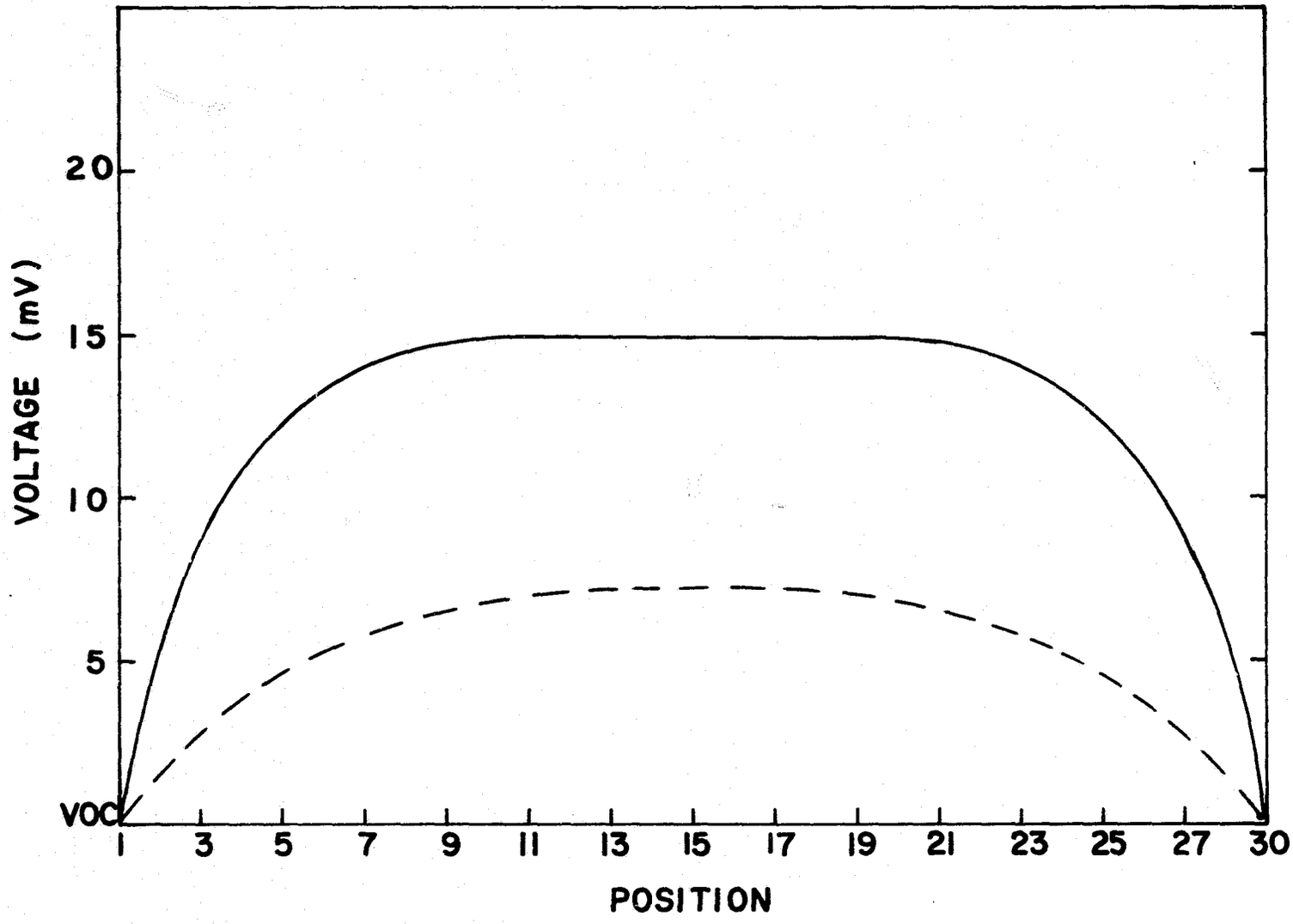

Figure 5.5. Photovoltaic potential at open circuit for one sun and 5 sun input power intensity with R_{ST} and R_C to be 500 Ω/□ and 10^{-7} Ω-cm^2. One AMO (dashed line), five AMO (solid line).

in the active area where the p-n junction potential exceeds the short circuit voltage. Figure 5.6 shows the potential drop in the cell under short circuit conditions. At 5 suns part of the cell operates at a 20 mV forward bias, and the forward current at these voltages subtracts from the terminal short circuit current.

The reduction in open circuit voltage is much more than the corresponding reduction in short circuit current. Thus the measured light I-V characteristic has a much lower diode n-factor and this factor is generally less than or equal to 1 with smaller values occurring for higher illuminating intensities. These effects cause the light I-V data not to be very useful at high illumination levels.

One interesting result needs to be discussed. The reduction of V_{oc} under the illuminating condition due to high sheet resistance has been discussed above; however, it is found that the surface contact resistance can compensate for this reduction. The calculations of Figure 5.7 and 5.8 demonstrate the above observation. The explanation is as follows. A solar cell is a two-dimensional structure with the bus bar connected to the terminal contact. At open circuit conditions there is a transversed current density flowing through the contact finger to the collecting bus bar where it will eventually balance out the injected dark current density. With higher surface contact resistance, the potential difference under the grid contact is reduced. This implies less injected dark current density and hence a smaller reduction in open circuit voltage. This is shown as Figure 5.9 with two different surface contact resistances where both curves are plotted against each open circuit voltage respectively.

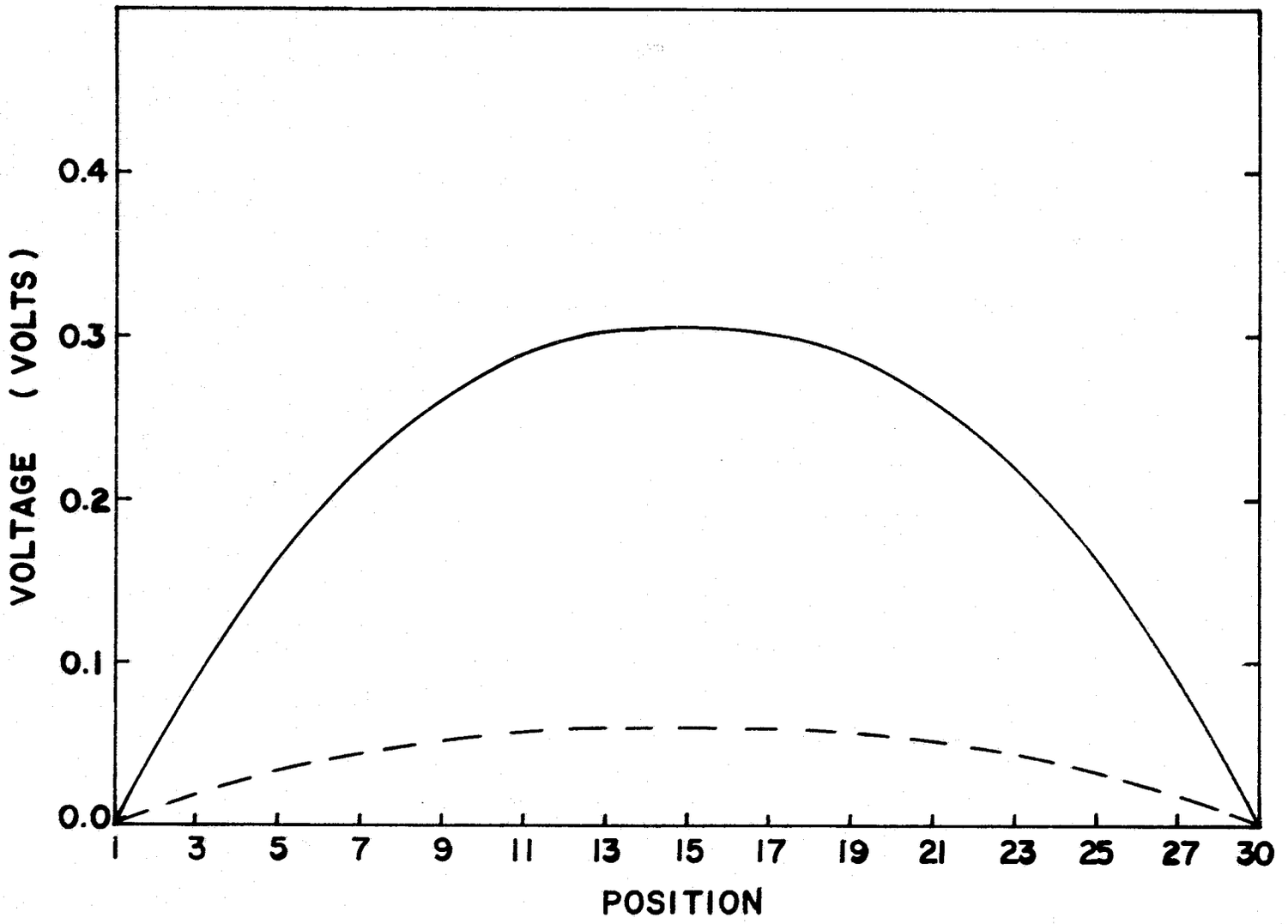

Figure 3.6. Photovoltaic potential at short circuit for one sun and five sun input power intensities with R_{SH} and R_C to be 500 $\Omega/\square$ and 10^{-7} Ω-cm^2 respectively. One AMO (dashed line), five AMO (solid line).

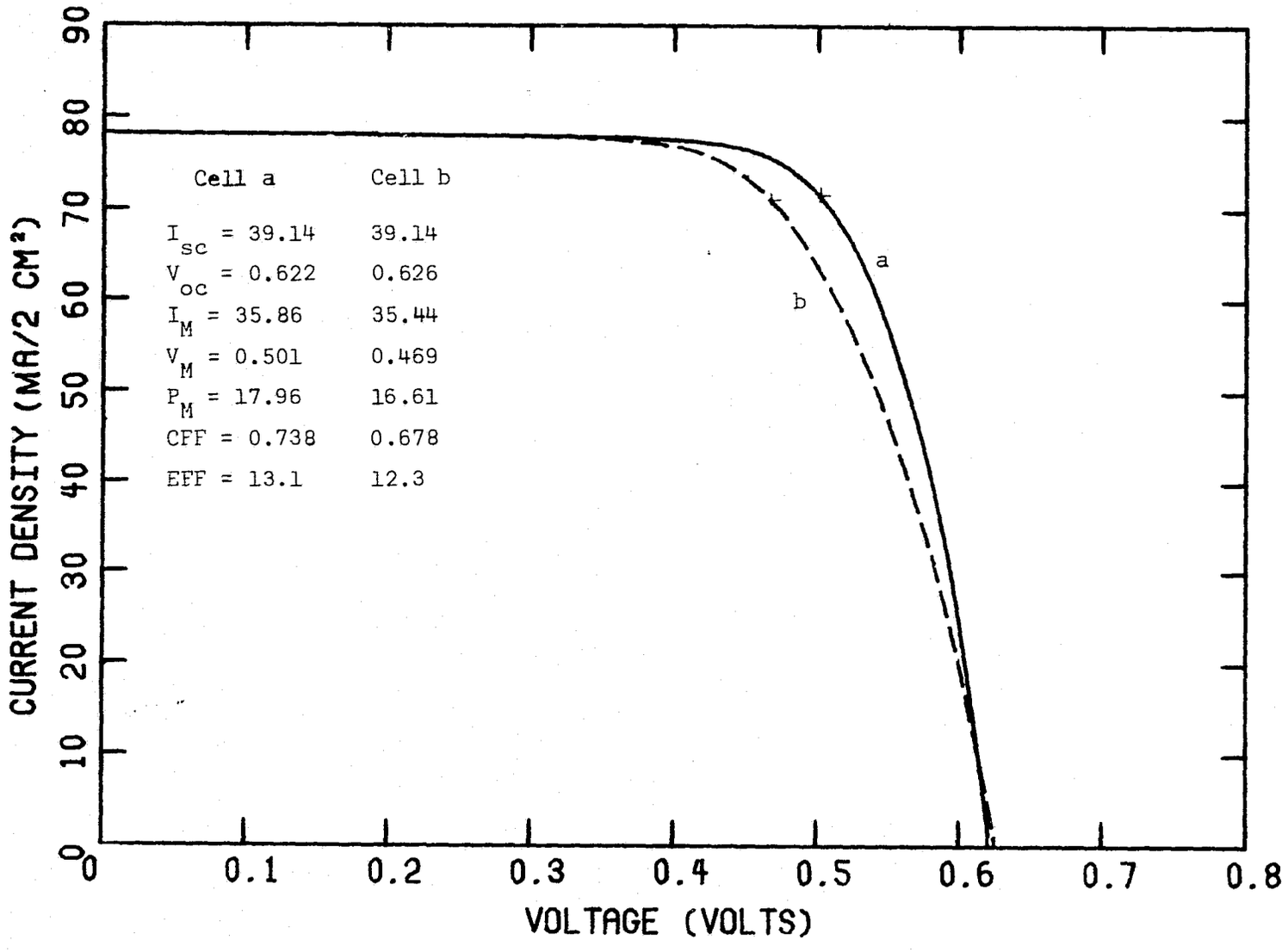

Figure 5.7. Photovoltaic I-V characteristics. R_{ST} = 500 Ω/□ and R_C = 10^{-7} Ω-cm^2 (a), R_{ST} = 500 Ω/□ and R_C = 0.1 Ω-cm^2 (b).

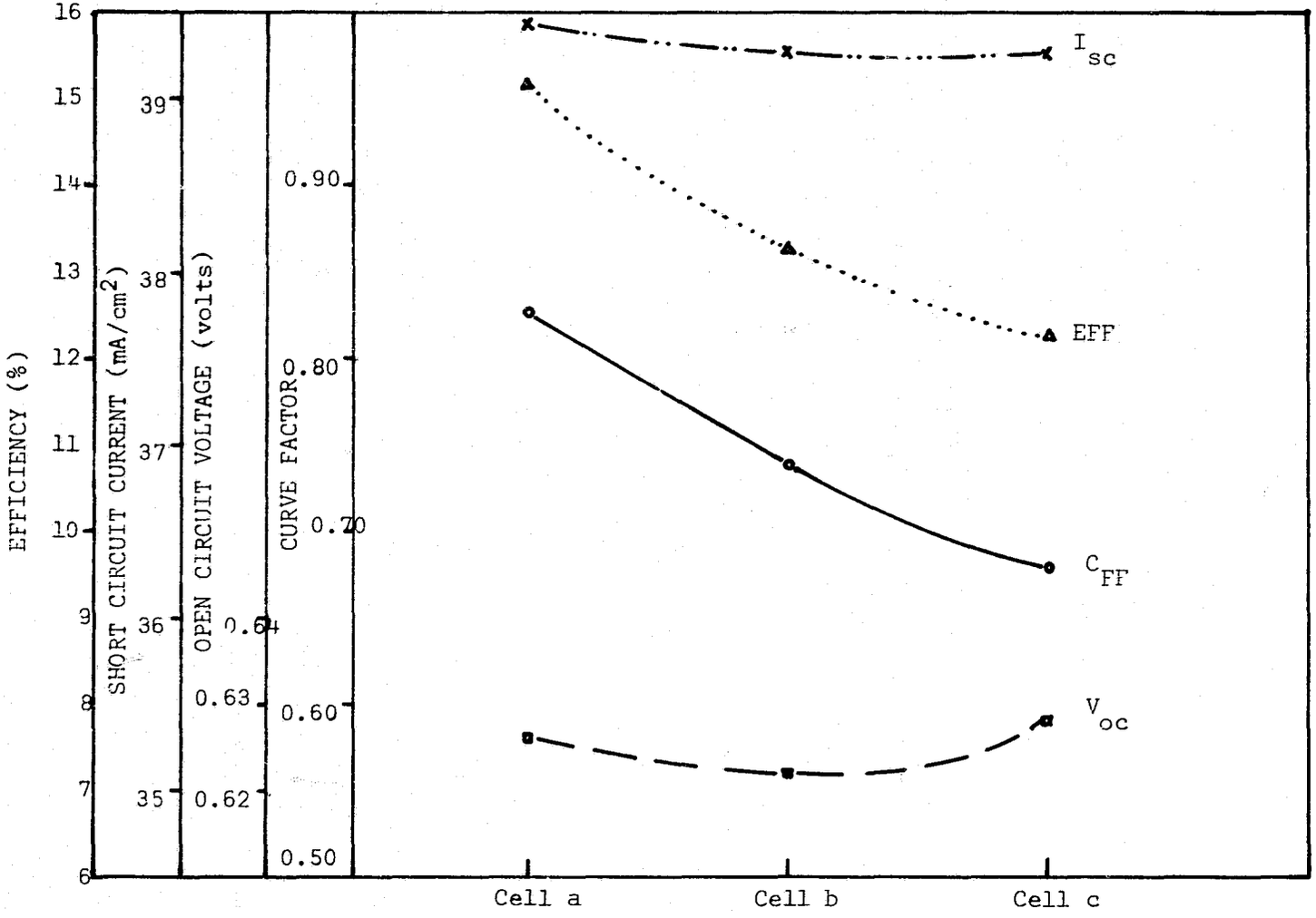

Figure 5.8. Effects of series resistance.
R_{ST} = 10 Ω/□ and R_C = 10^{-7} Ω-cm^2 (cell a)
R_{ST} = 500 Ω/□ and R_C = 10^{-7} Ω-cm^2 (cell b)
R_{ST} = 500 Ω/□ and R_C = 0.1 Ω-cm^2 (cell c)

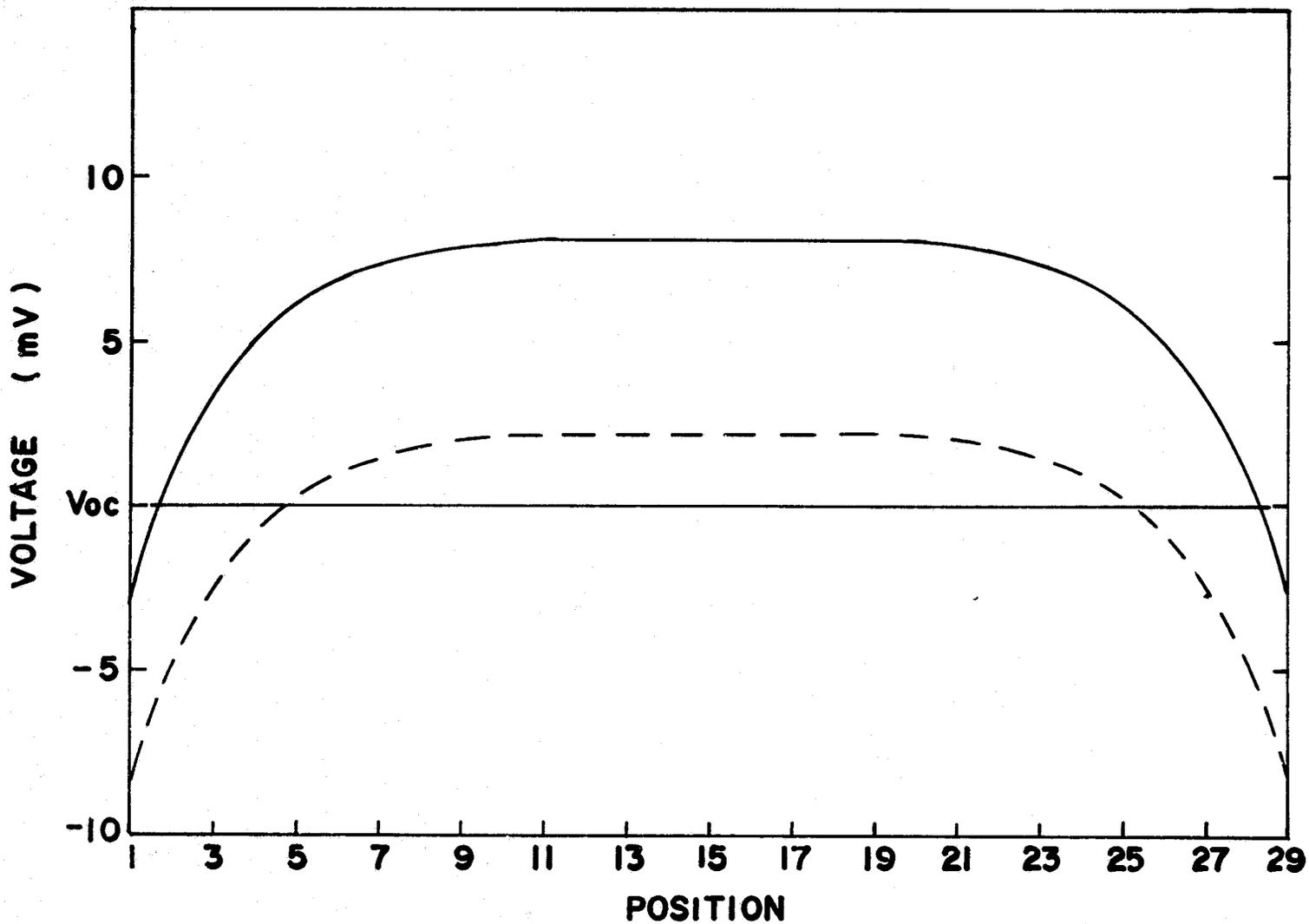

Figure 5.9. Photovoltaic potential at open circuit for five AMO power density.
one ohm surface contact resistance (dashed line)
two ohms surface contact resistance (solid line)

5.2.3 Effects of R_s on Photovoltaic Measurements

Photovoltaic measurements are the single most important method for extracting the important parameters of a solar cell. The effect of series resistance on the photovoltaic measurement is also far more complex than the previously discussed cases. Figure 5.10 is an example of this complexity. Using the same 0.1 Ω·cm cell as previously discussed, consider a short circuit current of 45 mA/cm^2 which corresponds to about 40 mA/cm^2 of short circuit current for the active area only. This value is reasonable in view of the recent improvements in the technology of anti-reflection layers or nonreflection solar cells.

In Figure 5.10, ΔI_1 is the current decrease due to the blocking of the incident light intensity by the grid pattern. ΔV_1 is the reduced open circuit voltage because of the dark current density under the metal contact. ΔI_2 is the reduction current due to an unbalanced dark current density flowing in the illuminating area at short circuit conditions. Finally the reduction ΔV_2 in open circuit voltage is due to the unbalanced light induced in the active area combined with the series resistance explained in the previous section.

The series resistance of the photovoltaic I-V is certainly a non-lumped parameter. One can expect higher effective series resistances for higher current density due to the nature of the transverse current flow in solar cells. However the opposite trend was found for the dark I-V measurements. And this is indeed true as Table 5.1 has previously shown.

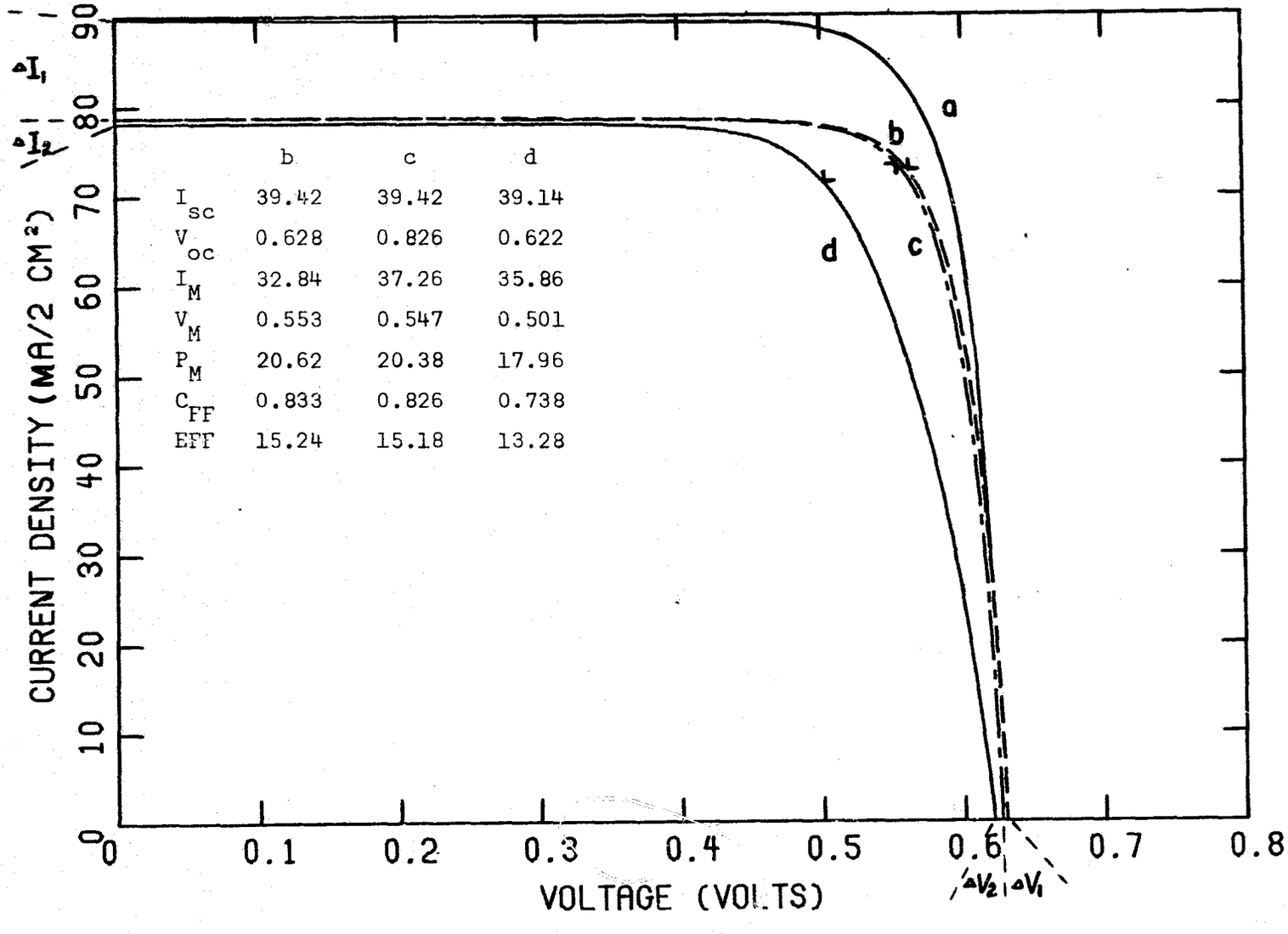

	b	c	d
I_{sc}	39.42	39.42	39.14
V_{oc}	0.628	0.826	0.622
I_M	32.84	37.26	35.86
V_M	0.553	0.547	0.501
P_M	20.62	20.38	17.96
C_{FF}	0.833	0.826	0.738
EFF	15.24	15.18	13.28

Figure 5.10. One-and two-dimensional photovoltaic I-V characteristics. One-dimension with total area (a), one-dimension with active area (b), two-dimension with total area and no series resistance (c), two-dimension with total area and series resistance (d).

Table 5.1 (a). $R_c = 10^{-7}\ \Omega\cdot cm^2$, $\rho_b = 500\ \Omega/\square$.

($mA/2cm^2$) Current density	Photovoltaic R_s (Ω)	Dark R_s (Ω)
200.00	-	0.15
76.58	1.03	0.22
71.72 (I_M)	0.84	0.23
56.80	0.75	0.24
24.71	0.72	0.33

Table 5.1 (b). $R_c = 0.1\ \Omega\cdot cm^2$, $\rho_b = 500\ \Omega/\square$.

Current density $mA/2cm^2$	Photovoltaic R_s (Ω)	Dark R_s (Ω)
100.00	-	0.68
73.50	1.40	0.70
70.88	1.38	0.71
63.82	1.28	0.72
46.77	1.14	0.73
19.97	0.98	0.74

The profound effects of series resistance on V_{oc}, I_{sc}, C_{FF} (curve factor), E_{FF} (efficiency) and the effect of incident light intensity is summarized in Figures 5.8 and 5.11. Figure 5.8 shows the effects of different combinations of series resistance on the performance of solar cells, while Figure 5.11 shows the effects of sheet resistance under different input power intensity.

It is clear that the major effect of the internal series resistance is the deterioration of the curve factor. The conversion efficiency is reduced with higher internal series resistance or higher illuminating intensity at the same resistance.

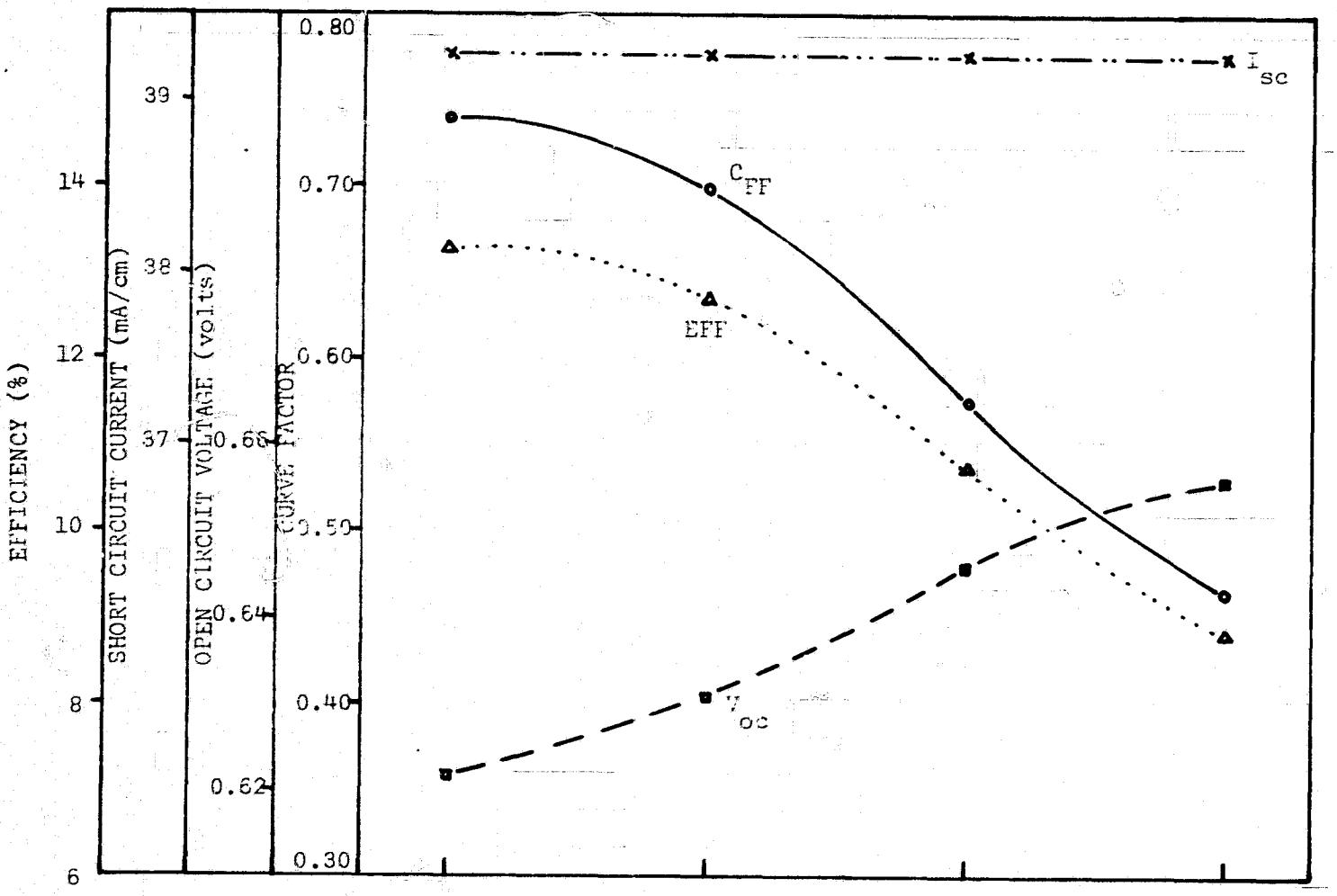

Figure 5.11. Effects of series resistance at different AMO intensities with sheet resistance of 500 Ω/□. a, b, c, d for one, one and one-half, three and five AMO power densities respectively.

5.3 The Determination of R_s in Photovoltaic Measurements

As discussed in the previous section, it is not possible to define a constant lumped series resistance which can be used over a wide range of currents. However, the concept of a lumped series resistance has appeared so frequently in the literature that it is useful to compare the two-dimensional results with experimental measurements of lumped resistance values. Over small current changes such as near the peak efficiency the use of a lumped resistance as a first order approximation perhaps still has some use.

Historically, several experimental methods have been proposed to measure the effective series resistance. All of those methods deduce R_s from comparisons of the photovoltaic I-V characteristic at several varying light intensities. Swanson [51] was the first to propose the method of translations along the voltage and current axes by the amount of $R_s \cdot \Delta I_L$ and ΔV where ΔI_L is the difference in short circuit current of two different light intensities. This method was later adopted extensively in Wolf's work [51]. Handy [52] proposed a somewhat different method of measuring the slope of all the connecting points which are at a fixed current density ΔI from each short circuit current at different illumination intensities.

The success of the above methods rely on a linear translation of the photovoltaic I-V characteristic with varying incident light intensity and the existance of a constant R_s with respect to the different current levels. Unfortunately the series resistance in solar cells is a nonlinear function of the current intensity and the above conditions cannot be satisfied in general. Figure 5.12 shows calculated results using a

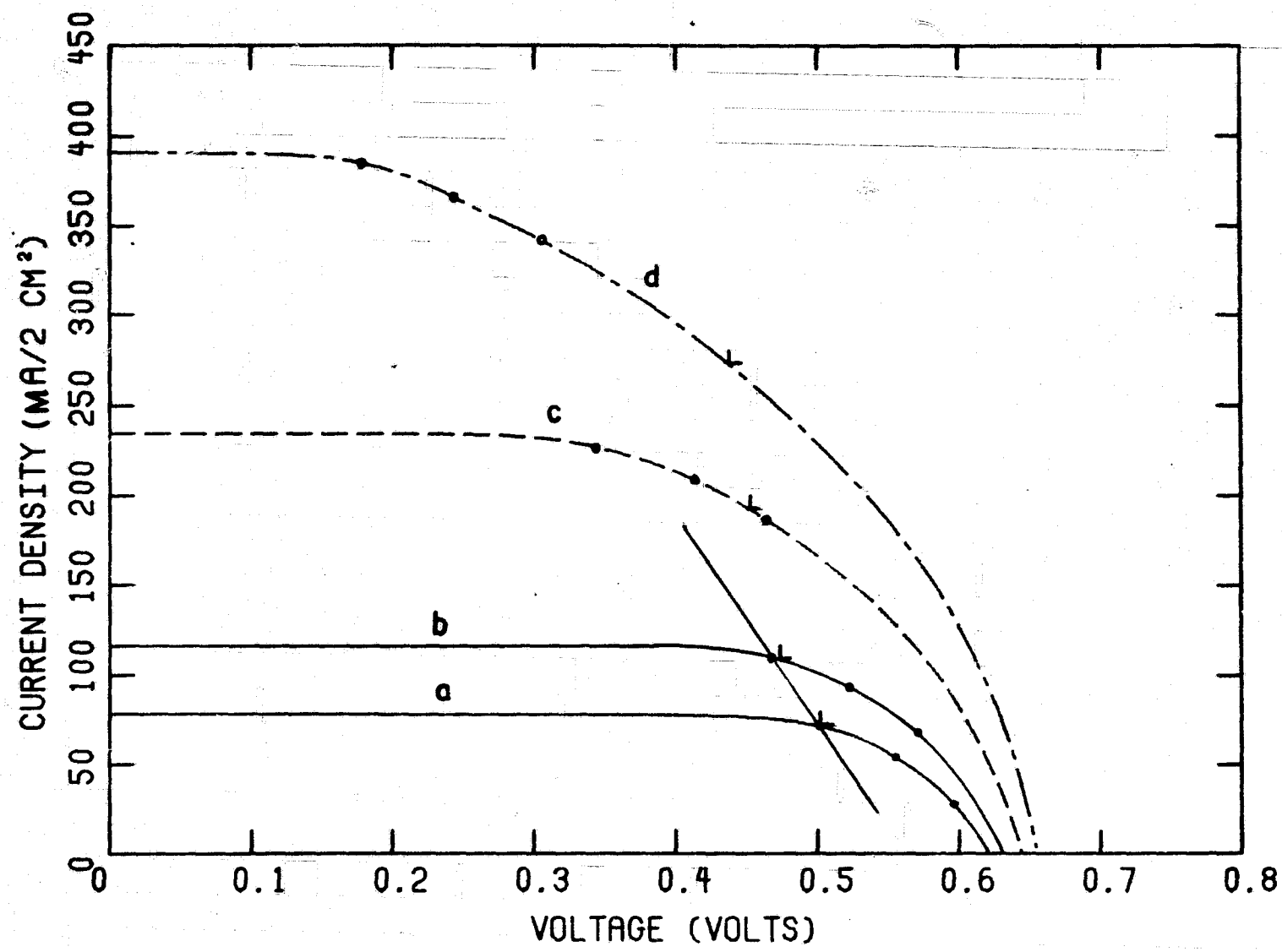

Figure 5.12. Photovoltaic I-V characteristics at different AMO intensities. One AMO (a), one and one-half AMO (b), three AMO (c), five AMO (d).

two-dimensional model of the photovoltaic I-V characteristics at 1, 1.5, 3, and 5 suns power density. The calculated series resistance for 1-sun by connecting to the corresponding point of different intensity are tabulated in Table 5.2.

Table 5.2. Calculated effective series resistance by Handy's method.

	Resistance values in Ω		
$\Delta I(mA/2cm^2)$	1.5-Sun	3-Sun	5-Sun
6.56	0.844 (Ω)	0.970	0.984
25	0.833	0.911	0.964
50	0.644	0.844	0.926

The results of Table 5.2 are just what might be expected of the higher effective series resistance for higher current intensities for the photovoltaic measurements.

5.4 Experimental Justification of the Distributed Resistance Model

It has been found experimentally that there are always some deviations in the current-voltage characteristics of a solar cell from the first order lumped resistance model [51]. Here the distributed resistance model shows its superiority over the old lumped resistance model. Three categories of solar cells have been chosen to demonstrate the correlation between experimental results and the theoretical calculation.

5.4.1 Solar Cells With Very High Sheet and Contact Resistance

Solar cell no. D-6-1 has a very shallow junction depth of about 0.07 μm. This results in a very high sheet resistance. Contact resistance is also very high on the surface and/or the back contact to the 10 Ω·cm base substrate. Sheet resistance could be estimated from the equations in Section 2.6 as

$$\rho_{ST} = \frac{h^2}{A} \frac{2kT}{qI_T}, \qquad (5.6)$$

where I_T is the experimentally measured transition current between an exp(qV/kT) dependence and an exp(qV/2kT) dependence. The calculated sheet resistance obtained from the data in Figure 5.13 is a very high value of 8220 Ω/□ . This is what might be expected for such a shallow junction solar cell. It has been found experimentally that the sheet resistance may increase very fast as the junction depth is reduced [41].

The contact resistance for this cell could be estimated at a much higher current level because of differences between the dark and static I_{sc}-V_{oc} characteristics. This calculated value is about 2.8 Ω for the 2 cm^2 cell of D-6-1. The theoretical prediction is very close to the experimental result in Figure 5.13 when the value of 8200 Ω/□ for sheet resistance and 2.84 Ω for total contact resistance is used. The diode n factor is about 5 at voltages above 0.45 volts. It is not possible to describe this behavior with a lumped resistance at all current or voltage levels for both dark and photovoltaic I-V measurements.

5.4.2 Solar Cells with Median Sheet and Contact Resistance

Solar cell no. D-6-2 has a junction depth of about 0.3 μm and a low surface doping density which results in a sheet resistance value of about 940 Ω/ . The total contact resistance is about 0.20 Ω. Figures 5.14 and 5.15 show good correlation to the dark and photovoltaic current-voltage characteristics using these parameters.

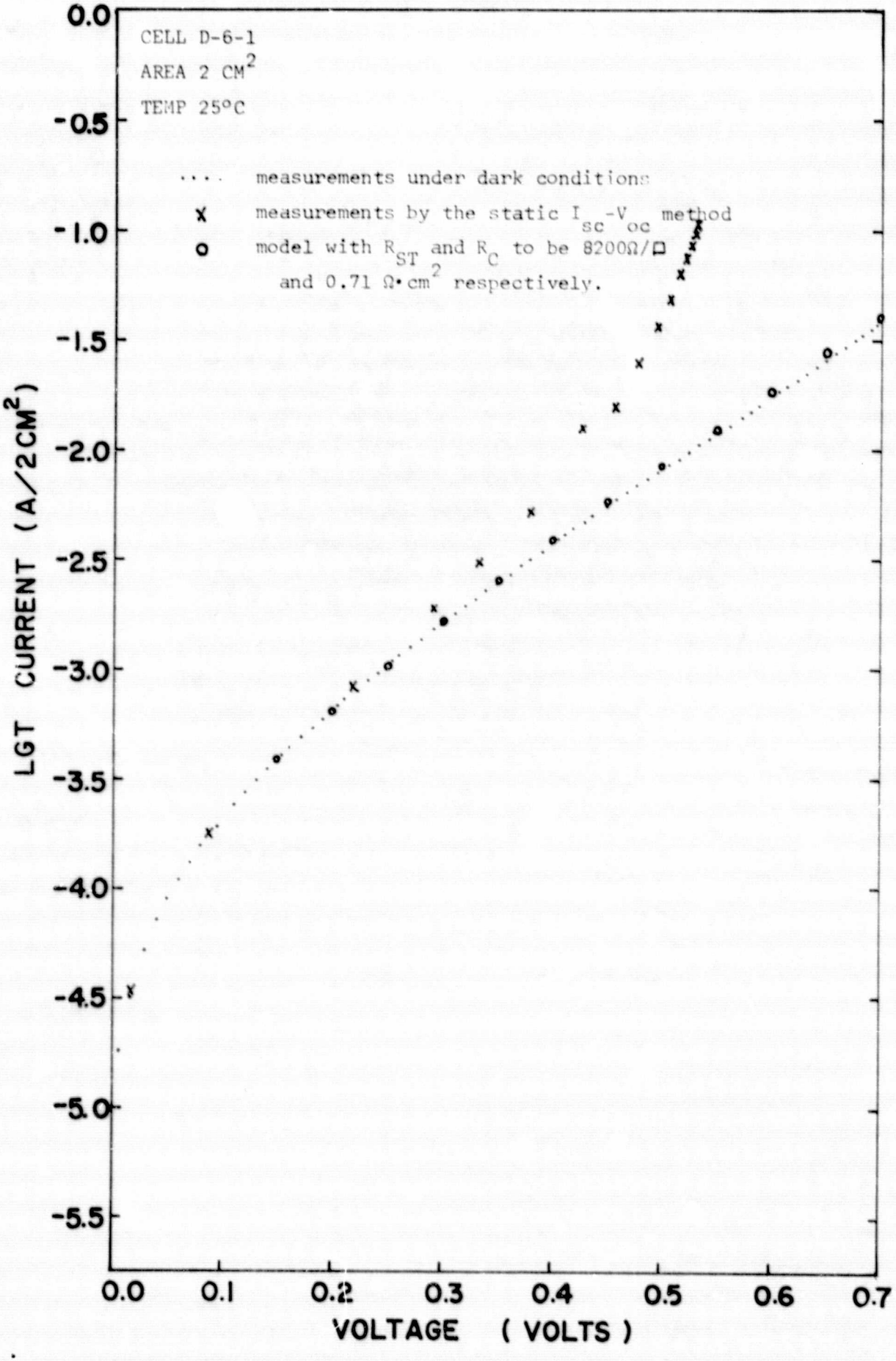

Figure 5.13. Comparison of the dark I-V characteristics of D-6-1.

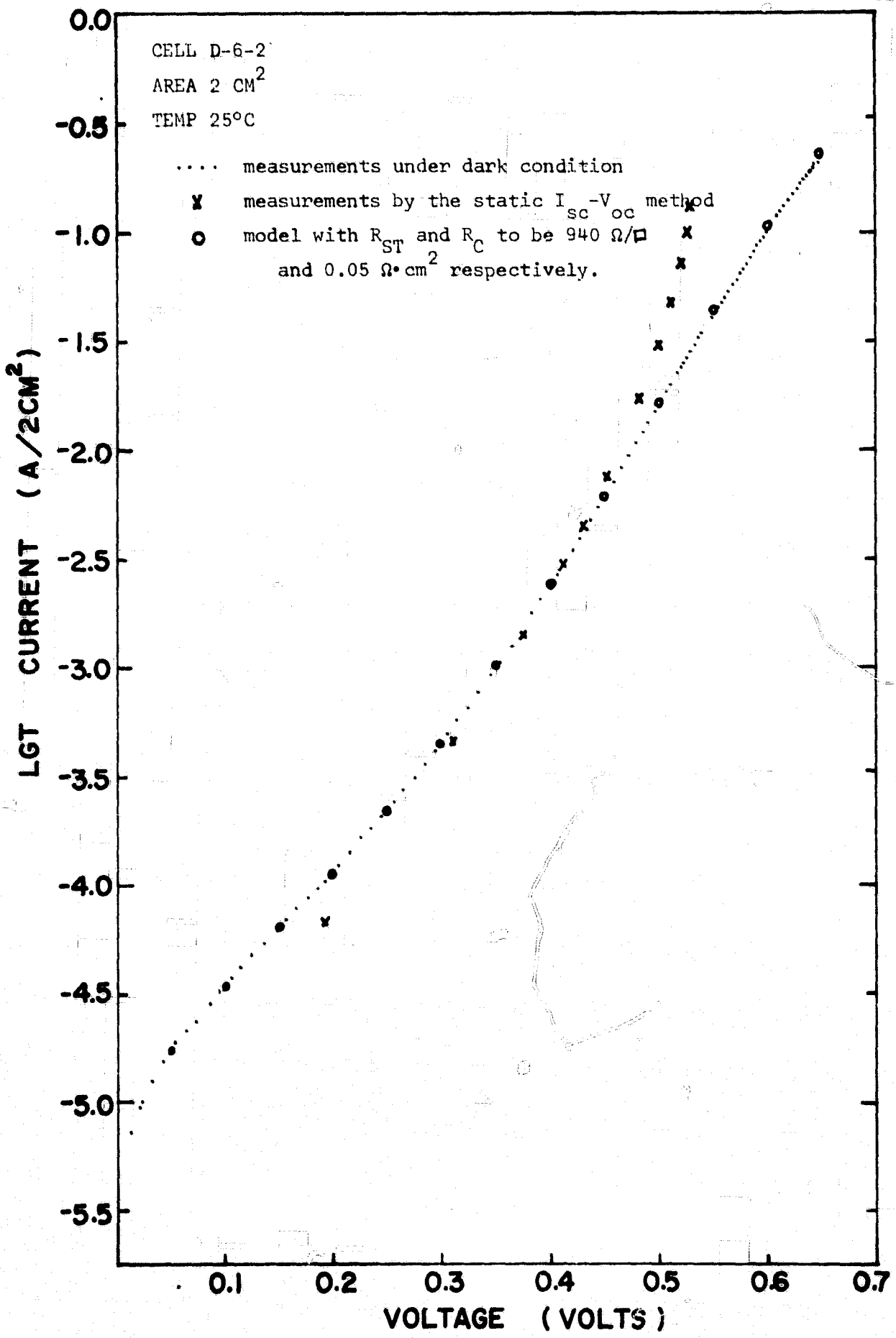

Figure 5.14. Comparison of the dark I-V characteristics of D-6-2.

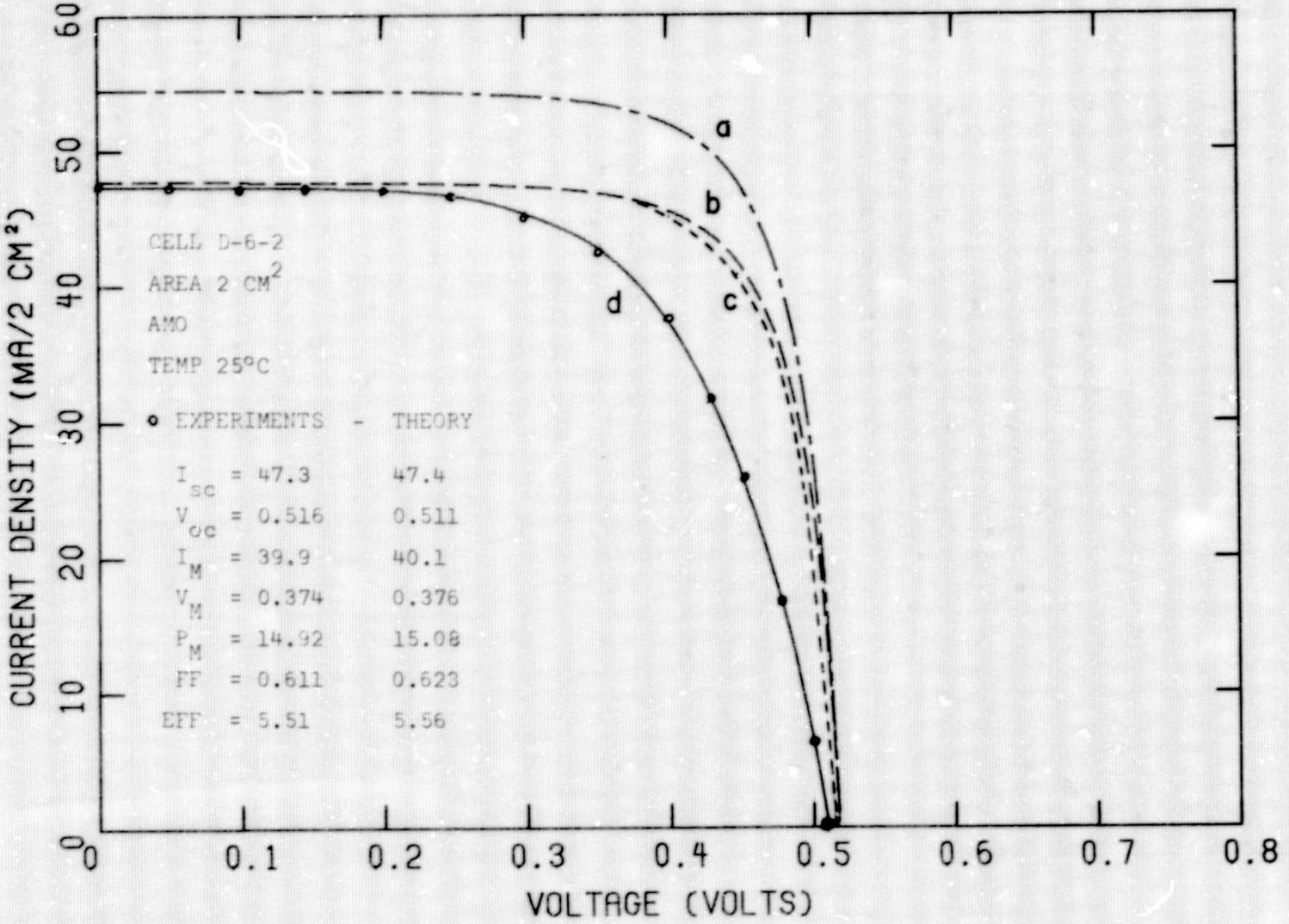

Figure 5.15. Comparison of the photovoltaic I-V characteristics of D-6-2. One-dimension with total area (a), one-dimension with active area (b), two-dimension with total area and no series resistance (c), two-dimension with total area and series resistance (d).

5.4.3 Solar Cells with Low Sheet and Contact Resistance

Solar cell no. D-6-3 has a 0.7 μm junction depth on a 0.1 Ω·cm base substrate. The resultant sheet and contact resistances are very low. Again the distributed model's prediction is very good as shown in Figure 5.16 and 5.17.

5.5 Summary

This section has discussed the important effects of sheet resistance and contact resistance on terminal device parameters of short circuit current open circuit voltage and curve factor. Calculations using a two-dimensional model of sheet resistance have emphasized the limitations of modeling a solar cell by a lumped single resistance value. The results of the two-dimensional distributed resistance model have been found to be in good agreement with experimental data on devices with both large and small values of sheet and contact resistance. Values of sheet resistance and contact resistance can be found by comparing theory and experiment at large current densities.

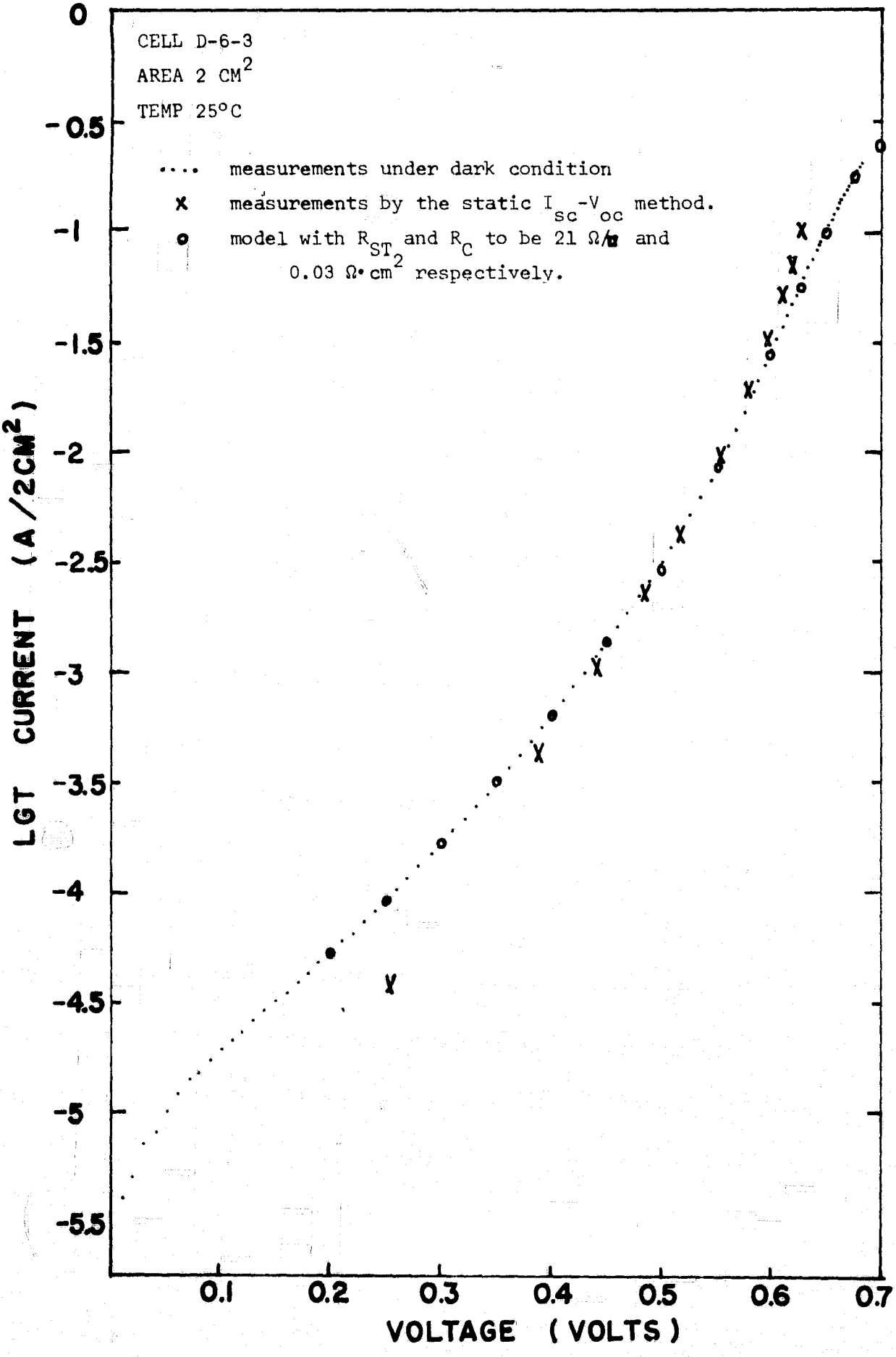

Figure 5.16. Comparison of the dark I-V characteristics of D-6-3.

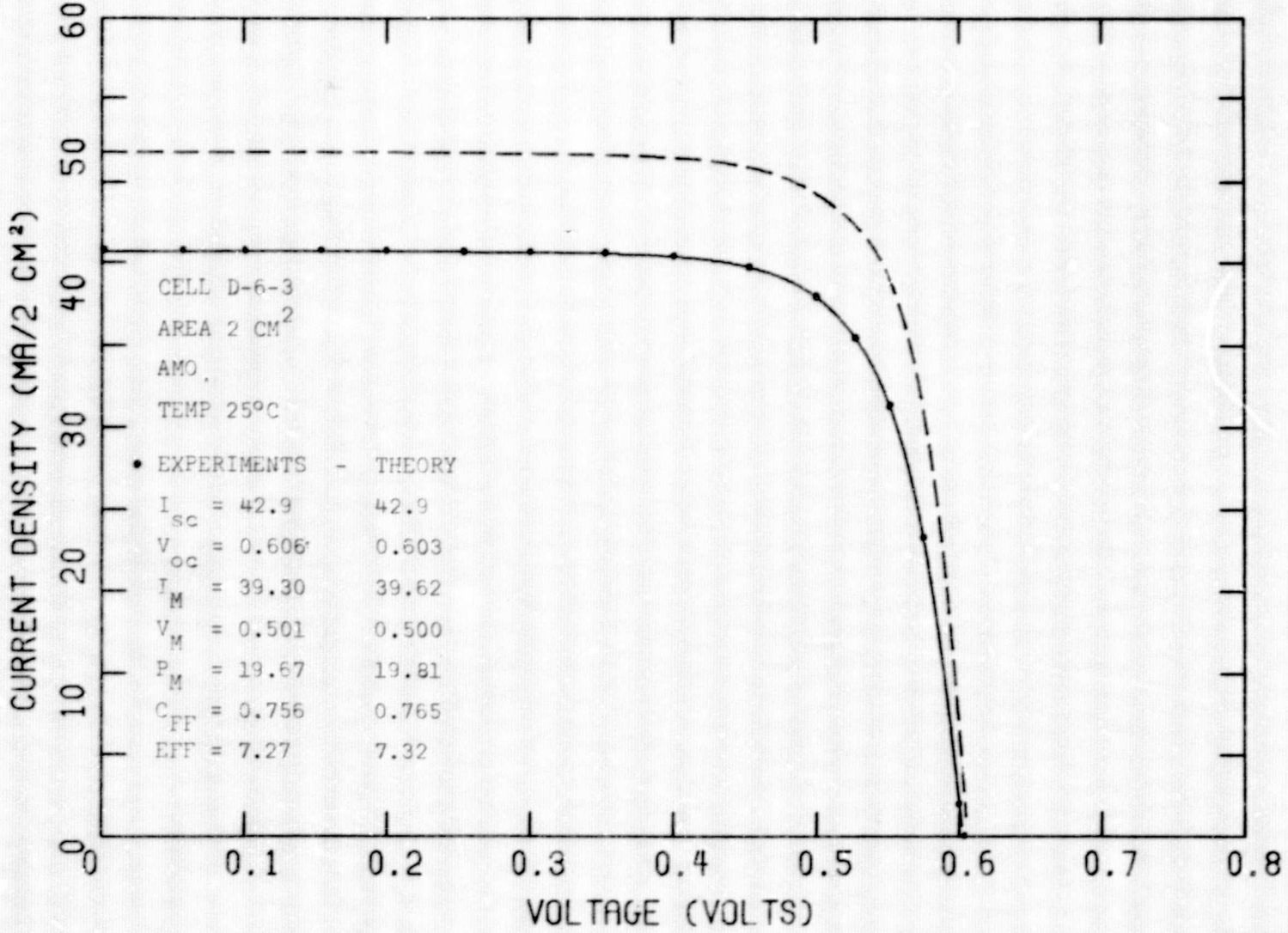

Figure 5.17. Comparison of the photovoltaic I-V characteristics of D-6-3. One-dimension with total area (dashed line), two-dimension with total area and series resistance (solid line).

6. EFFECTS OF IMPURITY GRADIENTS ON SOLAR CELLS

6.1 Introduction

The use of doping gradients to give built-in fields to enhance the performance of solar cells has been proposed for many years. Experimental measurements on BSF cells which have a back surface high-low junction certainly indicate that such an abrupt doping gradient enhances solar cell performance. The use of more gradual impurity gradients has been investigated in this phase of the research as a means of improving solar cell performance and efficiency.

6.2 Base Layer Impurity Gradients

The details of this phase of the work are contained in Appendix 9.1. This appendix reproduces a paper which has been accepted for publication in Solid-State Electronics. The major conclusions of this work are summarized there.

6.3 Surface Layer Impurity Gradients

The use of a built-in surface drift field has been proposed to enhance the collection of short wavelength photons for many years [54]. It is the purpose in this section to examine the effect of incorporating such surface drift fields on the operation of silicon solar cells.

The solar cell which has been modeled is a BSF cell with a surface doping density of $2 \times 10^{19}/cm^3$ and a junction depth of 0.2 μm. The diffused doping profile for the n^+pp^+ cell is assumed to be constant or exponential thus producing either zero or a constant surface drift field in the direction of the collection junction. Also a good surface

lifetime of L_D(MAX) was assumed. An SiO antireflection layer of 800 Å was also used.

Surface recombination velocity (SRV) is well known as a photon loss mechanism at the surface. The carriers generated by short wavelength photons recombined at the surface instead of being collected at the p-n junction. The effects of incorporation of surface drift fields can be measured by the amount of reduction in "dead layer" thickness and also by the increase in short circuit current density. The models and results are shown below in Table 6.1 and 6.2. In this work the dead layer thickness is defined as the depth from the surface at which the minority carrier current changes from a flow toward the surface to a flow toward the p-n junction.

It is clear that the built-in surface drift field indeed enhances the collection efficiency, although the overall conversion efficiency is lower. The explanation is fairly easy. The incorporation of a surface field through the grading of the doping profile inevitably reduces the doping density at the edge of the p-n junction. Hence the back injection component of current is increased and the open circuit voltage and conversion efficiency is therefore lowered. Thus it is not clear that a surface layer drift field leads to an enhanced efficiency. In fact the results of Table 6.1 and 6.2 indicate just the opposite trend. It appears that minimizing the dark current component due to injection into the surface layer is much more important than enhancing the collection efficiency.

C2

Table 6.1. Models of solar cell with the surface layer impurity gradients.

Device No.	Surface Doping Density	Surface Doping Profile	Surface field (volts/cm)	SRV	Surface diffusion length	Base Doping 0.4 Ω-cm	High-Low Junction
F-1	$2x10^{19}$	constant	0	10^5	L_D(MAX)	$5.6x10^{16}$	$1x10^{19}$
F-2	$2x10^{19}$	exponential	4000	10^5	L_D(MAX)	$5.6x10^{16}$	$1x10^{19}$
F-3	$2x10^{19}$	exponential	7000	10^5	L_D(MAX)	$5.6x10^{16}$	$1x10^{19}$

Table 6.2. Calculated results of devices F-1, F-2 and F-3.

Device No.	I_{sc}	V_{oc}	C_{FF}	E_{FF}	Dead layer thickness (A)
F-1	40.85	0.675	0.840	17.13	200
F-2	41.91	0.652	0.836	16.86	90
F-3	42.17	0.640	0.833	16.64	40

7. EFFECTS OF NON-UNIFORMITIES ON SOLAR CELL PERFORMANCE

7.1 Introduction

This section explores the importance of several non-uniform effects on solar cell performance. The effects considered are non-uniformities within the plane of the illuminated surface as opposed to non-uniformities with distance into the cell from the illuminated surface. The two dimensional nature of the ohmic grid fingers as discussed in previous sections is one type of surface area non-uniformity. Other effects discussed in this section include variations in surface recombination velocity, especially under the contact area, resistivity striations across a cell, and non-uniform surface illumination. The existance of the two-dimensional model makes possible most of these calculations.

7.2 The Effect of the Difference in SRV under the Contact Fingers and Anti-reflection Coated Area on the Operation of Silicon Solar Cells

Because of the two-dimensional configuration of a solar cell, the surface recombination velocity (SRV) is different under the contact fingers from the value under any anti-reflection layers. The area under the anti-reflection layer has, in general, a lower SRV due to the better lattice matching and lower interface surface states. The area under the ohmic contact has a much higher SRV where carriers will recombine. Hence the difference in SRV under the contact and antireflection areas should be considered in the two-dimensional modeling of a solar cell.

The theoretical upper limit of SRV has been found to be half of the thermal velocity of the carriers in the material by the principle of detailed balance [55]. This upper limit of SRV is about 5×10^{6} cm/sec for silicon at room temperature. However it is quite common in this limiting case to set SRV to infinity which is equivalent to taking the excess carrier density to be zero at the ohmic surface.

The calculations for different SRV have been performed for device D-2 and the results of dark I-V characteristics are shown as Table 7.1.

Table 7.1. Comparison of the dark I-V characteristics for different SRV.

D-2 Voltage (volts)	(mA/cm^2) Anti-Ref. Layer	(mA/cm^2) Ohmic Contact	(mA/cm^2) Experiment
0.45	0.2095	0.2099	0.2233
0.50	0.7291	0.7324	0.7305
0.55	2.95	2.97	2.94
0.60	14.15	14.30	14.10
0.65	78.55	79.93	79.24
0.70	470.24	478.79	-

Since the calculated dark I-V characteristics is almost indistinguished for different SRV values at the diffused surface, it can be expected that the consideration of the ohmic contact under the grid patterns has a very negligible effect on calculating the resultant conversion efficiency.

In the first order model of solar cells the reverse saturation current density into the surface layer can be expressed as [10]

$$J_{so} = q\frac{D_p}{L_p}\frac{n_i^2}{N_d}\left[\frac{\frac{S_p L_p}{D_p}\cosh\frac{X_j}{L_p} + \sinh\frac{X_j}{L_p}}{\frac{S_p L_p}{D_p}\sinh\frac{X_j}{L_p} + \cosh\frac{X_j}{L_p}}\right]. \qquad (7.1)$$

In a heavily doped surface region, $\frac{S_p L_p}{D_p}$ is typically larger than 1 for SRV values in the range of $10^5 \sim 10^7$ cm/sec. Hence J_{so} can be approximated as

$$J_{so} \simeq \frac{D_p}{L_p} \frac{n_i^2}{N_d} \coth \frac{X_j}{L_p}, \tag{7.2}$$

and is independent of the value of SRV in the range of 10^5 cm/sec to infinite.

The conclusions above are not valid if the SRV has a low value under the anti-reflection layer. In this case the surface diffusion current density does increase for higher SRV and the resultant conversion efficiency will be reduced somewhat, especially for low base resistivities such as 0.1 Ω•cm or lower.

However for most silicon solar cells with base resistivities equal to or larger than 1 Ω•cm, the dominance of base diffusion current implies that the high value of SRV under the grid pattern can be neglected. The small contact area of 7 to 10 percent of the total surface also supports the above conclusion.

7.3 The Effect of Substrate Resistivity Striations on the Operation of Silicon Solar Cells.

It is known that there are resistivity striations over a silicon surface which has been chem-mechanically polished with an aqueous based silica solution [56]. Indeed the resistivity has been reported to vary between 15 Ω-cm and 7 Ω-cm on the surface of a nominal 10 Ω-cm wafer. The shape of the doping profile looks like a "well" with lower resistivity locating in the center of the wafer and higher resistivity on the peripheral [57].

The example given below represents calculations of a standard 10 Ω-cm n+p silicon solar cell with a short circuit current density of 40 mA/cm^2. The surface sheet resistance is assumed to be 150 Ω/□ with the NASA 10-finger grid pattern. The calculations of solar cell parameters with the extreme base doping densities of 7 Ω·cm and 15 Ω·cm are shown in Table 7.2 with that of the nominal 10 Ω-cm cell. The photovoltaic I-V characteristics are shown in Figure 7.1.

Table 7.2. Calculated results of solar cell with different substrate resistivity striations.

	I_{sc} mA/cm^2	V_{oc} Volts	I_M mA/cm^2	V_M volts	P_M mW/cm^2	CFF	EFF %
7 Ω-cm $9x10^{14}$	34.19	0.542	32.05	0.452	14.49	0.782	10.71
10 Ω-cm $1.25x10^{15}/cm^3$	34.19	0.531	32.23	0.440	14.18	0.781	10.48
15 Ω-cm $1.8x10^{15}/cm^3$	34.19	0.521	32.41	0.429	13.91	0.781	10.28
Gaussian	34.19	0.529	32.29	0.437	14.11	0.780	10.43

It is clear from Table 7.2 that the major difference in these calculations is in the open circuit voltage with a smaller change in the conversion efficiency.

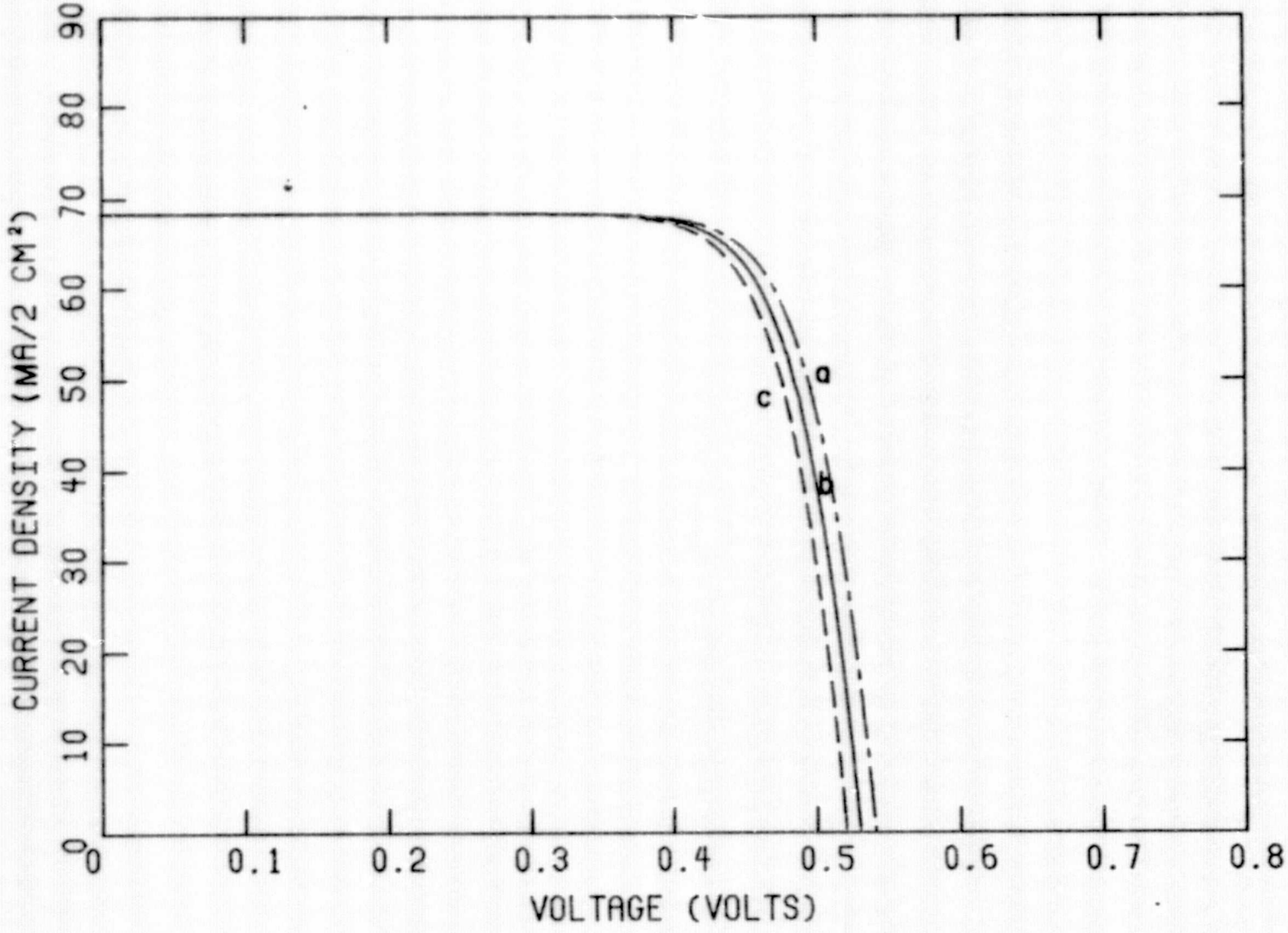

Figure 7.1. Photovoltaic I-V characteristics with different base layer resistivities. (a) 7Ω·cm, (b) 10 Ω·cm, (c) 15Ω·cm.

The actual doping profile has been modeled as an example by a Gaussian function with the peak resistivity of 15 Ω-cm. The result is shown in Table 7.2 for a 50 percent resistivity striation. It should be noted here that the apparent variation of about 50 percent in the resistivity has been reported to be reduced to less than ±5 percent after a 15 minute bakeout at about 150°C in a partial vacuum [56]. Hence the resistivity striation of the base substrate of a solar cell will not significantly change the results calculated from the nominal resistivity especially when concerned with the conversion efficiency.

7.4 The Electrical Output and Photovoltage of a Non-Uniformly Illuminated Silicon Solar Cell

7.4.1 Introduction

The uniformly illuminated solar cell usually does not exist despite the frequent use of this in a one-dimensional analysis. In any practical solar cell there are always some constraints that restrict the uniformity. The non-uniformity results at least from the opaque metal contact and sometimes from the shadow of structural elements such as antennas, satellite bodies, etc.

The power losses of a nonuniformly illuminated solar cell are found to be not just proportional to the shadowed area but larger because of the nature of the partial illuminated p-n junction. Moreover the nonuniformly illuminated solar cell produces a transverse photovoltage parallel to the junction as current flows to the non-uniformly illuminated areas. This section discusses the characteristics of such non-uniformly illuminated silicon solar cells. The degradation of conversion efficiency and the variation of photovoltage by the non-uniformity of illumination are presented and discussed.

The equation of two-dimensional carrier flow in a non-uniformly illuminated junction has been developed elsewhere [58][59]. The transverse voltage at the plane of a p-n junction satisfies the equation

$$\sigma \cdot \frac{d^2V}{dy^2} = I_o(e^{qV/nkT}-1)-I_{sc} \qquad (7.3)$$

where σ is the longitudinal conductivity of the diffused surface and equals $q \int_o^{x_j} \mu N_s(x)dx$, μ is the mobility of the majority carrier, N_s is the doping density and x_j is the junction depth.

Although the analytical solution of the above equation is possible for very special contacts and/or partially illuminated cells, there is no general solutions for an arbitrary non-uniformly illuminated case. Hence a general two-dimensional program has been developed which can handle any non-uniformity of illumination at any arbitrary illumination level (See Appendix 9.2).

7.4.2 Non-Uniformly Illuminated Junctions

Although the actual shadows of a non-uniformly illuminated solar cell are usually of complicated geometry and time-varying, one specific example will be presented to investigate the physical processes in a non-uniformly illuminated solar cell. This is the case of an abrupt illumination boundary which is assumed to be perpendicular to the finger contact of a solar cell. This approach should show all the aspects of a non-uniformly illuminated solar cell and pave the way for the analysis of more general cases.

The solar cell in this analysis is a conventional 10 Ω-cm silicon cell of 40 mA/cm^2 short circuit current density and with the NASA 10-finger grid pattern. The metal contact resistance was assumed negligible and values of 150 Ω/□ was assumed for the surface sheet resistance. The light level was assumed to produce 40 mA/cm^2 short circuit current density under

the illuminated area. The non-illuminated area has of course no light-generated current but a detrimental power consuming forward current density.

7.4.3 Photovoltage Profile Across the Non-uniformly Illuminated Boundary

In a uniformly illuminated p-n junction the photovoltage is almost constant except in the vicinity of the metal contact. This is shown in Figure 7.2 where the dashed lines represent the photovoltage at each terminal voltage respectively along line MM' of Figure 5.3. The junction photovoltage which is lower than the terminal voltage at 0.6 and 0.7 volts is due to the dominance of the forward current which is in a direction opposite to the light-generated current. Shown in the same figures are curve for the case of non-uniform illumination over half of the active area where the abrupt light-dark boundary is indicated as a verticle dotted line. It is clear that the gradual decay of the photovoltage across this boundary produces a transverse voltage. Additional plots of the photovoltage across a non-uniformly illuminated boundary are shown in Figure 7.3 for full, three quarters, half and quarter active areas respectively at a terminal voltage of 0.45 volts.

One interesting characteristic of a non-uniformly illuminated solar cell is shown in Figure 7.3 where the total forward current is less for the smaller active area because of the smaller photovoltaic potential on the surface. Also the forward current at the shadowed area which is to the right of the lighted area is much higher than that at the terminal voltage. This is because of the transverse photovoltage developed across the light-dark boundary. Since the light can be abruptly changed, the voltage cannot. Hence the degradation of the conversion efficiency by non-uniform illumination is more severe for higher light levels and high sheet resistances.

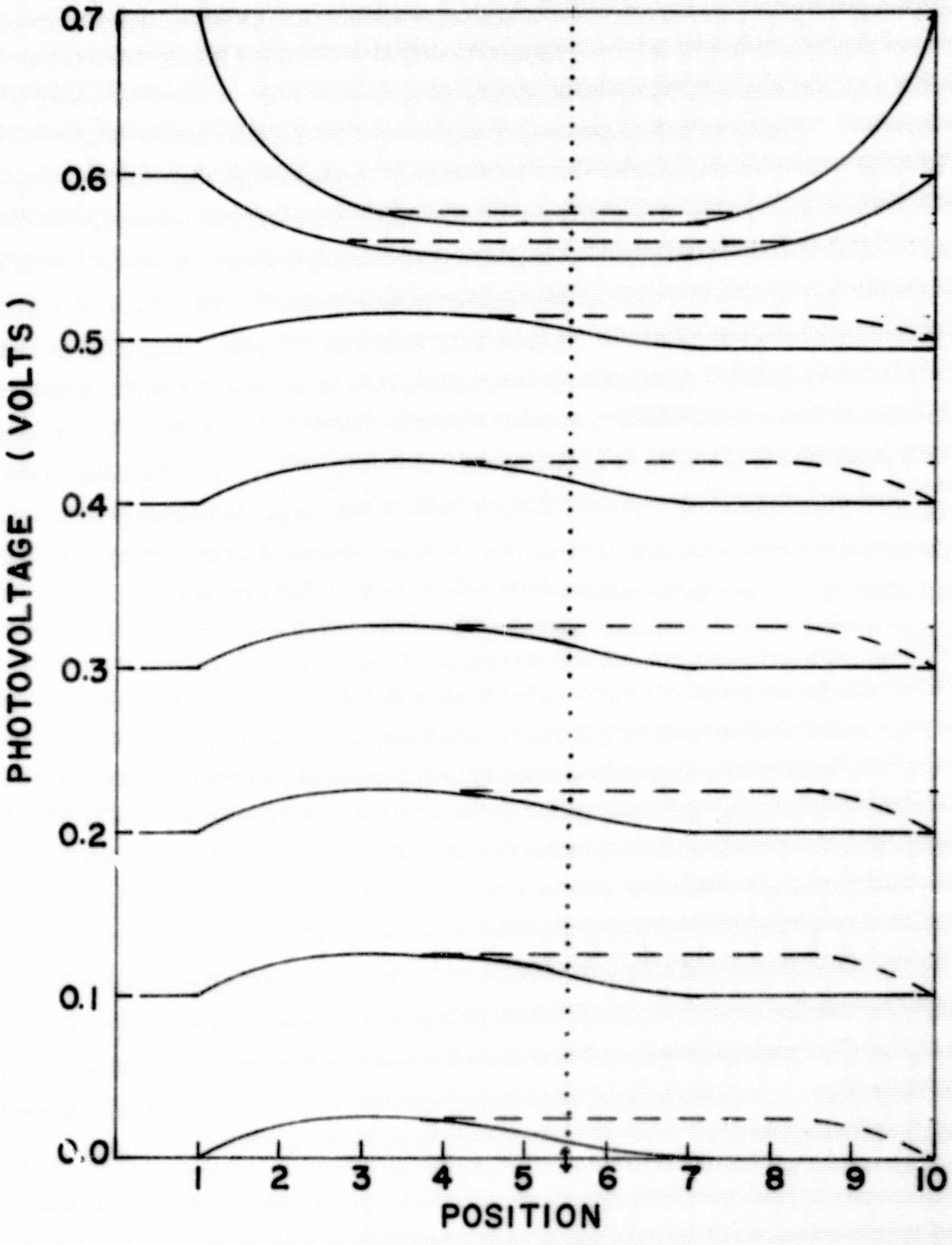

Figure 7.2. Photovoltaic potential profile of uniformly and non-uniformly illuminated cells. Uniform (dashed line), non-uniform (solid line)

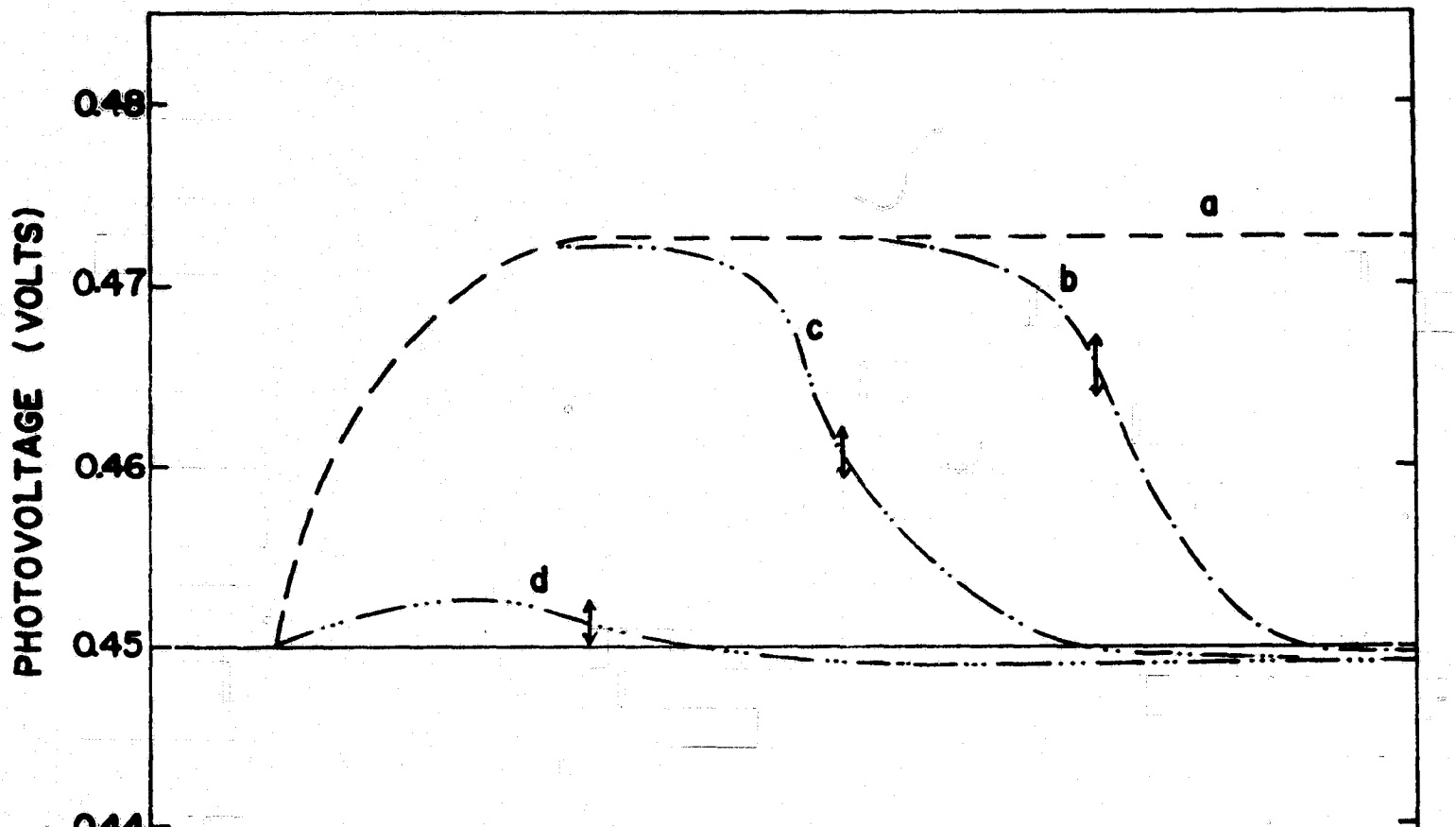

Figure 7.3. Photovoltaic potential profile for several non-uniformly illuminated cells. (a) full, (b) three quarters, (c) half and (d) one quarter of the active area.

7.4.4 Photovoltaic Output of a Non-Uniformly Illuminated Solar Cell

The calculations of the non-uniformly illuminated silicon solar cells are summarized in Table 7.3. The photovoltaic I-V characteristics are shown in Figure 7.4 for several values of illuminated areas. The open circuit voltage and short circuit current is reduced as the illuminated area decreases. The curve factor is found to be better for the smaller active area. The explanation for this is fairly straight-forward. In each case the illuminated area occurs next to the bus contact. Thus the effective resistance through which the current flows is reduced as the active area is reduced. If the center of the cell is illuminated over a small area, the curve factor should degrade as the illuminated area decreases. The general non-uniformly illuminated solar cell will not be treated here. But it is conceivable that the general characteristics are similar to those of Table 1.

The results of the smaller ratio of power output compared to the ratio of active area of Table 7.3 is in agreement with the reported experiments. This has been explained by the formation of the transverse photovoltage across the light-dark boundary. Hence the total injected dark current density is increased and the output power is reduced.

Table 7.3 Calculated results of several non-uniformly illuminated solar cells.

Device Number	Analysis	Active Area	Ratio of Active Area	Ratio of Power Output	I_{sc} mA/cm^2	V_{oc} volts	C_{FF}	EFF %	I_M mA/cm^2	V_M volts	P_M mW
1	1-DIM	2	-	-	40.0	0.536	0.805	12.76	37.78	0.457	17.26
1	2-DIM	1.752	1.0	1.0	34.19	0.531	0.781	10.48	32.01	0.443	14.18
2	2-DIM	1.314	0.75	0.707	24.56	0.522	0.782	7.41	22.99	0.436	10.03
3	2-DIM	0.876	0.50	0.474	16.67	0.511	0.790	4.97	15.57	0.432	6.72
4	2-DIM	0.438	0.25	0.133	4.99	0.480	0.791	1.40	4.53	0.418	1.89

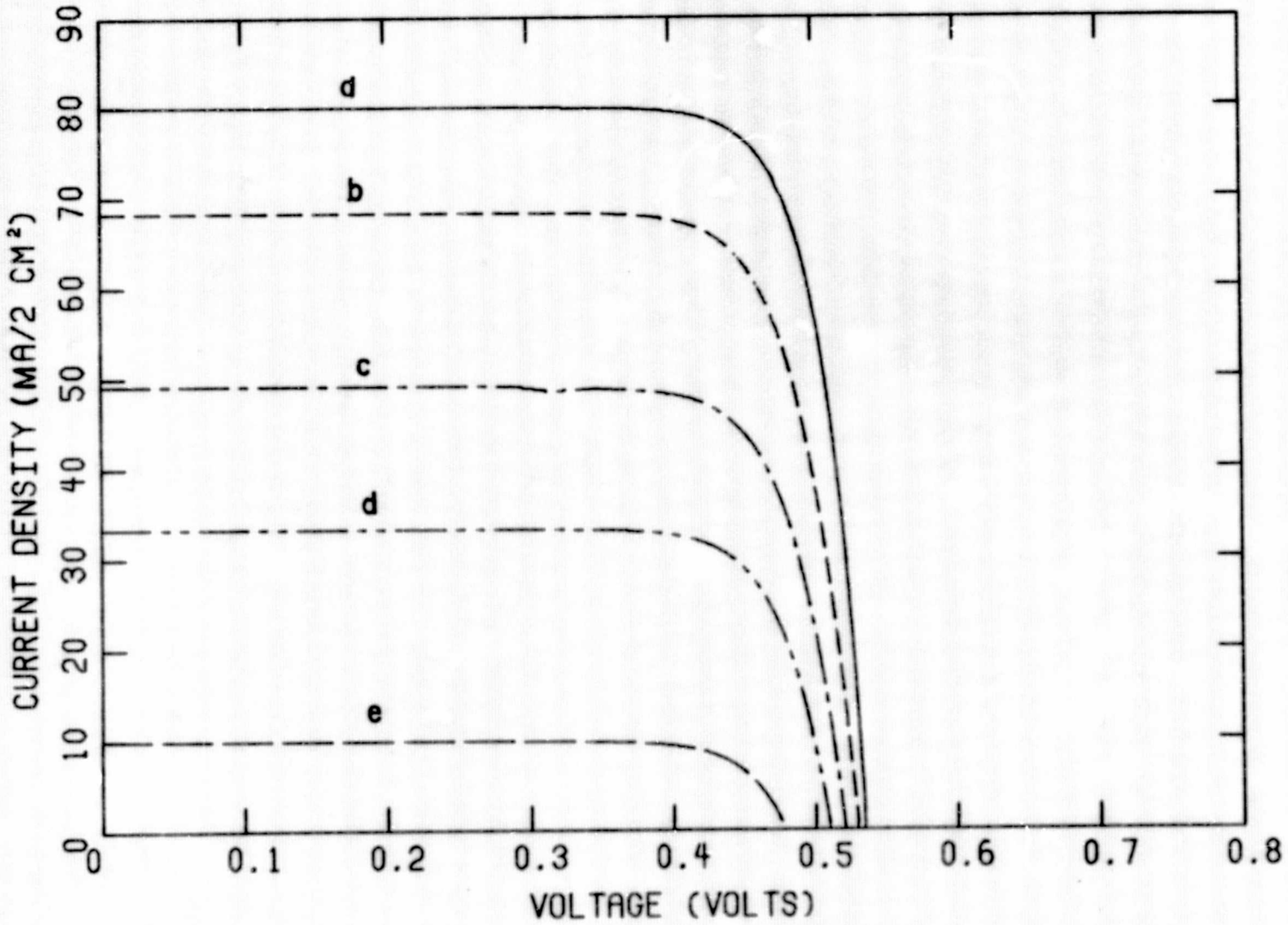

Figure 7.4. Photovoltaic I-V characteristics for several non-uniformly illuminated cells. One-dimensional model (a), two-dimensional model with full (b), three quarters (c), half (d) and one quarter (e) active areas.

8. BACK SURFACE FIELD SOLAR CELL

8.1 Introduction

The presence of a built-in back surface field has recently been found to improve solar cell operation [40]. Such BSF cells have higher collection efficiency and most significantly have a larger output voltage. Several physical models have been proposed to explain and predict the characteristics of BSF cells. Goldweski etc. [60] suggests that the confinement of minority carrier in the base region by the small effective surface recombination velocity at the high-low junction is responsible for the higher V_{oc}. He also pointed out the relative constancy of V_{oc} as a function of device width. Fossum [61] proposed that it is the increase of the integrated base doping density, especially the higher back surface doping density and subsequently the reduction of the minority diffusion current which leads to the unusually high V_{oc} in a BSF silicon solar cell.

It is the purpose in this section to discuss the physical fundamentals of the BSF cells, and to show that a first order model of the BSF cell agrees with the complete numerical model. Discrepancies in the measured and apparent diffusion length of BSF cells is discussed and the constancy of the high V_{oc} values as a function of the device thickness is again verified.

8.2 Characteristics of BSF Cell.

The modeling of Aluminum BSF cell D-5 suggests that the actual diffusion length is much larger than the experimentally measured value. It is fairly

easy to understand that the maximum measured value of diffusion length cannot be greater than the device dimension when using either the X-ray or γ-ray method. The excess carrier density in the base region of a BSF cell differs significantly from a simple exponential diffusion profile. Therefore the above methods need to be used carefully in the presence of high-low junctions.

Shown in Table 8.1 are computer simulation results for BSF cell D-4-3 and a comparison to a conventional cell which has similar parameters and structure except for the high-low junction. The better collection efficiency is clearly seen in the table. Open circuit voltage is significantly higher for the BSF cell.

Table 8.1 Comparison of conventional and BSF cells

	VOC (volts)	ISC (mA/cm^2)	CFF	EFF (%)	VM (volts)	IM (mA/cm^2)	PM (mw)
D-4-2	0.534	45.81	0.812	14.68	0.460	43.17	19.86
D-4-3	0.614	48.90	0.806	17.88	0.524	46.17	24.19

In a conventional non-BSF, 10 Ω·cm silicon cell, the measured diffusion length varies between 100 μm and 250 μm. The measured V_{oc} is typically in the range of 0.50 volts to 0.55 volts and is also a strong function of cell thickness. On the contrary the V_{oc} of BSF cells is relatively constant with respect to cell thickness with an unusually high value as Figure 8.1 shows.

The data of a high V_{oc} suggest that the diffusion length in a BSF cell is much larger than the cell thickness in order to have an effective interaction between minority carriers injected at the p-n junction and the high-low junction. Substantial improvements of V_{oc} due to the back surface

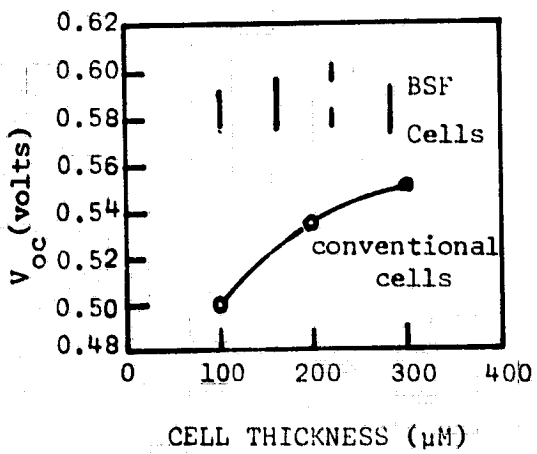

Figure 8.1. V_{oc} of conventional cell and BSF cell as a function of the device thickness.

field have been observed in silicon cells with thickness as thick as 33 mils [62]. In fact diffusion lengths as high as 1000 μm are not impossible to reach for bulk 10 Ω•cm material as Figure 3.1 shows.

8.3 First Order Theory

The forward dark current is exactly opposite to the photon-generated current when a solar cell is at open circuit conditions. Hence V_{oc} can be easily related by first order models to the short circuit current density I_{sc} and the diode saturation current density I_s by the following expression

$$V_{oc} = \frac{kT}{q} \ell n \left(\frac{I_{sc}}{I_s} + 1\right), \tag{8.1}$$

if Shockley's simple diffusion theory is assumed and I_{sc} can be assumed constant with respect to the forward voltage. V_{oc} can be increased by increasing I_{sc} or more effectively by reducing I_s. Since I_s is dominated by the base diffusion component in a high resistivity cell of 10 Ω•cm or larger as Table 4.7 shows, only the base diffusion current will be considered here.

The saturation current density I_s of the high-low junction solar cell has been previously developed [60] and the injected minority carrier density and the minority carrier density at the HL junction assume the following forms:

$$n_p(x) = n(x_{n+p}) \frac{\cosh \frac{W_p - x}{L_p} + S \sinh \frac{W_p - x}{L_p}}{\cosh \frac{x}{L_p} + S \sinh \frac{x}{L_p}}, \tag{8.2}$$

$$n_p(x_{HL}) = n(x_{n+p}) \frac{1}{\cosh \frac{x_{HL}}{L_p} + S\sinh \frac{x_{HL}}{L_p}}, \tag{8.3}$$

where $n(x_{n+p})$ is the injected excess electron carrier density at the p-n junction and subscript p is associated with the p-type base region or with the minority electrons. In this equation S is a normalized interface recombination velocity and is dimensionless, while x_{HL} is the base thickness.

$n(x_{n+p})$ can be expressed at low and high injection limits respectively as

$$n(x_{n+p}) = \frac{n_i^2}{N_p} (e^{qV/kT}-1), \tag{8.4}$$

$$n(x_{n+p}) = n_i \, e^{qV/2kT}. \tag{8.5}$$

The normalized SRV at the HL junction assuming a rear ohmic contact can be expressed as [6]

$$S = \frac{D_{p^+}}{L_{p^+}} \frac{N_p}{N_{p^+}} \frac{L_p}{D_p} \coth \frac{W_{p^+}}{L_{p^+}} \left[1 + \frac{n_p(x_{HL})}{N_p}\right]. \tag{8.6}$$

The base diffusion current density is obtained by differentiating Equation (8.2) as

$$J_d = -qD_p \left.\frac{dn_p(x)}{dx}\right|_{x=x_j}$$

$$= \frac{qD_p}{L_p} \cdot n(x_{n+p}) \frac{S+\tanh \frac{W_p}{L_p}}{1+S \tanh \frac{W_p}{L_p}}. \tag{8.7}$$

Hence it is clear that the current density has a diode slope factor of 1 and 2 at low and high injection respectively from Equations 8.4, 8.5 and 8.7.

From Equation 8.3 and 8.6 the explicit form of S can be derived as

$$S = \frac{(S_o \sinh \frac{x_{HL}}{L_p} - \cosh \frac{x_{HL}}{L_p}) + \sqrt{(\cosh \frac{x_{HL}}{L_p} - S_o \sinh \frac{x_{HL}}{L_p})^2 + 4 \sinh \frac{x_{HL}}{L_p} S_o \cdot n_{(n^+p)}}}{2 \sinh \frac{x_{HL}}{L_p}} \quad (8.8)$$

where $S_o = \frac{D_{n^+}}{L_{p^+}} \frac{N_p}{N_{p^+}} \frac{L_p}{D_p} \coth \frac{W_{p^+}}{L_{p^+}}$ is the normalized SRV at the HL junction at the limit of low injection.

Accompanying the base diffusion current, there also exists a leakage current through the HL junction which assumes the usual form of

$$J_\ell = qn(x_{HL})\, S_{HL}, \quad (8.9)$$

From Equations 8.6 and 8.8 the leakage current can be expressed as

$$J_\ell = qS_o \cdot \frac{D_p}{L_p} \cdot n(x_{HL}) + qS_o \frac{D_p}{L_p} \frac{n^2(x_{HL})}{N_p}. \quad (8.10)$$

It is interesting to investigate the voltage dependence of Equations 8.7 and 8.10. At low injection into the p^+ layer the second term of Equation 8.10 can be neglected and the leakage current has a diode n factor of one at all current levels. The base diffusion current, however, has a diode n-factor of two at high injection limit. The model of the leakage current at the HL junction is consistent with the conventional cell where there is no excess carrier density at the rear contact and hence no leakage current exists.

The case of only base diffusion current is fairly easy to consider as can be seen from Equation 8.7 where S is a constant depending on the device parameters. The results of this calculation are shown as a solid line in Figure 8.2 for various diffusion lengths and base widths. The variation of the predicted V_{oc} values covers a range of 30 mV for device thickness from 100 μm to 300 μm.

However the leakage current is important for thinner devices, especially at the limit of high injection. The effects of high injection in reducing the effectiveness of the HL junction as a minority carrier reflecting boundary and increasing the leakage current has been published elsewhere [63]. In this case the open circuit voltage can be calculated by solving the following equation

$$J_d + J_\ell = J_{sc} \tag{8.11}$$

where J_d and J_ℓ are the diffusion current density and leakage current density of Equations 8.7 and 8.10 respectively. An iterative algorithm has been developed to solve Equation 8.11 for V_{oc} assuming a constant J_{sc} value of 40 mA/cm^2. The results are shown as dashed lines in Figure 8.2 where V_{oc} is much less than the simpler theory for the thinner devices. Also the relative constancy of V_{oc} as a function of device thickness is more consistent with the experimental observations.

Table 8.2 Calculated V_{oc} by the first order theory and including the high injection effect.

x_{HL}(μm) Base width	L_D(μm) Base diff. Length	SRV (low-injection) (cm/sec)	SRV (cm/sec)	$n(x_{HL})$ min. car. density at V_{oc}	V_{oc}
100	100	6.27	6.57	6.07E13	0.519
100	200	-	7.62	2.71E14	0.549
100	300	-	9.34	6.12E14	0.569
100	400	-	11.54	1.05E15	0.583
100	500	-	13.99	1.54E15	0.592
100	600	-	16.35	2.01E15	0.599
100	1000	6.27	23.07	3.35E15	0.612
200	200	6.27	6.88	1.21E14	0.537
200	300	-	7.75	2.95E14	0.5544
200	400	-	8.95	5.34E14	0.568
200	500	-	10.42	8.27E14	0.578
200	600	-	12.09	1.16E15	0.586
200	1000	-	18.61	2.46E15	0.605
300	300	6.27	7.18	1.81E14	0.548
300	400	6.27	7.99	3.43E14	0.560
300	500	6.27	9.01	5.46E14	0.569
300	600	6.27	10.21	7.85E14	0.578
300	1000	6.27	15.75	1.89E15	0.598

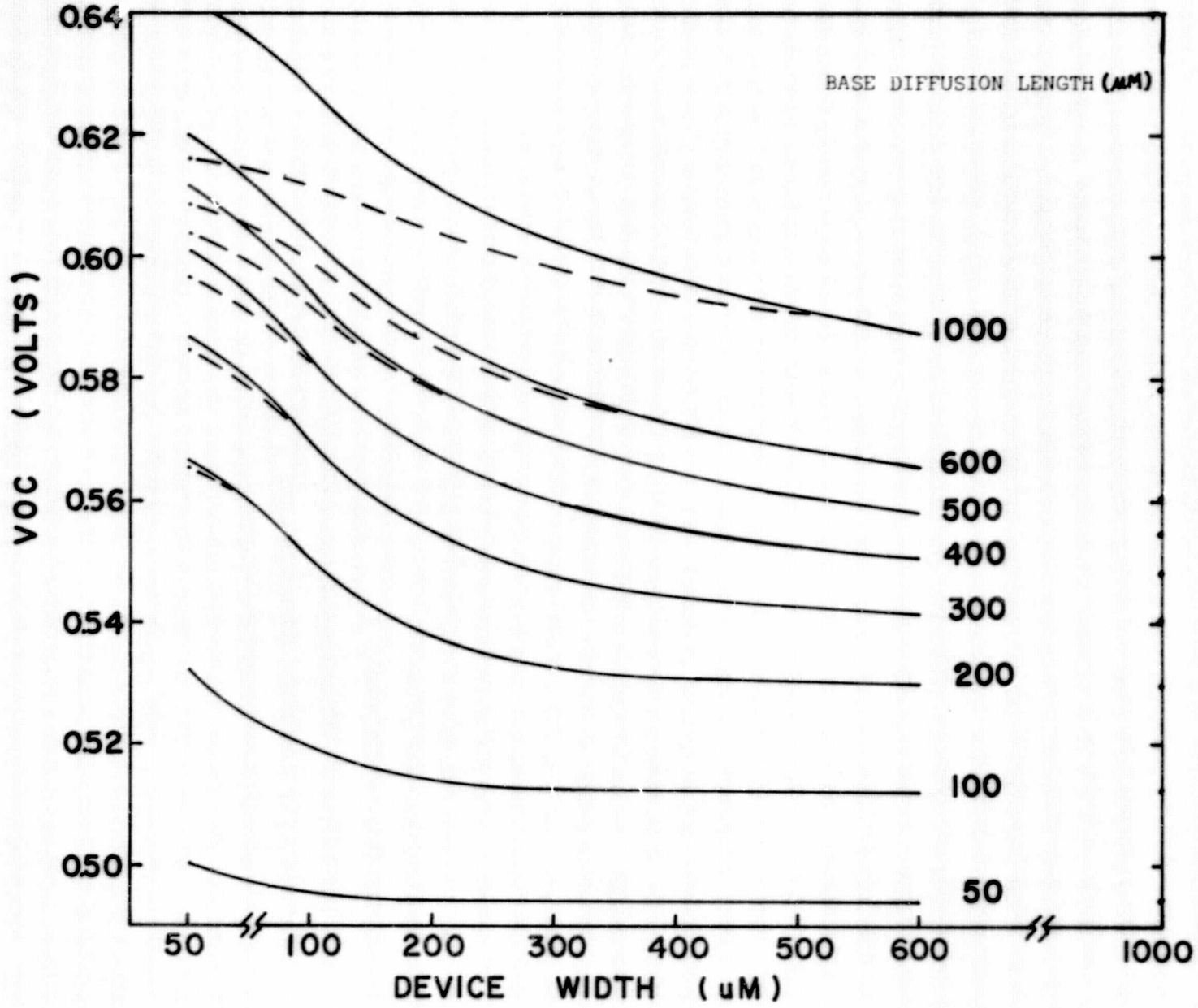

Figure 8.2. Calculation of V_{oc} as function of base diffusion length and device thickness. The parameters are listed below. I_{sc} = 40 mA/cm^2, ρ_B = 10 Ω·cm, D_p = 35, $N_p = 1.25 \times 10^{15}$ #/cm^3, W_{p^+} = 0.5 μM, L_{p^+} = 5 μM, D_{p^+} = 2.5, $N_{p^+} = 10^{19}$ #/cm^3.

8.4 Comparison with the Exact Numerical Calculations

The effects of high injection and leakage current on the prediction of V_{oc} can be demonstrated by the calculation of p^+-i-n cells. Parameters of the p^+-i-n cell are shown in Table 8.3. The initial base diffusion length was assumed to be 500 μm and the subsequent base diffusion length was reduced to values of 267, 136 and 44.5 μm after 1 MeV radiation with a total dose of 10^{14}, $5x10^{14}$ and $5x10^{15}/cm^2$. The lifetime radiation coefficient K_τ was assumed a value of $2.1x10^{-10}$ cm^2/sec. The calculated dark current density compared with the exact numerical calculations are shown in Figure 8.3. The current has a diode factor of two which is characteristic of high injection in a p^+-i-n structure. However the diode factor was found to be close to one instead of two at higher biased voltages for unradiated cells D-7 and D-8. This phenomena can only be explained by the leakage current density at the HL junction. The second term of Equation 8.10 will dominate at this point and the diode n-factor will be one from Equation 8.5. The comparisons of the simple HL junction theory, the modified theory and the exact numerical calculation on the prediction of V_{oc} are presented in Table 8.4. It is clear that the modified first order theory is in better agreement with the exact numerical calculation. It can be concluded that the leakage current at a HL junction cannot be neglected for certain BSF cells with long diffusion length, short device widths and/or high base resistivity.

Table 8.3 p^+-i-n thin solar cell parameters

CELL THICKNESS	101 μm (4 mil) or 51 μm (2 mil)
p^+ thickness	0.5 μm
i	100 μm or 50 μm
n	0.5 μm
p^+ doping	$2x10^{20}$ erfc
n doping	10^{19} constant
diffusion length	
p^+	L_D(med)
i	500 μm (initial)
n	L_D(med)
Surface recomb. velocity	10^4 cm/sec
Antireflection Layer	5% reflection film

Table 8.4 Comparisons between the first order theory and the exact numerical calculation.

p^+-i-n	(μM) Device Width	(μm) Base Diffusion Length	V_{oc}(volts) HL junction theory	V_{oc}(volts) HL junction theory including leakage	V_{oc} Exact Calculation
D-7	100	500	0.679	0.660	0.660
D-8	50	500	0.712	0.663	0.671

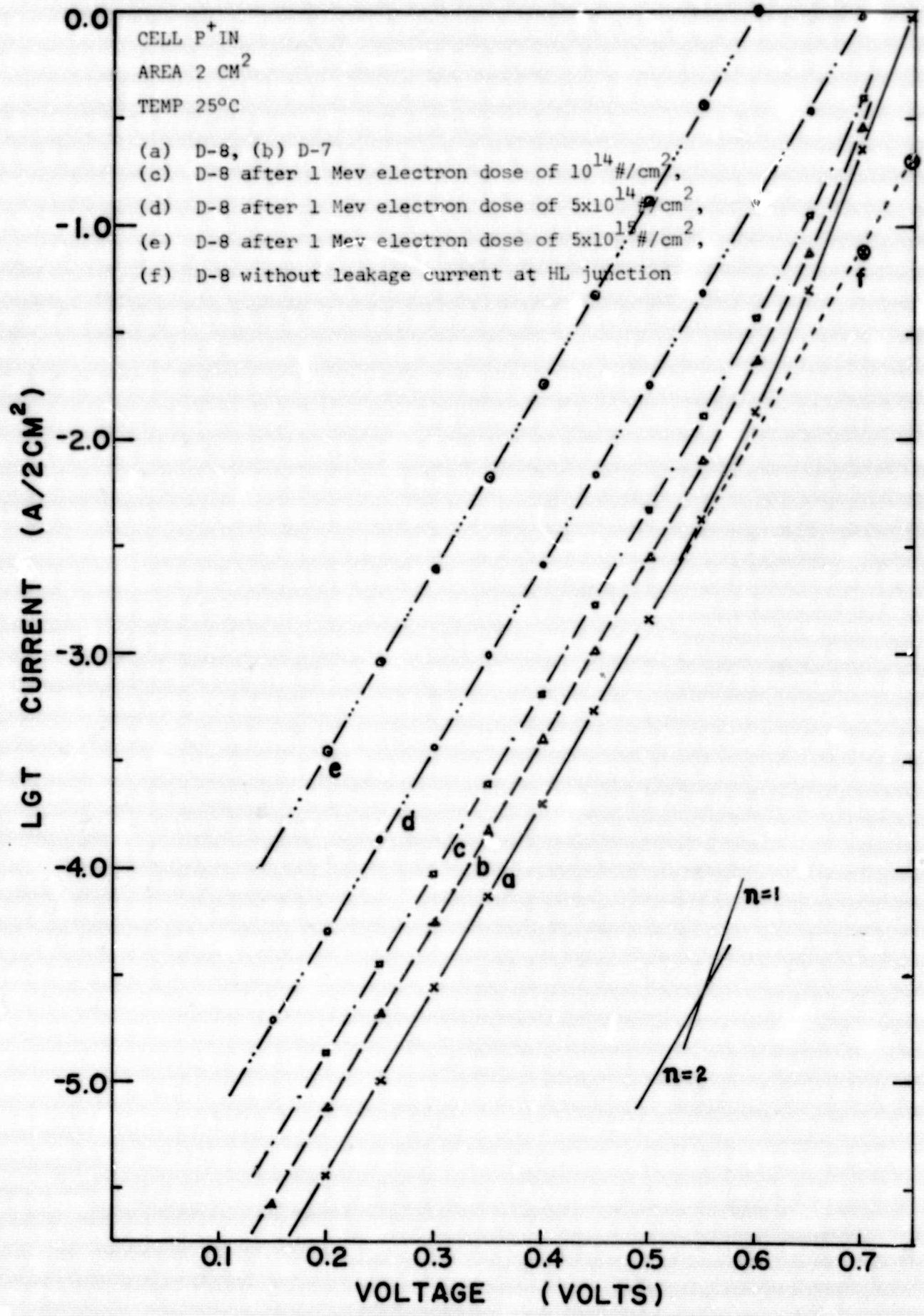

Figure 8.3. Dark I-V characteristics of P^+-I-N cells.

9. APPENDICES

9.1 Impurity Gradients and High Efficiency Solar Cells*

C. R. Fang and J. R. Hauser
North Carolina State University
Raleigh, NC 27607

ABSTRACT

One potential means of improving the efficiency of solar cells especially after space irradiation is to incorporate built-in fields into the device through the use of impurity doping gradients. Previously published papers have indicated an improved minority carrier collection efficiency and improved efficiency when doping gradients are present. In this work a detailed numerical calculation of solar cell performance has been used to study various types of doping gradients. In general the predicted improvements in performance have been less than previously reported due to various device effects such as high injection and the dependence of lifetime on doping density.

*This section has been accepted for publication in Solid-State Electronics.

PAGES 114 THRU. 138 ARE
MISSING FROM THE ORIGINAL DOCUMENT

PRECEDING PAGE BLANK NOT FILM.

9.2 Two-Dimensional Model of a Solar Cell

9.2.1 Introduction

A solar cell is in general at least a two-dimensional device. One dimension is parallel to the p-n junction where the light-generated current flows while the other dimension is perpendicular to the p-n junction. Although the optical current may be uniformly generated over the junction area, the surface current density is non-uniformly distributed over the active area. The sheet resistance and contact resistance which are traversed by the surface current density are thus functions of the relative location of a given area to the finger contact. All these considerations add to the complexity of a solar cell and require the use of a two dimensional model for an accurate analysis of the terminal properties of a solar cell.

The equations of the two dimensional carrier flow and its associated photovoltaic potential have been previously developed in analytical form [5859,64]. Since the equations are non-linear functions of the current density and series resistance, they can only be solved in closed form under very stringent assumptions such as low light levels or specimens with special contact shapes. Hence the use of closed form equations is very limited. In this chapter a general two-dimensional model for solar cell analysis is proposed and developed. A comparison of the calculated results to experimental data is also presented.

9.2.2 Distributed Resistance and Current Density Model of a Solar Cell

The distributed resistance and current density model considered here is actually a two-dimensional array of ideal one-dimensional solar cells

interconnected by series resistance. Shown in Figure 9.1 is an array of NX and NY points between two grid fingers which are used to locate an element of the two-dimensional array. The number of grid points in the X-direction is NX and the corresponding number in the Y-direction is NY. Figure 9.2 shows the equivalent circuit of the two dimensional model. Figure 9.3 shows the distributive resistance and current model at each grid point where the current source is that of an ideal one dimensional model including both optically generated current and forward bias current. For the present work this current is calculated from the tabulated current vs. voltage values obtained from the one-dimensional computer analysis. R_{ST} is the sheet resistance on the surface and R_c is the contact resistance between the metal-semiconductor interface. The collecting metal is also assumed to have a finite resistance R_M which is included between array elements located on the edges of the grid fingers.

The distributive resistance elements can be calculated from the following equations.

a. Sheet resistance - $R_{N-1} = R_{N+1} = R_{ST} \frac{\Delta X}{\Delta Y}$, (9.1)

b. Sheet resistance $R_{N-NX} = R_{N+NX} = R_{ST} \frac{\Delta Y}{\Delta X}$, (9.2)

c. Contact resistance $R_c' = R_c / A_c$, (9.3)

d. Metal resistance $R_M' = R_M \frac{T}{A_c}$, (9.4)

where ΔX and ΔY are the spacings between grid points in the X- and Y-direction respectively, R_{ST} is the sheet resistance in $\Omega/\square$, R_c is the contact resistivity in $\Omega \cdot cm^2$, and R_M is the metal resistivity in $\Omega \cdot cm$. A_c is the incremental area of the metal contact and T is the thickness of the metal contact grid.

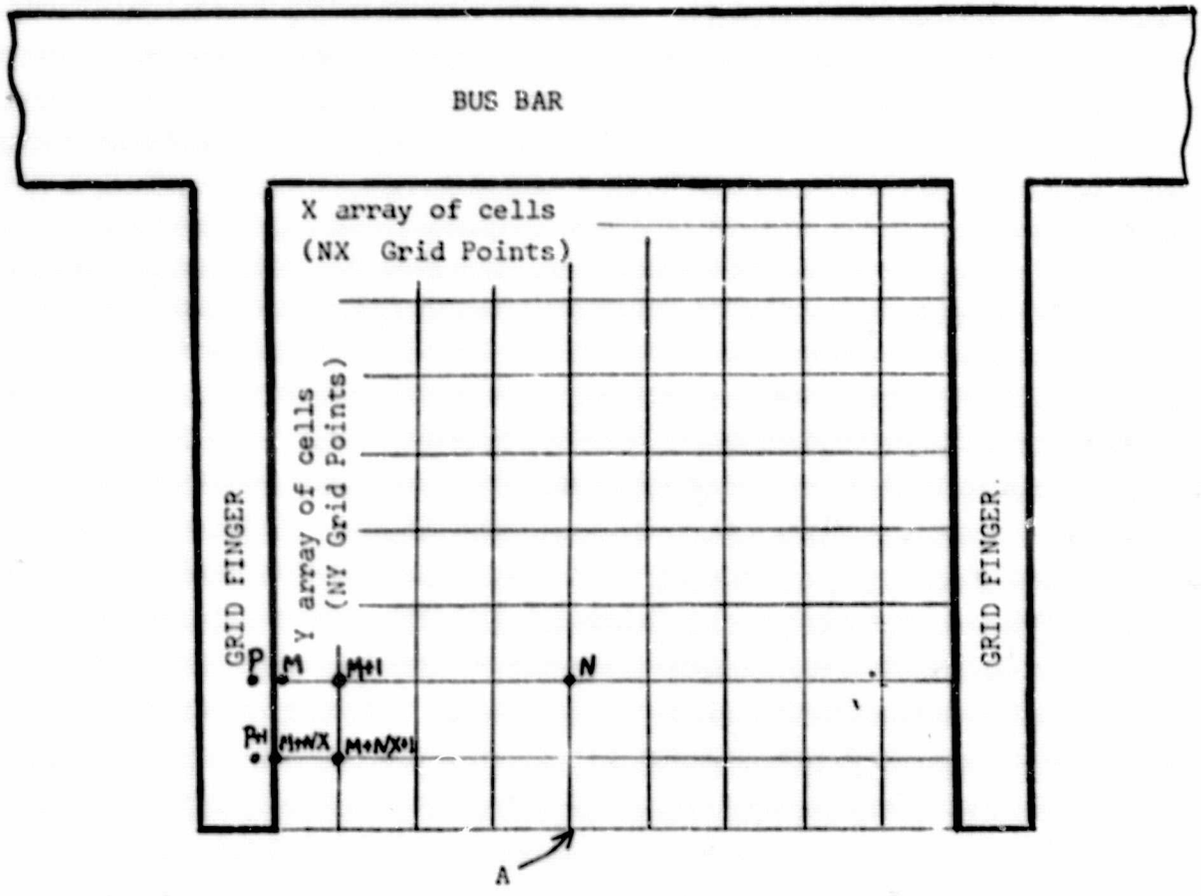

Figure 9.1. Array of Grid Points used for Two-Dimensional Solar Cell Calculation.

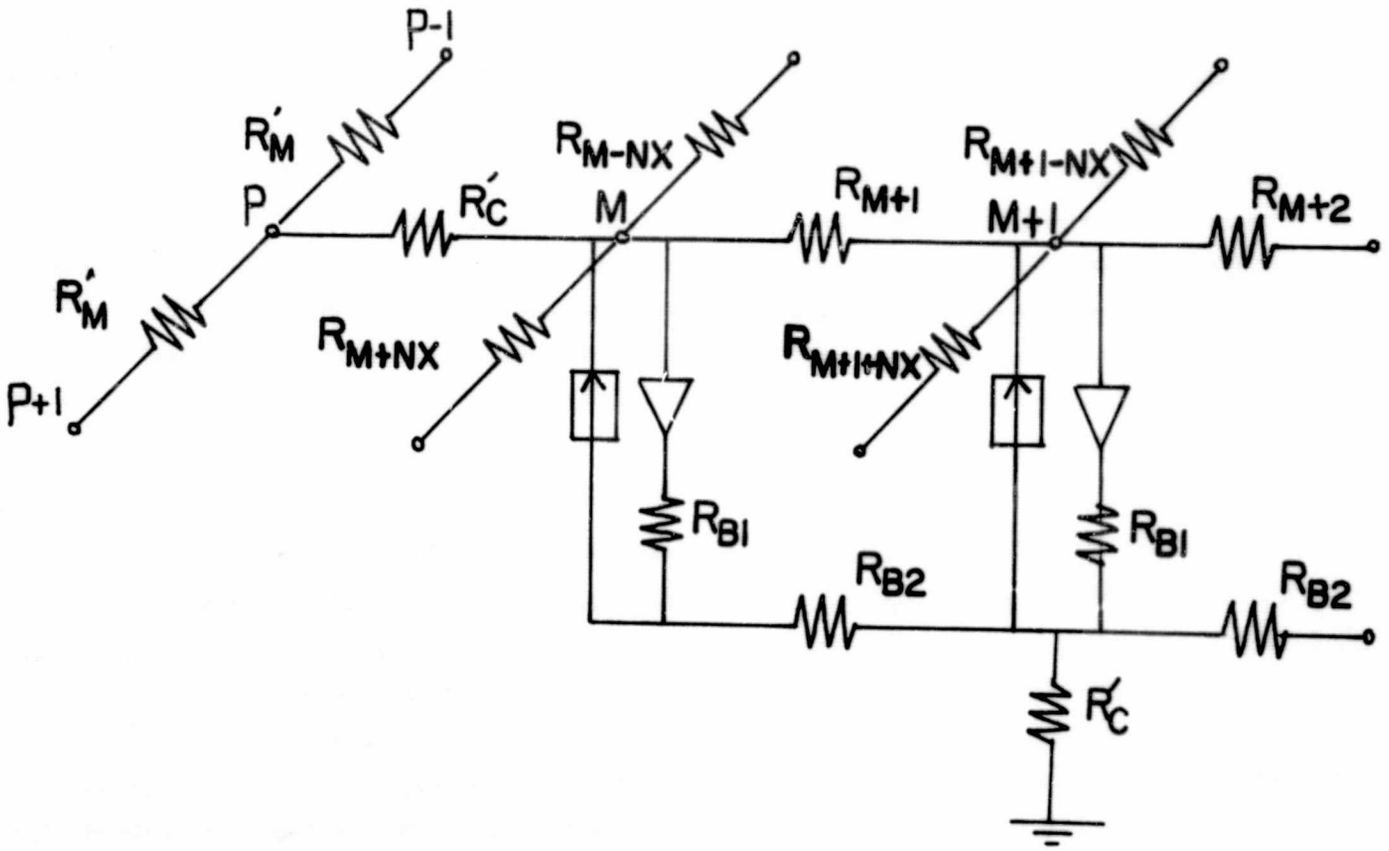

Figure 9.2. Equivalent circuit of a two-dimensional solar cell.

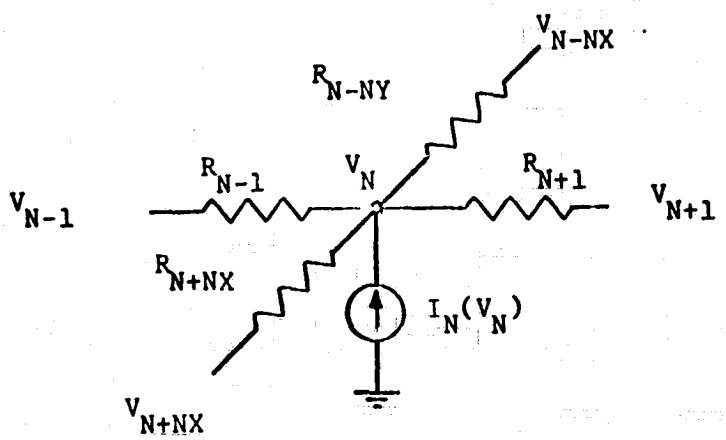

Figure 9.3. Two-dimensional array of one-dimensional cells interconnected by series resistances.

Any bulk resistance R_{B1} in Figure 9.2 which arises from the bulk resistivity of the base layer need not be included here, since it is already included in calculating the one-dimensional I-V characteristics. Also the distributive base resistance R_{B2} in Figure 9.2 can be usually neglected, since most solar cells are covered with an ohmic contact over the entire back surface.

The bus bar is assumed to be at a constant potential which equals the terminal solar cell voltage. The voltage of all other grid points then can be calculated from the simultaneous solution of the node voltage equations at each grid point.

The node voltage equation can be written for each point of the array in the active area (Equation 9.5), for points under the grid contact (Equation 9.6) and for the points on the grid pattern (Equation 9.7) as

$$F[V(N)] = V(N)[G(N-1)+G(N+1)+G(N+NX)+G(N=NX)]-V(n-1)G(N-1)-V(N+1)G(N+1) -V(N-NX)G(N-NX)-V(N+NX)G(N+NX)I_N[V(N)]=0 \quad (9.5)$$

$$F[V(M)] = V(M)[G(M-1)+G(M-NX)/2+G(M+NX)/2+GC(M)]-V(M-1)G(M-1) -V(M-NX)G(M-NX)/2-V(M+NX)G(M+NX)/2-GC(M)V(P)-I_M[V(M)]=0 \quad (9.6)$$

$$F[V(P)] = V(P)[GC(M)+GF\ V(P-1)+GF\ V(P+1)]-V(P-1)\ GF-V(P+1)\ GF-GC(M)\ V(M) \quad (9.7)$$

The task now becomes a problem of solving a system of (NX+2)(NY+1) simultaneous equations in the same number of unknowns.

9.2.3 Numerical Algorithm

The computer algorithm which has been used to solve this system of simultaneous equations is an iterative solution technique based on the modified Newton-Raphson method. A brief discussion of this technique is described.

The Newton-Raphson method can be derived from a Taylor series expansion. For a single function $f(x) = 0$, the algorithm used is $x_{i+1} = x_i - f(x_i)/f'(x_i)$ where x_{i+1} is the approximate value at the (i+1)th iteration. For two coupled equations with two unknowns $f_1(x,y)=0$ and $f_2(x,y)=0$, the algorithm can be written as

$$x_{i+1} = x_i - \frac{1}{J} \begin{vmatrix} f_1(x_i,y_i), & \frac{\partial f_1(x_i,y_i)}{\partial y} \\ f_2(x_i,y_i), & \frac{\partial f_2(x_i,y_i)}{\partial y} \end{vmatrix} \tag{9.8}$$

$$y_{i+1} = y_i - \frac{1}{J} \begin{vmatrix} \frac{\partial f_1(x_i,y_i)}{\partial x}, & f_1(x_i y_i) \\ \frac{\partial f_1(x_i,y_i)}{\partial x}, & f_2(x_i,y_i) \end{vmatrix} \tag{9.9}$$

where J is the Jacobian

$$J = \begin{vmatrix} \frac{\partial f_1(x_i,y_i}{\partial x}, & \frac{\partial f_1(x_i,y_i)}{\partial y} \\ \frac{\partial f_2(x_i,y_i)}{\partial x}, & \frac{\partial f_2(x_i,y_i)}{\partial y} \end{vmatrix} \tag{9.10}$$

For a solution to occur J must not be zero.

The requirement of a non-zero Jacobian is difficult to check before running the program and the computation of the matrix operations is time consuming, hence a simpler modifier Newton-Raphson method is generally used which consists of applying the single-variable Newton-Raphson method n times, once for each variable in a system of n simultaneous equations. Each time we do this, we assume that the other variables are kept constant.

Consider as an example two equations with two unknowns such as

$$f_1(x,y) = 0, \tag{9.11}$$

$$f_2(x,y) = 0. \tag{9.12}$$

Taking x_o and y_o as the initial guesses new values are obtained as

$$x_1 = x_o - \frac{f_1(x_o,y_o)}{\frac{\partial f_1(x_o,y_o)}{\partial x}}, \tag{9.13}$$

$$y_1 = y_o - \frac{f_2(x_o,y_o)}{\frac{\partial f_2(x_o,y_o)}{\partial y}} \tag{9.14}$$

The algorithm is then repeated until the desired degree of accuracy is achieved. An important question is which variables should be used to calculate the next approximate solution and in what order.

One simple example given below will illustrate this point.

$$f_1(x,y) = 0.2X + 0.1\ Y-0.01, \tag{9.15}$$

$$f_2(x,y) = 0.1X + 0.2Y-0.01. \tag{9.16}$$

When we use $f_1(x,y)$ to calculate x and $f_2(x,y)$ for y, convergence to an error of 10^{-4} is achieved in 14 iterations. While the choice of $f_2(x,y)$ to calculate x and $f_1(x,y)$ to calculate y gives a fast divergence. In general, it can be easily shown that the function with the steeper slope at the solution point with respect to variable x should be chosen to calculate the next approximate x, and similarly for y.

The question of convergence for the modified Newton-Raphson method is a touchy one, since one cannot always guarantee a solution. For n simultaneous equations with n unknowns, there are n! ways of picking the variables and order of execution and usually only one of these choices may converge [65].

Sometimes the modified Newton-Raphson method doesn't converge but instead oscillates back and forth around the solution. This raises the question of when to stop the iterations. In this work the iteration has typically been continued until the maximum changes of the variable is below some selected small value, but what this may mean with respect to the answer is another question. In fact it is possible that the difference between two successive calculations may be very small even though the values are nowhere near the right answer in the case of very slow convergence. To overcome this difficulty, the so-called under-and-over relaxation method has been used as a weighting parameter in the variable correction equation.

In this work, the unknown variables are always chosen from the equation which shows the steepest slope with respect to that particular variable at the solution point. And the order of evaluations are arranged to assure fast convergence with an appropriate relaxation weight.

Suppose $V(N)_j$ is the j'th iteration value of V(N). The next corrected value by using the one-variable Newton-Raphson method is then

$$V(N)_{j+1} = V(N)_j - \frac{F[V(N)_j]}{F'[V(N)_j]}, \tag{9.17}$$

Where $F'[V(N)_j]$ is the partial derivative with respect to $V(N)_j$. The explicit form of $F'[V(N)_j]$ is

$$F'[V(N)_j]=G(N+L)+G(N-1)+G(N-NX)+G(N+NX) - \frac{\partial I_N[V(N)_j]}{\partial V(N)_j} \tag{9.18}$$

for the grid points on the active area. $I_N[V(N)]$ is the current density of the dark current density superimposed on the optically-generated current density. The current derivative can be accurately calculated, if the injected dark current density is assumed to be an exponential function of the potential at each particular grid point.

A flow chart of the two dimensional analysis program is shown in Figure 9.4. The input data consists of the one-dimensional I-V data plus structural data on the contact finger arrangement. The complete two dimensional I-V characteristics of the solar cell is then calculated at specified terminal voltage points using the modified Newton Raphson method. Calculations have typically been made until the voltage is accurate at each array point to less than 10^{-4} volts. With the voltage known at each array point the total solar cell current can then be evaluated by summing the current contributions from each node in the array.

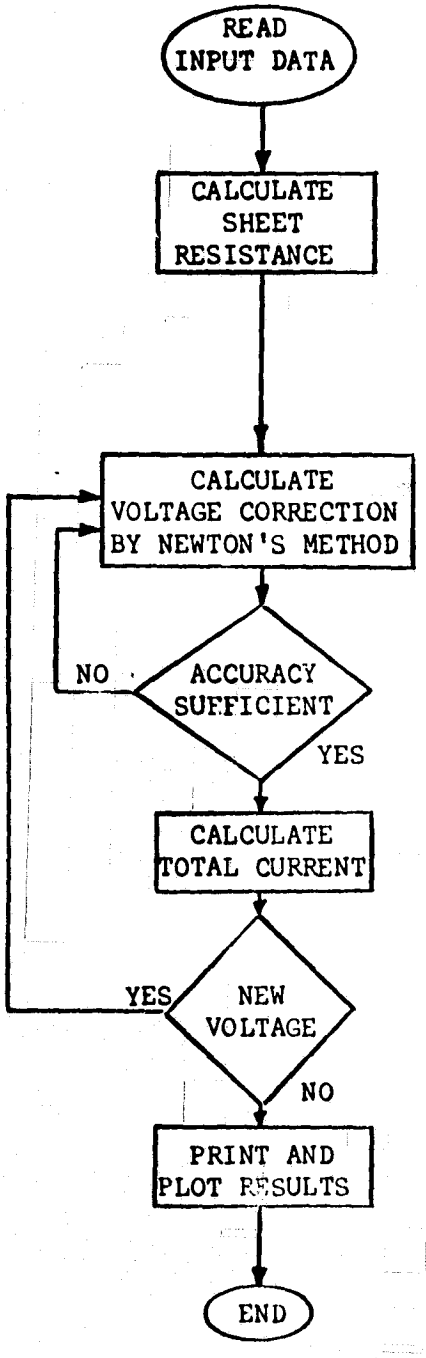

Figure 9.4. Flow Chart of Two-Dimensional Analysis Program

9.2.4 Discussions

Several questions may arise concerning the accuracy of this model. The first question concerns the number of grid points used in the calculation. Theoretically we can use as many points as we want to improve the precision in calculation. In this work, an array of 20x20 grid points has generally been used unless mentioned otherwise. This results in errors of only a few percent even in very severe conditions such as high sheet and contact resistance.

The second question concerns the validity of the one dimensional I-V characteristics used in the two dimensional analysis. Since the typical built-in field in the diffused surface is in the range of 10^3-10^4 volts/cm which is several orders of magnitude larger than the transverse field, the development of a transverse field in the two-dimensional analysis has a negligible influence upon the minority current density obtained from the one-dimensional model.

The third question is the assumption that the optically generated carriers in the base region will only be collected at the junction under the illuminated area. It is possible for the generated carrier in the base region to diffuse to the junction under the grid pattern, especially for the case of a thin collecting metal grid and a long diffusion length of the base minority carrier. For "good" cells with low sheet and contact resistance this effect is found to be relatively unimportant, since the total collected optical current is the same in both cases.

The fourth assumption concerns modeling of contact resistance through a distributed surface contact resistor. In good solar cells, the surface contact resistance is usually very small because of the high surface doping density. The base contact resistance is limited by the substrate doping density for non BSF cells and may not be negligible. The base contact resistance can however be transformed into an effective surface

contact resistance. The calculated photovoltaic potential is the potential difference across the p-n junction irrespective of the combination of contact resistance from the surface or base. The relative voltage drop across the surface or base contact resistance can be determined experimentally.

9.2.5 Comparisons Between Model and Experimental Measurements

Sample D-9 is a 10 mil thick n^+-p silicon cell with a 10 Ω•cm substrate. The p-n junction is diffused at 750°C for 30 minutes resulting in a thin surface layer with measured junction depth of 0.15 μm and high sheet resistance. The contact resistance is also large.

Comparisons of the experimental data and theoretical calculations are good. Figure 9.5 shows the 2-dimensional calculation without illumination for sample D-9. Figure 9.6 shows the photovoltaic current-voltage characteristic for the 1-dimensional model for both total area and active area. The 2-dimensional calculations are also shown taking into account the effects of sheet resistance and contact resistance. More examples of two-dimensional calculation are presented in Section 4 and 5. In each case the agreement between the experimental data and the two-dimensional calculations are seen to be very good.

9.2.6 Conclusions

(A) A general two-dimensional program has been developed which can simulate a practical solar cell with any arbitrary grid pattern and series resistance.

(B) A general two-dimensional program is a good tool for the optimum design of grid patterns and the prediction of the non-linear series resistance effects at the maximum power output.

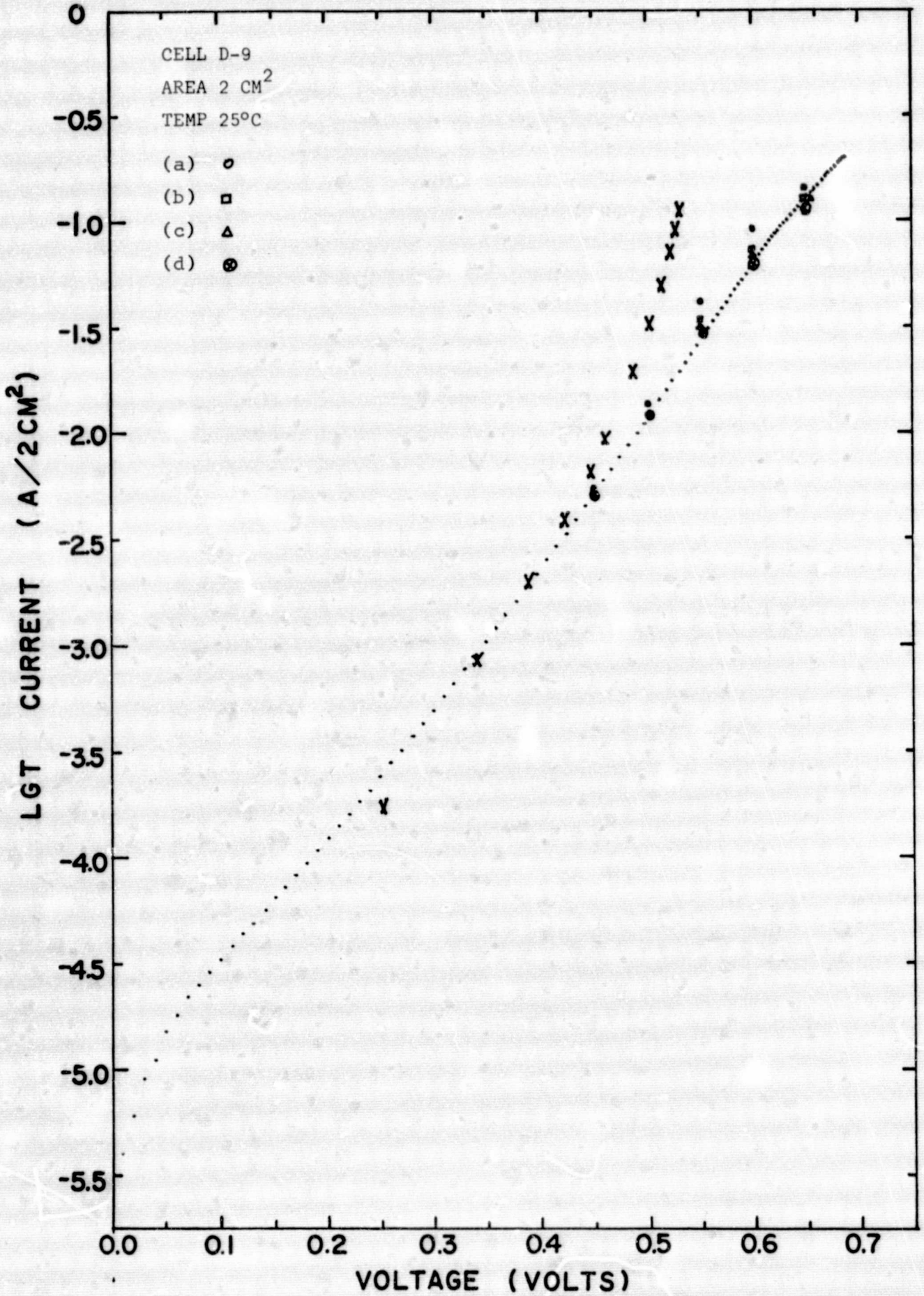

Figure 9.5. Comparison of the dark I-V characteristics of D-9 and the two-dimensional model with R_{ST} and R_C to be 2150 Ω/□ and 0.72Ω respectively.

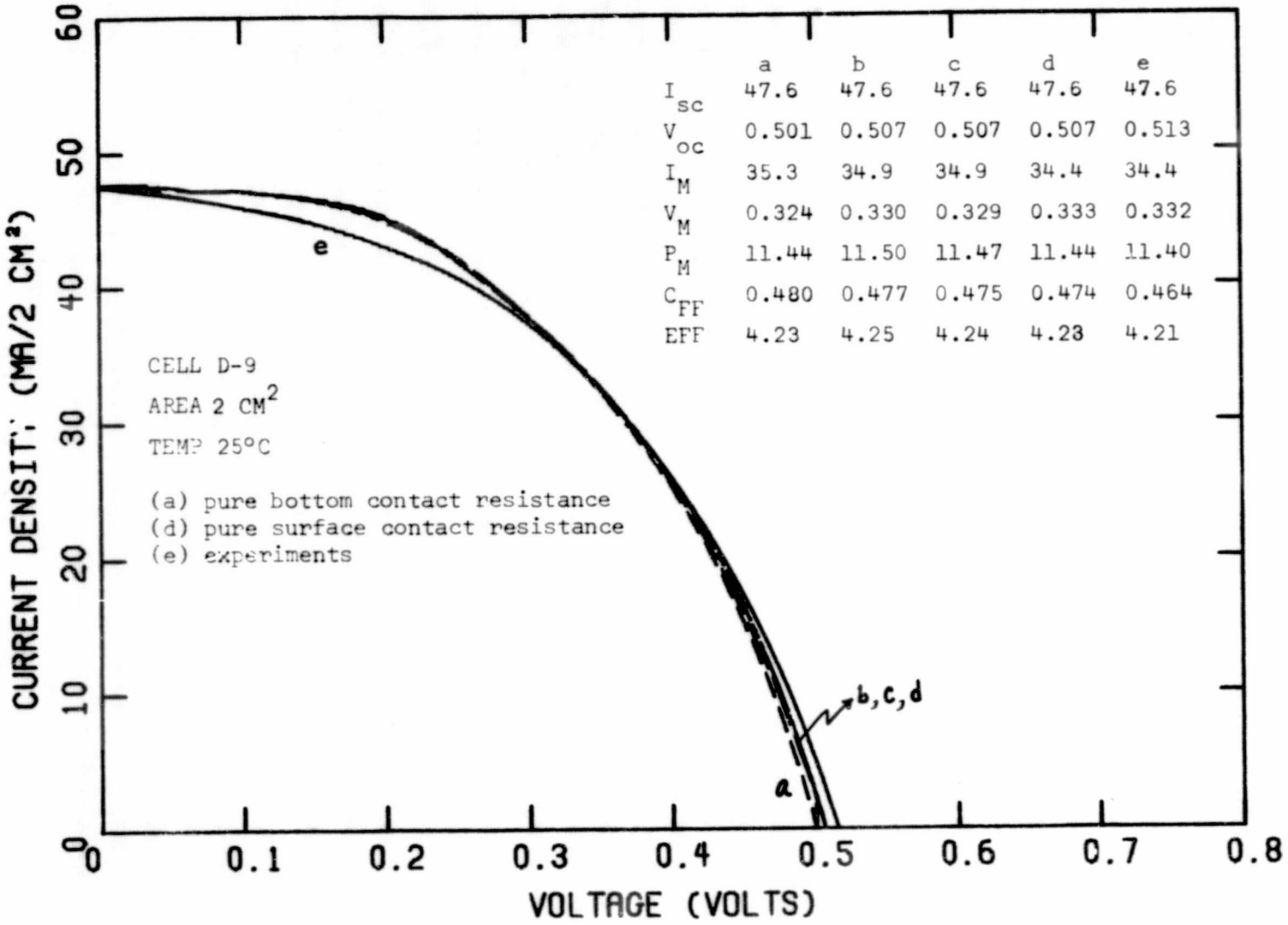

Figure 9.6. Comparison of the photovoltaic I-V characteristics of D-9 and the two-dimensional model.

9.3 Surface Lifetime Model

For a heavy doped region several lifetime models have been proposed. Data by Nilsson and Svantesson [66] suggest the dominance of the Auger recombination mechanism in regions of high doping density. The Auger recombination rate has been developed as [67].

$$U_A = G_e\,(n^2p - nn_i^2) + G_h(p^2n - pn_i^2), \tag{9.19}$$

where the Auger recombination coefficients G_e and G_h are found to be 1.7×10^{-31} cm^6/sec and 1.2×10^{-31} cm^6/sec for n-type and p-type silicon respectively [68].

Hence the Auger lifetime is proportional to the reciprocal of the square of the majority carrier density with

$$\tau_e = \frac{1}{G_h p^2} \quad \text{in p-type materials and} \tag{9.20}$$

$$\tau_h = \frac{1}{G_e n^2} \quad \text{in n-type materials} \tag{9.21}$$

The three device equations governing the carrier transport mechanism in semiconductors have been reproduced below including Auger recombination [69].

$$\frac{d^2\psi}{dx^2} = F_1(\psi, \phi_n, \phi_p) \tag{9.22}$$

$$\frac{d^2\phi_n}{dx^2} = F_2(\psi, \phi_n, \phi_p, \psi', \phi_n') + F_2'(\psi, \phi_n, \phi_p, \psi', \phi_n') \tag{9.23}$$

$$\frac{d^2 d_p}{dx^2} = F_3(\psi, \phi_n, \phi_p, \psi', \phi_p') + F_3'(\phi, \phi_n, \phi_p, \phi', \phi_p') \tag{9.24}$$

As a supplement to Table 5.2 and 5.3 in Reference [69], the terms of Auger recombination are shown in Table 9.1 and 9.2.

Table 9.1 Partial derivatives of F_2'

$$F_2'(\psi, \phi_n, \phi_p, \psi', \phi_n') = -\gamma_n G_e [\exp(\phi_p-\phi_n)-1] - \gamma_n G_h [\exp(2\phi_p-2\psi)-\exp(\phi_n+\phi_p-2\psi)]$$

$$\frac{\partial F_2'}{\partial \psi} = 2\gamma_n G_h \exp(2\phi_p-2\psi) - 2\gamma_n G_h \exp(\phi_n+\phi_p-2\psi)$$

$$\frac{\partial F_2'}{\partial \phi_n} = \gamma_n G_e \exp(\phi_p-\phi_n) + \gamma_n G_h \exp(\phi_n+\phi_p-2\psi)$$

$$\frac{\partial F_2'}{\partial \phi_p} = -\gamma_n G_e \exp(\phi_p-\phi_n) - 2\gamma_n G_h \exp(2\phi_p-2\psi) + \gamma_n G_h \cdot \exp(\phi_n+\phi_p-2\psi)$$

$$\frac{\partial F_2'}{\partial \psi'} = 0$$

$$\frac{\partial F_2'}{\partial \phi_n'} = 0$$

Table 9.2 Partial derivatives of F_3'

$$F_3'(\psi, \phi_n, \phi_p, \psi', \phi_p') = \gamma_p G_e [\exp(2\psi-2\phi_n)-\exp(2\psi-\phi_n-\phi_p)] + \gamma_p G_h [\exp(\phi_p-\phi_n)-1]$$

$$\frac{\partial F_3'}{\partial \psi} = 2\gamma_p G_e \exp(2\psi-2\phi_n) - 2\gamma_p G_e \exp(2\psi-\phi_n-\phi_p)$$

$$\frac{\partial F_3'}{\partial \phi_n} = -2\gamma_p G_e \exp(2\psi-2\phi_n) + \gamma_p G_e \exp(2\psi-\phi_n-\phi_p) - \gamma_p G_h \exp(\phi_p-\phi_n)$$

$$\frac{\partial F_3'}{\partial \psi'} = 0$$

$$\frac{\partial F_3'}{\partial \phi_p'} = 0$$

The calculation of spectral response for device D-2 of Section 4 including the Auger recombination is presented in Table 9.3 for wavelength 0.4 μm to 0.6 μm.

Table 9.3 Comparison of the surface lifetime model with or without Auger recombination mechanism.

Wavelength μm	No Auger	Include Auger	(mA/mW) Experiments
0.4	0.0141	0.0017	0.0056
0.4125	0.0208	0.0061	-
0.425	0.0315	0.0151	-
0.45	0.0624	0.0614	0.0544
0.5	0.1319	0.1169	0.1294
0.6	0.2393	0.2301	0.2310

It is fairly difficult to reach a conclusion from this data as to whether or not Auger recombination plays an important role in the heavily doped surface region. Since there are some uncertainties about the diffused surface lifetime, the magnitude of SRV and heavy doping effect as well as the Auger recombination coefficient. However it is believed Auger recombination may play some role in this highly doped region with somehow smaller values of Auger recombination coefficient.

Another model of surface lifetime has been proposed by Lindholm, et al. [70]. The general form of this doping dependent model is

$$\tau(x) = \frac{\tau_o}{(N_S/N_B+1)^N} \tag{9.25}$$

with N value of 1, 2 or 4. For large N values the resultant surface lifetime of the high doping density is in the range of 10^{-12} second or less which is close to the relaxation time and is nonrealistic.